

AFRL-IF-RS-TR-2004-148
Final Technical Report
June 2004



WATER POWERED BIOASSAY SYSTEM

University of California at Berkeley

Sponsored by
Defense Advanced Research Projects Agency
DARPA Order No. E117

APPROVED FOR PUBLIC RELEASE; DISTRIBUTION UNLIMITED.

The views and conclusions contained in this document are those of the authors and should not be interpreted as necessarily representing the official policies, either expressed or implied, of the Defense Advanced Research Projects Agency or the U.S. Government.

AIR FORCE RESEARCH LABORATORY
INFORMATION DIRECTORATE
ROME RESEARCH SITE
ROME, NEW YORK

REPORT DOCUMENTATION PAGE

Form Approved
OMB No. 074-0188

Public reporting burden for this collection of information is estimated to average 1 hour per response, including the time for reviewing instructions, searching existing data sources, gathering and maintaining the data needed, and completing and reviewing this collection of information. Send comments regarding this burden estimate or any other aspect of this collection of information, including suggestions for reducing this burden to Washington Headquarters Services, Directorate for Information Operations and Reports, 1215 Jefferson Davis Highway, Suite 1204, Arlington, VA 22202-4302, and to the Office of Management and Budget, Paperwork Reduction Project (0704-0188), Washington, DC 20503

1. AGENCY USE ONLY (Leave blank)		2. REPORT DATE JUNE 2004	3. REPORT TYPE AND DATES COVERED Final Sep 00 – Dec 03	
4. TITLE AND SUBTITLE WATER POWERED BIOASSAY SYSTEM			5. FUNDING NUMBERS C - F30602-00-2-0566 PE - 63739E PR -E117 TA - 00 WU - 53	
6. AUTHOR(S) Liwei Lin				
7. PERFORMING ORGANIZATION NAME(S) AND ADDRESS(ES) University of California at Berkeley Department of Mechanical Engineering 5126 Etcheverry Hall Berkeley California 94720-1740			8. PERFORMING ORGANIZATION REPORT NUMBER N/A	
9. SPONSORING / MONITORING AGENCY NAME(S) AND ADDRESS(ES) Defense Advanced Research Projects Agency AFRL/IFTC 3701 North Fairfax Drive Arlington Virginia 22203-1714			10. SPONSORING / MONITORING AGENCY REPORT NUMBER AFRL-IF-RS-TR-2004-148	
11. SUPPLEMENTARY NOTES AFRL Project Engineer: George O. Ramseyer/IFTC/(315) 330-3492/ George.Ramseyer@rl.af.mil				
12a. DISTRIBUTION / AVAILABILITY STATEMENT APPROVED FOR PUBLIC RELEASE; DISTRIBUTION UNLIMITED.			12b. DISTRIBUTION CODE	
13. ABSTRACT (Maximum 200 Words) This project addresses critical technologies, including the acquisition, metering, buffering, delivery and assay for the processing of bio-fluids that enable the complete integration of microfluidic chips into systems. An all-plastic micromachined water-powered pump was first developed that provided a constant rate fluidic delivery of 0.2 1/hr without requiring electrical power. A low-leakage, hole-in-the-wall micro valve was demonstrated that provided fluidic resistance 255 times higher in the closed state than in the open state. A micro-accumulator was designed, fabricated, and demonstrated that repeatedly stored and delivered fluidic pressure and, with a combination of pumps and valves, formed the basic micro fluidic processing unit. The addition of integrated micro dialysis needles and a bioassay system completed the system by providing the capability of extracting interstitial liquid directly from tissue and making a real-time diagnosis. A water-activated micro power battery was constructed and operated that delivered 0.6 V of power, and was demonstrated by driving a 10 kohm resistor for more than one hour. These micro-fluidic components and system integration technologies are leading the way in developing a microsystem to process microfluidics on a single chip.				
14. SUBJECT TERMS Microfluidics, Microfluidics System, Microvalve, Micro-Accumulator, Micro Dialysis Needle, Bioassay System, Water Activated, Micro Osmotic Pump			15. NUMBER OF PAGES 108	
			16. PRICE CODE	
17. SECURITY CLASSIFICATION OF REPORT UNCLASSIFIED	18. SECURITY CLASSIFICATION OF THIS PAGE UNCLASSIFIED	19. SECURITY CLASSIFICATION OF ABSTRACT UNCLASSIFIED	20. LIMITATION OF ABSTRACT UL	

TABLE OF CONTENTS

1.	EXECUTIVE SUMMARY	1
2.	INTRODUCTION	2
3.	METHODS, ASSUMPTIONS AND PROCEDURES	4
3.1	Water-Powered, Micro Osmotic Pump	5
3.2	Ultra Low-Leakage, Ultra Low-Power Hydrophobic Gate Valve.....	6
3.3	Fore-and-Aft Throttled Osmotic Pump (FATOP).....	6
3.4	Micro Dialysis Needle.....	7
3.5	A Complete Water-powered Bioassay System	8
3.6	Water-Based Micro Power Generation	9
4.	RESULTS AND DISCUSSION.....	11
4.1	Water-Powered, Micro Osmotic Pump	11
4.1.1	Water-Powered, Osmotic Microactuator	11
4.1.2	Water-Powered, Osmotic Micropump.....	17
4.1.3	Water-Powered, Osmotic Drug Delivery System.....	20
4.1.4	A Frozen Water Micromachining Process.....	23
4.1.5	Micro Osmotic Pumping Nano Droplet Generator.....	27
4.2	Ultra Low-Leakage, Low-Power Gate Valve	35
4.2.1	Design of “Hole-in-the-Wall” Ultra Low-Leakage Valve.....	35
4.2.2	Characterizations of Low-Leakage Valve	37
4.2.3	Ultra-Low-Leakage and Ultra-Low-Power Valve in a Microsystem	42
4.3	Fore-and-Aft Throttled Osmotic Pump (FATOP).....	45
4.3.1	A Micro Fluidic Accumulator	46
4.3.2	Fabrication and Characterization of MFA.....	50
4.4	Micro Dialysis Needle.....	54
4.4.1	Micro Fabricated Dialysis Needle	54
4.4.2	Theoretical and Numerical Simulation on Micro Dialysis Needles	57
4.4.3	Integrated Microneedle and Bioassay System.....	60
4.5	Complete Water-Powered Bioassay System.....	63
4.5.1	Localized Plastic Bonding for Assembly, Packaging and Liquid Encapsulation	63
4.5.2	A Micro-gap PH Sensor	69
4.5.3	A Polypyrrole-Carbon-Nanotube Nanocomposite Glucose Sensor.....	71
4.5.4	Control Circuitry	76
4.6	Water-based Micro Power Generation.....	78
4.6.1	Electrolyte-based, On-Demand Microbattery.....	78

4.6.2	Water-activated, Long Shelf-Life Microbattery	81
4.6.3	A Micro Microbial Fuel Cell	87
5.	CONCLUSIONS	92
6.	RECOMMENDATIONS	93
7.	REFERENCES	95
	APPENDIX I. LIST OF JOURNAL PUBLICATIONS	97
	APPENDIX II. LIST OF CONFERENCE PRESENTATIONS	98

LIST OF FIGURES

Figure 1: A complete water-powered bioassay system in a wristwatch	2
Figure 2: Micromachined osmotic pump	5
Figure 3: Schematic diagram of hydrophobic gate valve for ultra-low leakage fluidic control	6
Figure 4: Fore-and-Aft Throttled Osmotic Pump (FATOP)	7
Figure 5: Hollow, Dual-Channel Micro Dialysis Needle	7
Figure 6: Schematic diagram showing the integration of the water-powered micro osmotic pump into the same substrate as the bioassay system	8
Figure 7: A microaccelerometer (top) and the schematic diagram of the packaging cap and the integrated micro power source	9
Figure 8: The working principle of the microbial fuel cell by using an ion-exchange film to convert power from microorganisms	10
Figure 9: Schematic of osmotic actuation	12
Figure 10: One-mask fabrication process of osmotic microactuators	13
Figure 11: SEM micrographs of silicon mold (a), molded cellulose acetate substrate (b)	14
Figure 12: Cross sections of a (a) semipermeable-piston type and an (b) impermeable-piston type osmotic microactuators	15
Figure 13: (a) The micro osmotic actuator has been actuated based on the principle of osmotic pumping, (b) The actuated device is cleaved in half	15
Figure 14: Measured profiles of an actuating membrane during the expansion process	16
Figure 15: Measured peak displacement and volume expansion vs. actuating time characteristic of actuating membranes	17
Figure 16: Schematic diagram of a micro osmotic pump system using osmotic actuator as the pumping source	17
Figure 17: The fabrication process of the micro osmotic pump	18
Figure 18: A fabricated drug delivery system as compared with a one-cent coin	19
Figure 19: The cross sectional SEM micrograph of the drug delivery system	19
Figure 20: The measured delivery profile from the prototype micro drug delivery system	20
Figure 21: Drug delivery (colored liquid) was observed after 10 hours by inserting the system into fresh pork meat	21
Figure 22: Cross-sectional SEM micrograph of the bonding interface between PDMS substrate and Mylar barrier film	21
Figure 23: Measurement set up	23
Figure 24: The schematic diagram of the disposable capillary micropump using frozen water technology	24
Figure 25: Fabrication sequence of the disposable micropump using frozen water as the sacrificial layer	24
Figure 26: The SEM micrograph showing the cross-sectional view of the micro-chambers	25
Figure 27: Higher resolution SEM micrograph of Figure 26 showing the microchannels	25
Figure 28: SEM micrograph of the micropump	26
Figure 29: Measured flow rate of the one-mask, disposable capillary micropump	26
Figure 30: Slow dripping/separation of a droplet from a capillary	27
Figure 31: Microfluidic channel combining attractive and expulsive forces for flow discretization (a) Geometry and surface properties (b) to (f) Splitting sequence	28
Figure 32: Schematic diagram of the flow discretizer	28
Figure 33: Pressure barriers built across the junction prevent water from (a) entering and (b) staying in the hydrophobic area	29
Figure 34: Schematic diagram of the basic element used in the simulation program for surface energy minimization	30
Figure 35: A successful breakaway sequence simulated by Surface Evolver	31
Figure 36: Simulation results of Surface Evolver	31
Figure 37: Fabrication process (a) Selectively casting of liquid pre-polymer (b) Oxygen plasma surface treatment and (c) Final result	32
Figure 38: SEM micrographs of microchannel partially filled and covered by self-aligned mask and a close view near the junction	32
Figure 39: A complete flow discretization sequence	33
Figure 40: Measured segment volume with respect to geometry of the flow discretizer	33

Figure 41: A schematic diagram of the integrated drug delivery system	34
Figure 42: To close the valve, the sliding gate is positioned across the inlet channel using a probe tip	35
Figure 43: Superior sealing is developed by the “hole-in-the-wall” valve seat due to the removal of the leakage path above and below the gate	36
Figure 44: The “hole-in-the-wall” process combines features of both the SCREAM and Dual-depth DRIE processes	37
Figure 45: The open and closed configurations of the valve can be modeled by equivalent fluidic resistor circuits	38
Figure 46: Our test apparatus was designed to reduce dead volume and fluidic capacitance	40
Figure 47: Valve open	40
Figure 48: Valve closed	40
Figure 49: When the valve is closed, the fluidic resistance increases 255 times the fluidic resistance of the valve in the open position	42
Figure 50: Photograph (top view through the Pyrex [®] cover onto the silicon substrate) of the planar micropump	42
Figure 51: SEM micrograph of the in-plane flap valve	43
Figure 52: Photograph (top view thorough the Pyrex [®] cover) of the flap (bent in the open position) during fluid flow through the "hole-in-the-wall"	44
Figure 53: Schematic diagram of the dicing sequence	45
Figure 54: A conceptual drawing of the micro fluidic accumulator (MFA)	47
Figure 55: Micro fluidic accumulator schematic	47
Figure 56: Planar wafer-level Fabrication Process for the MFA	49
Figure 57: Fabrication results for the planar wafer-level process	50
Figure 58: Testing system schematic	51
Figure 59: Pressure as a function of z_c for the MFA	51
Figure 60: Mode of operation of the micro accumulator	52
Figure 61: Fluid remains in the microfluidic accumulator after 5-10 filling cycles	52
Figure 62: The system integration	53
Figure 63: SEM micrograph of a micro dialysis microneedle	55
Figure 64: SEM micrograph of the fluid channel of a microneedle	55
Figure 65: Fabrication process of the improved micro dialysis needle	56
Figure 66: Calculated 2-dimensional diffusion	59
Figure 67: Fluorescent dye in equilibrium with a water droplet on the needle	59
Figure 68: Photograph of the μ -needle-based glucose monitor	60
Figure 69: SEM micrograph of 200 μm long hollow μ -needles with an inner diameter of 40 μm	60
Figure 70: Sensor response of the single use glucose monitor after sampling interstitial fluid	61
Figure 71: Photograph of a bonded wafer pair showing the inlet and outlet for wafer-level enzyme loading (top) and single chip with an integrated glucose sensor inside the flow channel (bottom)	61
Figure 72: Photograph of 15 μm thick gel sleeves immobilized around silicon pins inside the flow	62
Figure 73: Calibration curve of the glucose monitor	62
Figure 74: Schematic of bonding processes (a) built-in heater configuration (b) reusable heater configuration	64
Figure 75: Temperature distribution of substrates after 0.25second of heating period (a) built-in heater with silicon substrate (b) reusable heater with plastic substrate.	65
Figure 76: Bonding results of various substrate materials	66
Figure 77: A dome shape is formed under SEM micrograph of MYLAR to PMMA showing good seal is achieved	67
Figure 78: SEM micrographs of bonding interface	68
Figure 79: Photograph of water encapsulation result	68
Figure 80: Conceptual design of a polypyrrole (PPy) micro-gap sensor array	69
Figure 81: A micro-gap sensor	70
Figure 82: Pt electrodes	70
Figure 83: (a) Humidity sensing results showing conductivity change for different PPy film thickness (t) and (b) pH sensing results showing decreasing conductivity with increasing pH	71
Figure 84: General scheme of polypyrrole conduction	73
Figure 85: Glucose sensor	74

Figure 86: PPy and PPy-MWNT	74
Figure 87: Conductivity v. Glucose Concentration	75
Figure 88: The nominalized conductivity and resistance of the microgap PPy-MWNT sensor	76
Figure 89: Diagram of control and sensing circuit	76
Figure 90: Parallax microprocessor (left) and LED (right)	77
Figure 91: The housing unit of the system	77
Figure 92: The design of the second-generation signal processing unit	78
Figure 93: Schematic of a liquid-electrolyte microbattery	79
Figure 94: Working principle of the microbattery	79
Figure 95: SEM micrograph of capped microbattery before inserting liquid-electrolyte	80
Figure 96: Measured voltage of the microbattery with a load resistance of $1M\Omega$	80
Figure 97: Working principle of the water activated microbattery	81
Figure 98: Fabrication process for the microbattery	83
Figure 99: SEM micrograph of a fabricated microbattery	84
Figure 100: Magnified SEM micrograph of Figure 99	84
Figure 101: Measured voltage of the 8mmx8mm microbattery with AgCl as the cathode and a 100 μ m-high chamber	85
Figure 102: Measured voltage of microbatteries with AgCl as the cathode and a 100 μ m-high chamber discharged at 1k-ohm	85
Figure 103: Measured voltage of the 12 mmx12mm micro-battery with a 100 μ m-high chamber discharged at 1k-ohm	86
Figure 104: Measured voltage of the 12mmx 12mm microbattery with AgCl discharged under a load resistor of 1k-ohm	86
Figure 105: Operational principle of a microbial fuel cell	87
Figure 106: Design of a miniaturized microbial fuel cell	87
Figure 107: Fabrication process of the silicon micromachined microbial fuel cell	88
Figure 108: SEM micrograph showing the fluid port and micro channel of the micromachined microbial fuel cell	89
Figure 109: Cross-sectional view of micromachined microbial fuel cell	89
Figure 110: An assembled micromachined microbial fuel cell	89
Figure 111: Open circuit measurements	90
Figure 112: Discharge	91

LIST OF TABLES

Table 1. Results for Valves with 250 μm and 500 μm Wide Channels.....	41
Table 2. Power Requirements of Micro Pumping Mechanisms.....	46
Table 3. Test Matrix for Evaluation of Hydrophobic Surfaces.....	53
Table 4. Reduction Potential and Weights of Chemicals.....	82
Table 5. Theoretical Performance of Mg-CuCl and Mg-AgCl Microbatteries.....	83

1. EXECUTIVE SUMMARY

In responding to the needs for a sample acquisition and delivery microsystem, the Berkeley Sensor & Actuator Center (BSAC) of the University of California at Berkeley has developed the technologies for a fully integrated, fully regulated microfluidics system. Generally, this system includes the acquisition, metering, buffering, delivery and assay of fluid biological samples. Specifically, this system includes “power pressure sources,” “local control of flow,” and “chip-scale sample collection platforms” to develop integrated microfluidic components in BioFlips (bio-fluidic chips). Several MEMS BioFlips components and subsystems have been demonstrated, including water-powered micro actuators, water-powered micro pumps, water-powered micro drug delivery systems, low-leakage and low-power micro valves, micro accumulators, micro dialysis needles, micro enzymatic glucose monitors, micro-gap bioassay sensors, water-powered micro batteries and micromachined microbial fuel cells. These major accomplishments have been disseminated by various publications, including 9 journal papers and 21 conference papers (Appendix I and II, respectively), 7 overview presentations in conferences, and 6 project presentations at research institutes.

2. INTRODUCTION

This research responds to the need for a low power, constant-operation, self-contained and long shelf-life biological sample acquisition and assay system. The Berkeley Sensor & Actuator Center (BSAC) of the University of California at Berkeley, in conjunction with the ALZA Corporation, teamed up to develop the technology for a fully integrated, fully regulated system for the acquisition, metering, buffering, delivery and assay of fluid biological samples as shown in Figure 1. The fluidic actuation in this system is based upon an innovative, water-powered, micro osmotic pump that is a constant flow rate device in which the osmotic membrane and cross sectional area of the osmotic salt determine the basic flow rate. The volume increase of the salt displaces the piston and delivers the working fluid. ALZA Corporation has developed macro scale osmotic pumps with flow rates ranging from 0.016 $\mu\text{l/hr}$ to greater than 10 $\mu\text{l/hr}$. If the output flow is obstructed, these pumps will develop pressures of more than 3000 psi. Thus, an osmotic pump is highly resistant to fouling by biological materials.

The redesign of osmotic pumps for Micro Electro Mechanical System (MEMS) compatible fabrication processing means that valves, reservoirs, accumulators, and other interconnects can all be integrated on silicon or plastic. This makes it possible to draw a sample of fluid and then deliver it, after metering and buffering, to a bioassay system downstream. A precisely prescribed volume of biological fluid is delivered on-demand to the electrochemical bioassay subsystem. The prescribed volume first passes into a channel where the lactate in the sample is enzymatically reacted to create hydrogen peroxide. The prescribed volume that now contains hydrogen peroxide is passed to a channel where the hydrogen peroxide is electrochemically reduced to water. During this reaction, a measurable electric charge is generated proportional to the original lactate concentration. The enzymes are not consumed in the reaction, so there is no need to replace any components after each assay. Thus, the assay runs continuously.



Figure 1: A complete water-powered bioassay system in a wristwatch

The six major tasks of this effort, which are discussed in detail in the next chapter, are: I. Water-powered micro osmotic pump, II. Ultra low-leakage, low power gate valve, III. Fore-and-Aft Throttled Osmotic Pump (FATOP), IV. Micro dialysis needle, V. Complete water-powered bioassay system and VI. Water-based micro power generation.

3. METHODS, ASSUMPTIONS AND PROCEDURES

This project has been divided into several tasks leading to the development a long life wristwatch-sized bioassay system. The issues addressed here can be categorized as relating to power, sample acquisition and assay. Of particular interest is the development of a micro dialysis needle, an osmotic pump system and an enzymatic assay system.

The micro dialysis needle will allow the acquisition of lactate from interstitial fluid in the human body. The implementation of dialysis at the point of sample acquisition in the interstitial layer of skin unburdens the system from many subsequent sample preparation issues in more conventional systems such as the separation of red blood cells from the sample.

The osmotic pump provides pumping power from the introduction of water. Electrical power is not needed for the transport of fluid, and this elimination of electrical pumping power makes it possible for the overall system to have an extremely long life. Further, the development of microvalves requiring only power in the micro-Watts range for actuation means that a standard wristwatch battery can power the water-powered bioassay system for 1 to 3 years.

Finally, the use of an enzymatic reaction to convert the lactate to hydrogen peroxide makes possible continuous system testing. The enzyme is not consumed in the assay process, and the assay fluid is intermittently pumped through the system on an ongoing basis, with an assay done each time a new slug of fluid is passed through the system. A potential of 0.4 V across two electrodes is required in the analysis channel to cause the hydrogen peroxide to be reduced. With 10 μ amps a typical current, the total power required to sense lactate is only 4 μ Watts. The enzymatic reduction bioassay modules do not have to be renewed or replaced between assays.

This research is focused on the solution of the technical problems that make the implementation of such a system possible. Thus, the first task, Water-Powered Osmotic Pump, was to fabricate osmotic pumps in MEMS technologies. This allowed the integration of the osmotic pump directly into the acquisition and assay system. The second research task, Ultra Low-Leakage Hydrophobic Gate Valve, was to devise new valve designs for low fluid leakage. Previous research had already resulted in microvalves of extremely low power, and so the emphasis of this research task was to focus on the fluidic issues, since the power consumption issues were well in hand. The third research task, Fore-and-Aft Throttled Osmotic Pump, took the results of the first two tasks and produced a functional fluidic sample transport system by adding an accumulator and combining the microvalves with an osmotic pump. In this task, the technology required to move the fluid biosample was both integrated and characterized so that a functional system could be designed. The fourth and fifth research tasks possible the actual acquisition of the fluid biosample and the actual assay. Task four, Micro Dialysis Needle, explicitly focused on the fabrication of dialysis membranes on the surface of the microneedles so that sample fluid could be painlessly drawn from an interstitial layer of skin. Nerve endings do not reach up to this layer of skin, so it is not possible to generate sensory input with the needle. In the fifth task, Water-Powered Bioassay System, the enzymatic assay was implemented, and all of the components were integrated into a wristwatch-sized case. Finally, in the sixth task, Water-Based Micro

Power Generation, electrical power was generated directly from either bacteria-based microbial fuel cells or water-based electrochemical reactions such that no conventional battery was needed in this research.

3.1 Water-Powered, Micro Osmotic Pump

The conventional osmotic pumps were redesigned for MEMS technology, eliminating the use of stainless steel ampoules for osmotic pump housings. This allowed for the incorporation of micro osmotic pumps into complex micro fluid flow systems without significant interconnects and with minimal dead volume. In Figure 2 is shown the schematic diagram of a MEMS osmotic pump fabricated using deep reactive ion etching (DRIE) and microencapsulation schemes developed at UC Berkeley to package the osmotic salt and the osmotic membrane as well as a flexible piston that dispenses the working fluid. As water is drawn across the osmotic membrane into the osmotic salt, the osmotic salt expands and slowly displaces the piston. The working fluids, whether just water, a drug to be delivered, a buffer or a reagent, were thereby expelled by the piston. No electricity is required to operate the osmotic pump, and so a major electrical power draw is eliminated.

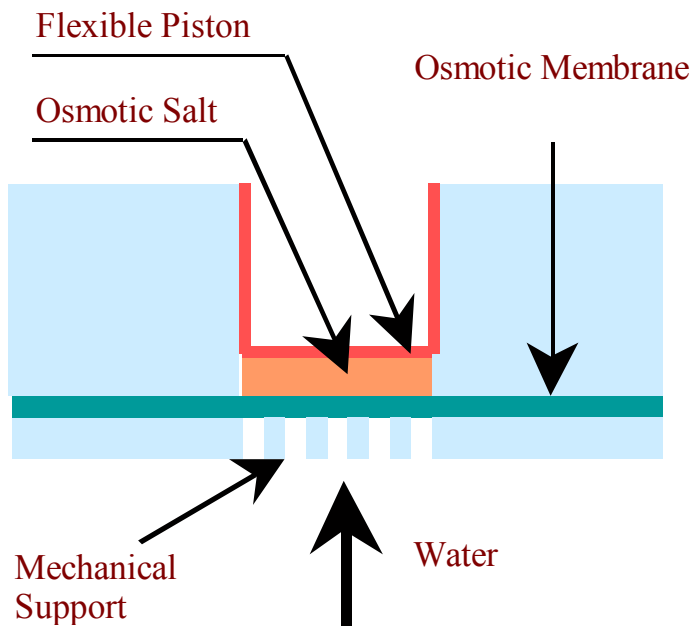


Figure 2: Micromachined osmotic pump

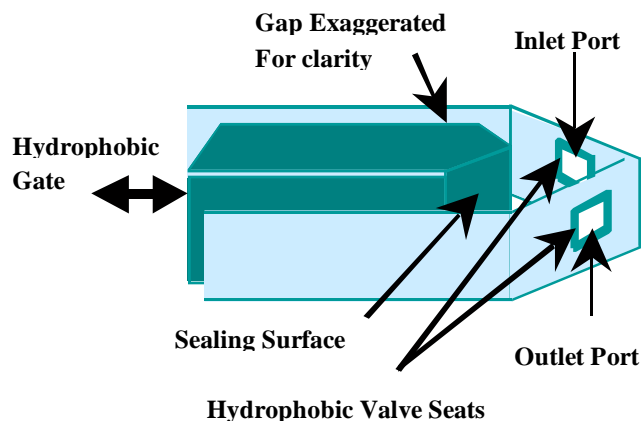


Figure 3: Schematic diagram of hydrophobic gate valve for ultra-low leakage fluidic control

3.2 Ultra Low-Leakage, Ultra Low-Power Hydrophobic Gate Valve

An ultra low-leakage gate valve that operated at ultra low-power was developed. Since osmotic pumps have flow rates in the orders of 0.016 to 10.0 $\mu\text{l/hr}$, a new, low-power microvalve was developed with a leakage rate in the order of 1 nl/hr. Previously, BSAC had achieved low-power (4.3 μW) micro valves, but with leakage rates as high as 2.35 $\mu\text{l/hr}$ at 1 atm¹. The high leakage rate of the previous micro valves required a reduction by several orders of magnitude to be suitable for the regulation of flow from micro osmotic pumps. Therefore, a new electrolysis actuation scheme requiring lower power consumption was developed for the new ultra-low leakage valves. In Figure 3 is shown the hydrophobic gate valve in which the rectangular gate was redesigned to be tapered at the end to increase the seating forces. Further, the new gate had hydrophobic surface to reduce the ability of the fluid to wick past. Finally, two raised valve seats at the inlet and outlet ports of the valve enhanced sealing by providing a much smaller width leakage path past the valve gate.

3.3 Fore-and-Aft Throttled Osmotic Pump (FATOP)

As shown in Figure 4, two hydrophobic gate valves and a flow accumulator were added to the water-powered micro osmotic pump. This integrated fluid delivery system was a **Fore-and-Aft Throttled Osmotic Pump**. The fore-throttling valve regulated the amount of water that reached the osmotic membrane. This valve experienced a maximum pressure drop of just one atmosphere and effectively controlled the average flow rate through the osmotic pump. Since throttling the fluid supply sets the overall working fluid delivery rate, this was the primary regulation scheme for the osmotic flow rate. However, these adjustments required a long time to take affect and, depending upon the particular design of the osmotic pump, closing the fore throttling valve may not significantly alter the output flow rate for from 1 to 4 hours.

1. "MicroFLUME System for Reconstitution of Biological and Medical Supplies"

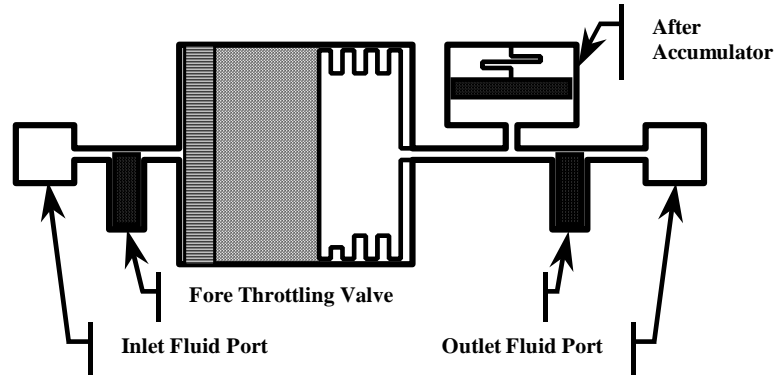


Figure 4: Fore-and-Aft Throttled Osmotic Pump (FATOP)

The water-powered micro osmotic pump of Figure 2 is augmented with a fore throttling valve, an after throttling valve and an accumulator. This allows the adjustment of both the average flow rate through the device (using the fore throttling valve) as well as high-bandwidth flow regulation (using the after throttling valve and accumulator).

Thus, as seen in Figure 4, an after accumulator and an after throttling valve provided high-bandwidth flow rate regulation to the osmotic pump. The accumulator simply acquired excess working fluid displaced by the osmotic pump when the after throttling valve was closed. The accumulator stored the pump output at lower pressure, and not at the maximum osmotic pressure of 3000 psi, so that excessive working pressures were avoided. The fore throttling valve was set to provide the correct average working fluid delivery rate, and the after throttling valve was used to generate variations in the flow. In this way, nearly any working fluid flow schedule can be generated. A FATOP can now be designed and fabricated for any specific flow rate.

3.4 Micro Dialysis Needle

A microneedle was fabricated with a porous integral separation membrane. Inside the needle a dialysis fluid can flow, and by diffusion the dialysis fluid will acquire

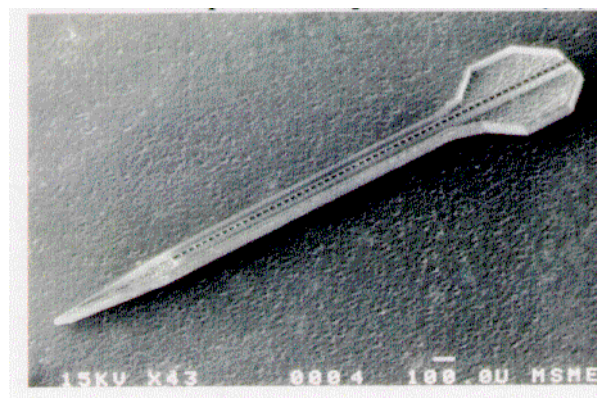


Figure 5: Hollow, Dual-Channel Micro Dialysis Needle

lactate from body fluids. This dialysis fluid is drawn into the water-powered bioassay system via the FATOP fluidic system. A micro dialysis needle is shown in Figure 5. This newly designed needle had a strengthening rib of 20 mm crystalline silicon, upon which was fabricated a 10 mm micro dialysis membrane. The dialysis fluid will flow between the membrane and the strengthening rib, and will never enter the tissue.

3.5 A Complete Water-powered Bioassay System

A complete, biocompatible system for the acquisition, metering, buffering, delivery and assay of fluid biological samples was designed, built and characterized. FATOP was used as a programmable buffer solution delivery system. FATOP, working in conjunction with the double-T metering section, delivered precisely metered fluid biological samples (each with isolating buffer on each side) at significant pressure to a downstream bioassay device. A metering section just 5 μm wide, 10 μm deep and 100 μm long dispensed fluid in 5 pico-Liter increments. A second FATOP, minus the after throttle, was used to evacuate a water reservoir. The evacuated water reservoir was used as a suction source to draw a fluid biological sample into the inlet. Subsequently the fluid biological sample was drawn completely across the double-T metering section. The first FATOP delivered a prescribed amount of buffer solution, sweeping the metering section clean of the fluid biological sample and thereby delivering it to the downstream bioassay devices.

The sample then progressed to the enzymatic reaction channel where a stoichiometric reaction with lactate oxidase created a molar concentration of hydrogen peroxide identical to the original lactate concentration in the sample. Finally, the sample progressed to the electrochemical channel where the hydrogen peroxide was reduced, providing a quantity of electrical charge proportional to the original quantity of lactate. Two assembly/integration processes are illustrated in Figure 6. Localized bonding techniques with nearly room temperature thermal budgets were used to implement the bonding process without damaging the temperature sensitive biological samples or osmotic salts.

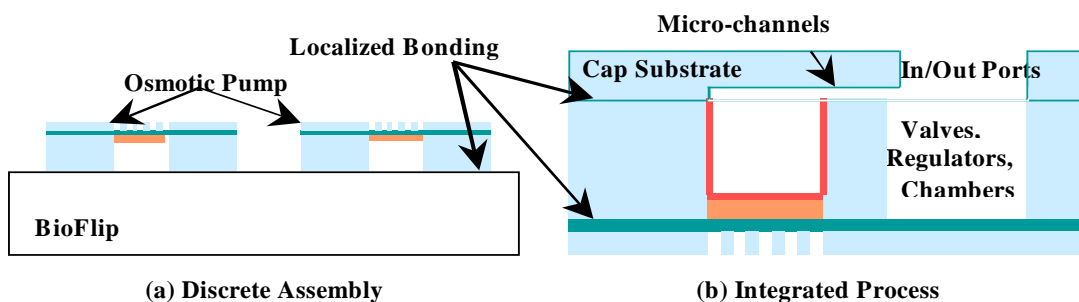


Figure 6: Schematic diagram showing the integration of the water-powered micro osmotic pump into the same substrate as the bioassay system

In each of the two methods used, the low-temperature localized bonding results from DARPA-supported research at the University of Michigan were used.

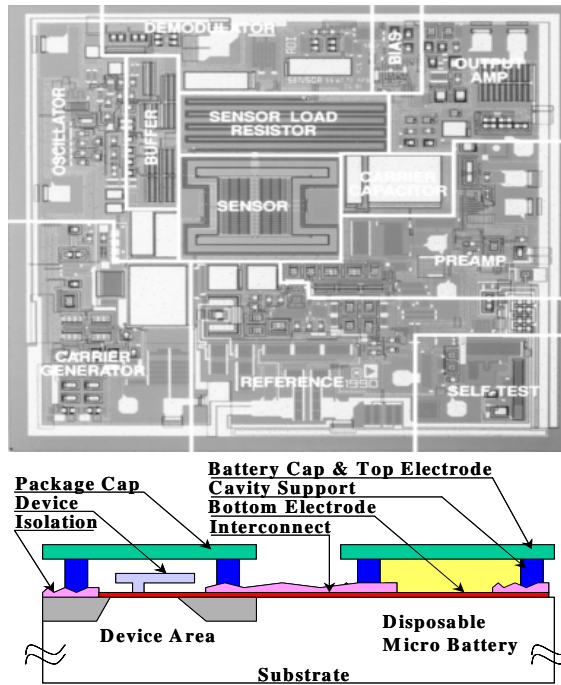


Figure 7: A microaccelerometer (top) and the schematic diagram of the packaging cap and the integrated micro power source

3.6 Water-Based Micro Power Generation

In Figure 7 is shown a microaccelerometer fabricated by Analog Devices Inc. The chip had a mechanical sensor of about $500 \times 500 \mu\text{m}^2$ at the center surrounded by microelectronics and was powered by external power sources. The second approach of this project was to develop microbial fuel cells that convert power from microorganisms utilizing an ion-exchange film as shown in Figure 8. This kind of power source is expected to work and generate power in body environments.

The research is based on wafer-level post-processing that is expected to be applicable for different types of MEMS manufacturing processes to provide disposable power or microbial power to various applications. In both application areas, it is desirable that these power sources be directly integrated with active devices without consuming extra device areas. Furthermore, the power generation method uses a low temperature process to prevent high temperature damages to the MEMS/NEMS devices that are adjacent to the power sources. Many other micro power generation projects use combustion to generate power, but they generate too much heat, and therefore are not applicable for these applications.

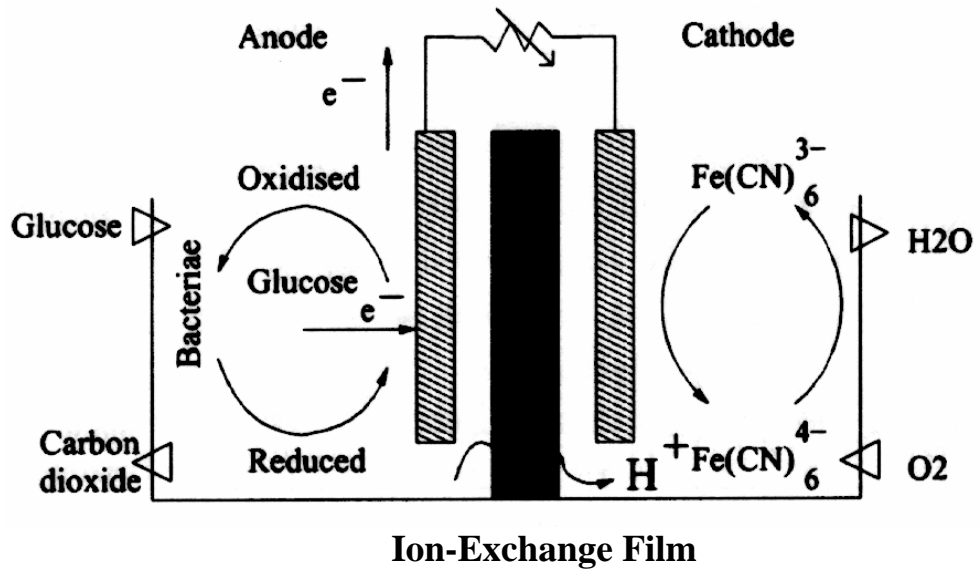


Figure 8: The working principle of the microbial fuel cell by using an ion-exchange film to convert power from microorganisms

4. RESULTS AND DISCUSSION

4.1 Water-Powered, Micro Osmotic Pump

We have successfully demonstrated and characterized the first micro scale osmotic actuator and the first micro osmotic pump. When combined with other components, these are the foundations of a working water-powered bioassay system. Furthermore, we have successfully applied localized plastic bonding technique to bond plastic-to-plastic materials, plastic-to-silicon and plastic-to glass with liquid encapsulation capability for the integration of various BioFlips components. These new technologies are discussed below.

4.1.1 Water-Powered, Osmotic Microactuator

This work presents a microactuator that draws power directly from water and produces mechanical actuation without any electrical energy consumption. The microactuator is made of cellulose acetate with a cylindrical cavity of 0.5 to 1.5mm in diameter and 0.4 to 1mm in depth. These cavities are filled with sodium chloride, and a polyvinylidene chloride copolymer diaphragm is spun on as the cover. Using osmosis for the first time on the microscale, this water-powered, osmotic actuator can provide both high pressure (up to 35.6MPa) and large actuating displacement (up to 0.8mm as measured with an actuator of 0.8mm in diameter). Incompressible water flow controlled by membrane characteristics and chemical potential enables the direct energy conversion to provide mechanical actuation. Measurement results show that constant volume change of 4 to 15nl/hr can be achieved depending on the design. When integrated with other microfluidic devices, this osmotic microactuator can serve as a clean, compact and inexpensive fluid power source.

Previously several different types of microactuators that were based on different physical and chemical principles have been fabricated and investigated for potential applications to MEMS. Most existing microactuators are driven by externally supplied electrical power. For applications where electrical power is not available or is difficult to supply, alternative types of power are required. Very little work has been done in this area. Osmosis has been utilized on macroscale devices for generating fluid pressure, and these devices store energy that can be used over for long time durations. When applied to the microscale, osmosis offers attractive features based on a purely chemical actuation principle: it is controllable by membrane characteristics utilizing the incompressible flow of water as a driving force [1]. Previously, macroscale osmotic pumps with diameters as short as 6mm with a length as short as 15mm have been developed [2,3]. This work presents the first operational, micromachined osmotic actuator for the promising applications in microfluidic systems and power sources for MEMS devices.

In Figure 9 is shown the schematic diagram of the osmotic actuating principle. When the osmotic microactuator is supplied with water through the inlet port, there is a net flux of water across the semipermeable membrane (osmotic membrane) into the chamber that contains the osmotic driving agent (osmotic salt). The flow is controlled by the permeability of the osmotic membrane, the osmotic pressure of the driving agent, and the hydrostatic pressure difference across the membrane. The outside walls of the

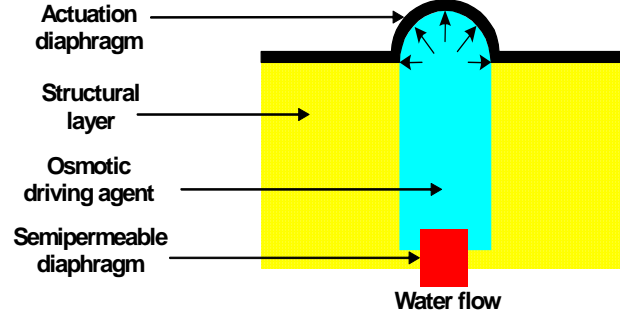


Figure 9: Schematic of osmotic actuation

Actuators and membranes are rigid and nondeformable. By virtue of the incompressibility of water, the volume of water entering the chamber is equal to the expansion volume of the chamber. The osmotic flow rate of water can be written as [2]:

$$J = KA(\sigma\Delta\pi - \Delta P) \quad (1)$$

where J is the flow rate (volume of water transported per unit time), K is the permeability of the membrane to water, and A is the effective surface area of the osmotic membrane. When water diffuses across the osmotic membrane, the hydrostatic pressure inside the cavity increases and ΔP is the difference of the hydrostatic pressure across the osmotic membrane that has a negative effect on the flow rate. On the other hand, $\Delta\pi$ is the difference in osmotic pressure across the membrane that has a positive effect on the flow rate. An osmotic reflection coefficient, σ , of the membrane is used to account the driving agent as it diffuses outwards through the membrane. If σ is equal to 1, the driving agent will not diffuse outwards. Water is able to diffuse through the osmotic membrane into the chamber if the difference in osmotic pressure is higher than that of the hydrostatic pressure across the membrane. The osmotic pressure can be represented as following [2]:

$$\pi = S \cdot i \cdot RT \quad (2)$$

where S is the solubility of the driving agent in water, i is the number of ions or particles per mole in solution, R is the ideal gas constant and T is absolute temperature. Since osmotic pressure can go as high as 356atm [4], water can flow inside the cavity to cause the hydrostatic pressure to increase such that the actuation membrane is forced to deform outwards as shown. By using standard theories of shell and plate, the deformation and radial stress of the plastic actuation membrane can be approximated by the following equations [5]:

$$w_0 = 0.662a^3 \sqrt{\frac{qa}{Eh}} \quad (3)$$

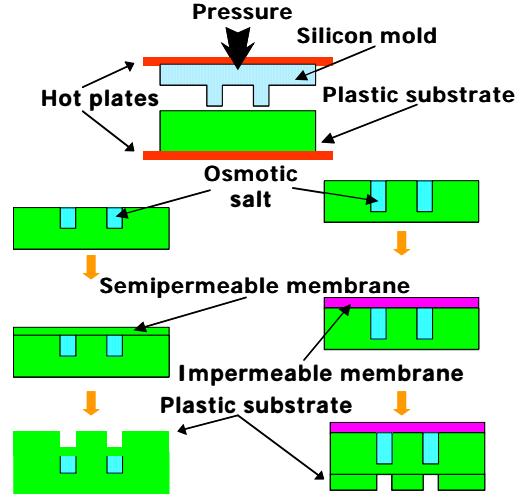


Figure 10: One-mask fabrication process of osmotic microactuators

where w_0 is the maximum deflection at the center of the membrane, a and h are the radius and thickness of the membrane, respectively. E is the Young's modulus and q is the applied pressure.

Two types of osmotic microactuators, including the semipermeable-piston type and the impermeable-piston type, are fabricated by using a one-mask fabrication process as shown in Figure 10. The semipermeable-piston type actuator uses the same semipermeable membrane as both the actuation membrane and the osmotic membrane such that water is directly diffused into the cavity via the actuation membrane as shown. The impermeable-piston type actuator uses an impermeable material as the actuation membrane and water is diffused into the cavity from the osmotic membrane from the backside of the cavity.

The manufacturing process starts with the making of silicon mold inserts by using the Deep Reactive Ion Etching process to construct the molds to be used in a micro hot embossing process [6,7]. Osmotic chambers of 0.5~1.5mm in diameter and depths of 400 to 1000 μ m are designed. Cellulose acetate sheets of two thickness, 0.5mm and 1mm, are used to fabricate the actuator body. Because cellulose acetate is semipermeable to water, it is also used as the actuation membrane in the semipermeable-piston type actuator as shown in the left side of Figure 10 and as the osmotic membrane in the impermeable-piston type actuator as shown in right side of Figure 10. The micro hot embossing process is applied to make micro cavities on the surface of the plastic sheets. A constant pressure of 0.2MPa is applied throughout the hot embossing process, including the imprinting stage and the cooling stage to obtain good replications. The standard process takes about 30~50 minutes at an elevated temperature of 130 $^{\circ}$ C followed by a 15 minutes of cooling period [8]. When the depth of the cavity is properly designed, this hot embossing process can fabricate about 100~400 μ m thick of osmotic membrane at the backside of the cavity for the impermeable-piston type actuator. However, if the desirable thickness of the osmotic membrane is less than 100 μ m,

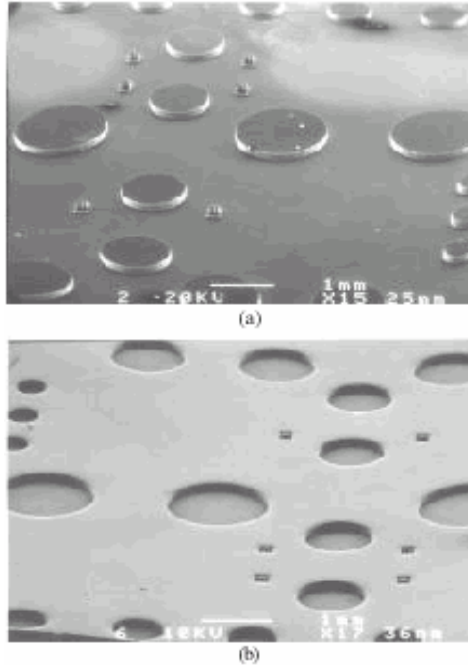


Figure 11: SEM micrographs of silicon mold (a), molded cellulose acetate substrate (b)

this thin membrane must be solvent-bonded on the backside of a through-hole cavity. Sodium chloride powder is then manually placed into the cavities as the osmotic driving agent. Any extra salt spilled on the substrate is removed to keep the surface flat. In the case of semipermeable-piston actuator, cellulose acetate that plays the dual role of osmotic and actuation membrane is dissolved in acetone and spin-coated to form the top membrane and seal the osmotic salt. A thickness of 20 μm is used such that the membrane is permeable to water but not to the osmotic salt. For the impermeable-piston type microactuator, an impermeable membrane consisting of Saran F-310 solvent-soluble barrier polymer (vinylidene chloride and acrylonitrile copolymer) is employed as the actuation membrane. The powder of Saran F-310 resin is first dissolved in solution of 65% methyl ethyl ketone and 35% toluene up to 20% of the total weight. The mixture is kept in 23°C for one hour until powder is completely dissolved. Another cellulose acetate substrate that uses mechanical drills to define the water inlet of 500 μm thick is aligned and solvent-bonded on the backside of the substrate. Figure 11 shows SEM micrographs of the silicon mold-insert and molded cellulose acetate substrate. A good replication is illustrated. The cross sectional views of both semipermeable-piston type and impermeable-piston type microactuators are shown in Figure 12, where the osmotic salt is removed. The semipermeable-piston type microactuator shown in Figure 12(a) has actuation membrane thickness of 20 μm , osmotic cavity diameter of 1.5 mm and depth of 500 μm . The 500 μm -thick layer at the bottom of the osmotic cavity is enough to prevent water penetration during the lifetime of the experiments. Therefore, the top piston membrane serves for both purposes of water inlet and osmotic actuation. On the other hand, the impermeable-piston type microactuator shown in Figure 12(b) has osmotic membrane thickness of 100 μm , actuation membrane thickness of 40 μm and osmotic

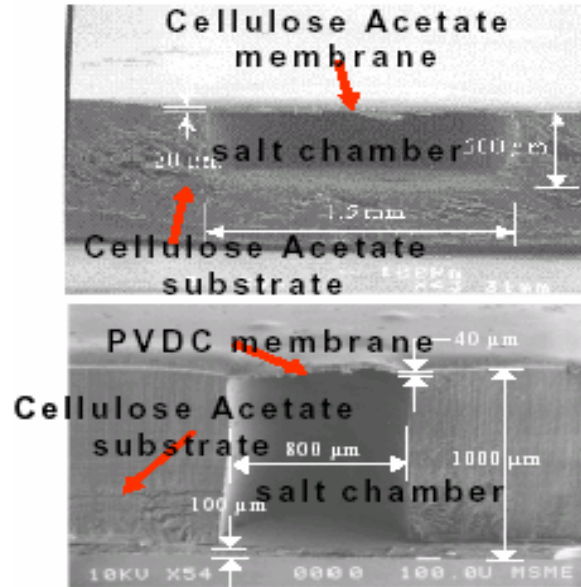


Figure 12: Cross sections of a (a) semipermeable-piston type and an (b) impermeable-piston type osmotic microactuators

cavity of 800 μm in diameter and 1000 μm in depth. Figure 13 shows the SEM micrographs of an impermeable-piston type microactuator before and after the actuation caused by osmotic reaction. Before the actuation, the actuation membrane is relatively flat. After the actuation, a dome shape structure is formed in Figure 13(a). If the microactuator is cut in half after actuation, Figure 13(b) is the result showing cleavage and separation of the actuation membrane and the actuator body at the edge of the cavity.

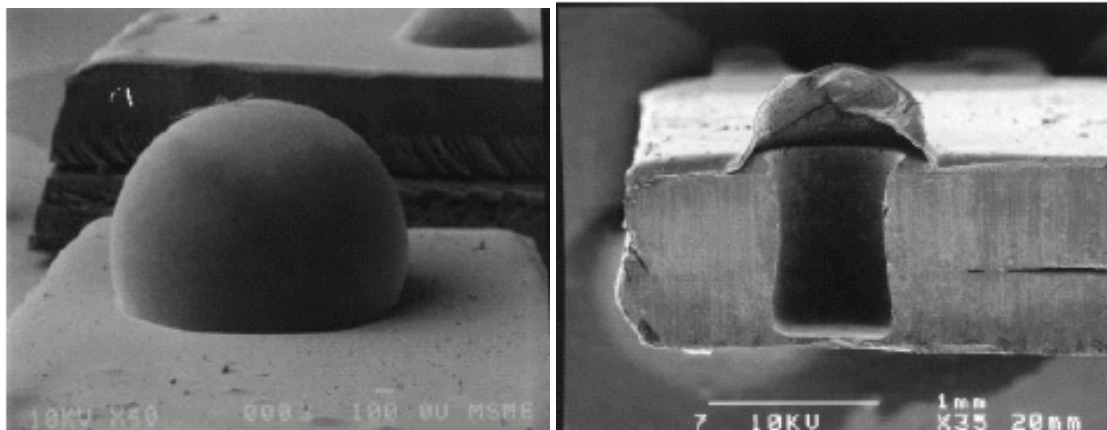


Figure 13: (a) The micro osmotic actuator has been actuated based on the principle of osmotic pumping, (b) The actuated device is cleaved in half

The cross sectional view microphoto (b) shows the semi-permeable membrane at the bottom, the osmotic chamber at the center, and the actuation diaphragm on the top.

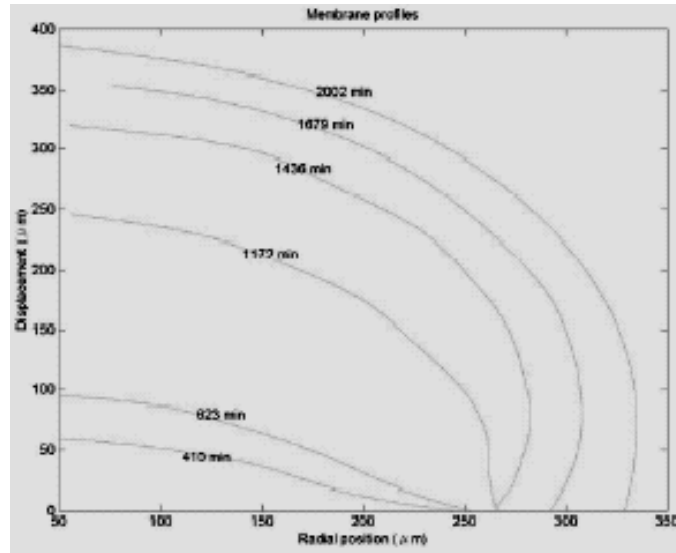


Figure 14: Measured profiles of an actuating membrane during the expansion process

The microactuator is observed under an optical microscope during the expansion process and the profiles of the actuating membrane are recorded by tilting the samples in a 90° oblique view for front view image processing. Figure 14 shows six profiles of an actuating membrane on an impermeable-piston type microactuator recorded at six different time steps up to about 33 hours when solid salt is completely dissolved. The initial diameter of the cavity is 500 μm. It is observed that the boundary of the membrane extends as time goes by. By comparing with Figure 13(b), the membrane boundary increases as the stress at the boundary can break the bond between the actuation membrane and the actuator body. The volume expansion is calculated by the integration of recorded profiles. The measured peak displacement and volume expansion versus actuating time for two impermeable-piston type microactuators are shown in Figure 15. The depth of the cavities is 500 μm with actuation membrane thickness of 40 μm and osmotic membrane thickness of 70 μm. As can be seen in the figure, there is a delay of actuation in the beginning. The measured volume expansion rates of microactuators with 0.5 and 0.8 mm diameters are 4.5 and 11.5 nl/hr respectively. During the last few records of the experiments, the increases of peak displacements seem to slow down while the increases in volume expansion remain constant. For a circular membrane of 0.8 mm in diameter, the measured peak displacement of the membrane can be up to 800 μm to generate a volume expansion of 0.65 μl. Actuators of desired characteristics can be designed and optimized by selecting the right combination of membrane dimensions, materials and the right type of osmotic salt.

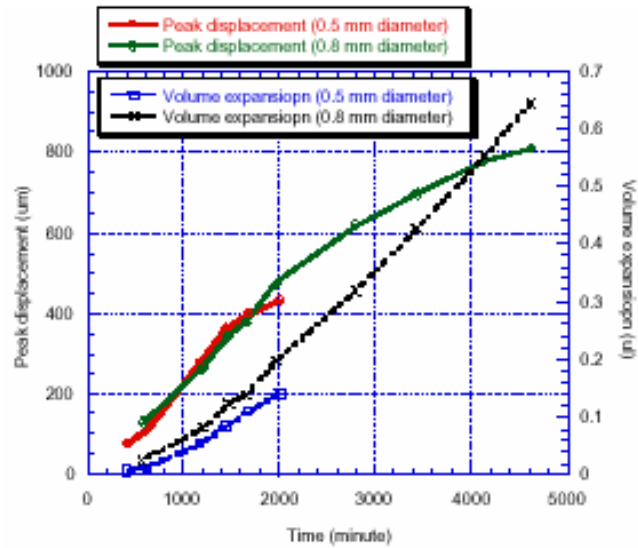


Figure 15: Measured peak displacement and volume expansion vs. actuating time characteristic of actuating membranes

4.1.2 Water-Powered, Osmotic Micropump

By integrating the osmotic actuator as described in section 4.1.1 with microfluidic channels and a working liquid, a water-powered micropump was fabricated. A schematic diagram of the osmotic micropump is shown in Figure 16. The embedded microfluidic channels in the top polydimethylsiloxane (PDMS) layer were made by a SU-8 mold casting process.

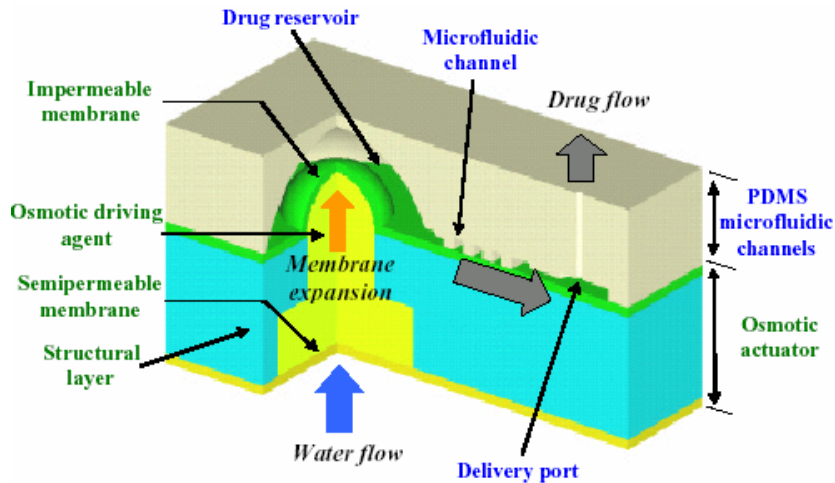


Figure 16: Schematic diagram of a micro osmotic pump system using osmotic actuator as the pumping source

Water can diffuse through the semi-permeable membrane at the bottom into the osmotic driving agent chamber and push the top, impermeable membrane. Drug stored in the reservoir is expelled by the impermeable actuation membrane via the microfluidic channel (to control the drug diffusion process). PDMS is used as the material to construct the top layer in the prototype demonstration. Microchannels with cross-sectional area of $10 \times 20 \mu\text{m}^2$ are constructed in the prototype.

Using oxygen plasma to activate bonding surfaces, sealing and liquid encapsulation can be achieved to assemble the micro-pump. Figure 17 shows the complete fabrication process. We have developed a bonding process by introducing an intermediate KRATON D1193PX styrene/isoprenestyrene copolymer layer. Both KRATON and PDMS are exposed to oxygen plasma to modify and activate surfaces for bonding. Once two surfaces are brought into conformal contact, strong bonding will be achieved. Furthermore, it is found that these plasma-activated surfaces will remain active if they are covered by water. After plasma oxidation, activated surfaces are immersed into water to fill microfluidic channels with water and aligned. This pre-bonding pair is then removed from water and placed on a hot plate at about 70°C to evaporate water between two activated surfaces and bonding is achieved afterwards. This way, water with zero dead volume is encapsulated in the microfluidic channels.

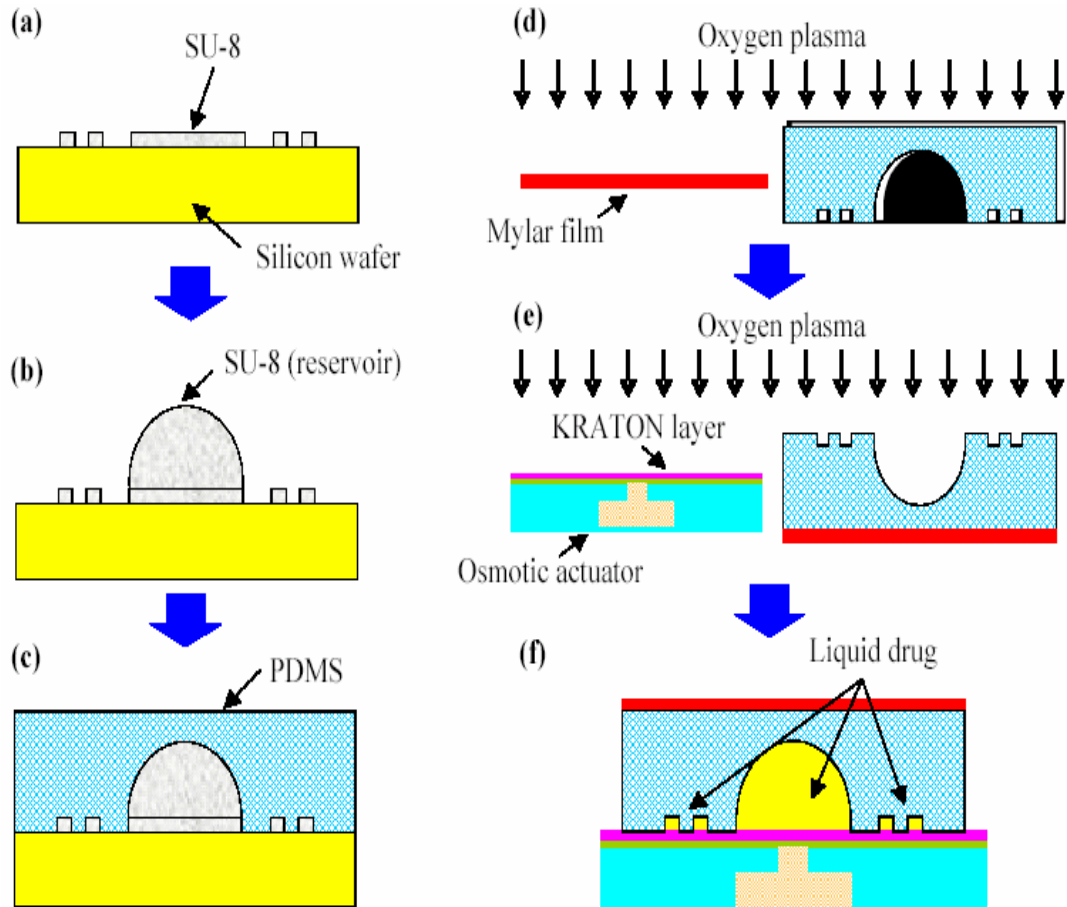


Figure 17: The fabrication process of the micro osmotic pump



Figure 18: A fabricated drug delivery system as compared with a one-cent coin

A long delivery microchannel (1cm) is designed between the reservoir and the outlet port as shown to minimize the drug diffusion effect. The total delivery volume of this prototype system is designed as 2 μl for a total delivery period of about 10 hours.

Figure 18 is the molded PDMS replica containing microfluidic channel on a US one-cent coin. The size of the system can be extremely small for site-specific delivery applications. The system can also be designed to have big drug reservoir for long-term applications but with micro features to control the delivery profiles. The cross-sectional view of the assembled micro drug delivery system is shown in Figure 19 where the thickness of the PDMS layer is 1.5 mm. The chamber that stores osmotic salt is also redesigned with two widths to increase the volume storage of osmotic salt and extend the life of the osmotic actuation. We have also improved the actuation rate up to 20 times faster than the previous results. It is noted that the drug reservoir can be easily enlarged

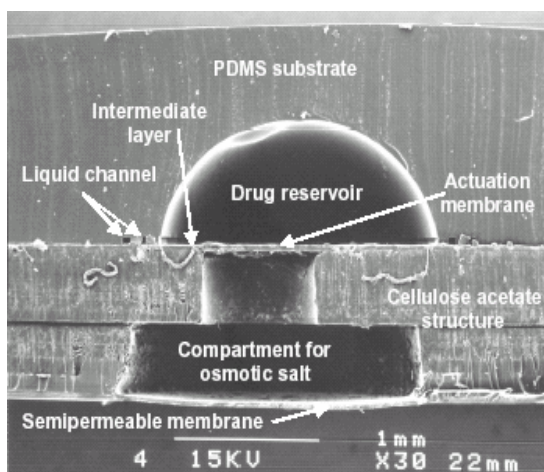


Figure 19: The cross sectional SEM micrograph of the drug delivery system

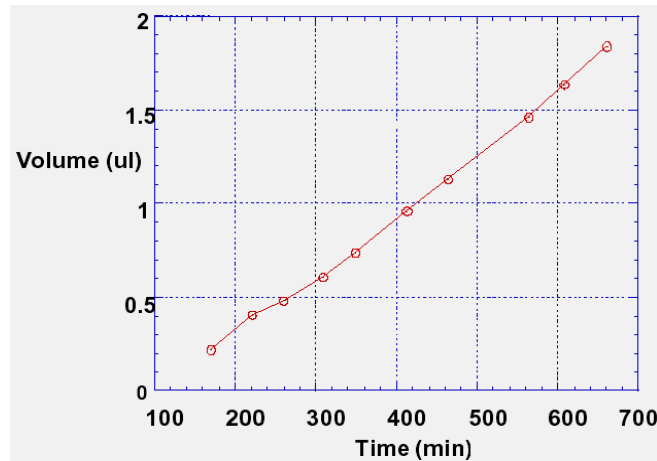


Figure 20: The measured delivery profile from the prototype micro drug delivery system

to store more drug volume for long-term applications and the semi-permeable diaphragm can be processed to be either porous or dense for short- or long-term drug delivery applications. Figure 20 shows the measured delivery volume with respect to time. The drug delivery rate is observed at $0.2 \mu\text{l/hr}$ for an operation period of 10 hours. This delivery rate is about 10 times less than the current technology used by Medtronic Inc. Slower delivery rates can be easily achieved by changing the porosity of the semi-permeable diaphragms. As such, it opens up many possibilities of shrinking the system and extending the life of the system before drug refills. We have designed this prototype for military applications where high-speed delivery rate is desirable for battlefield applications. By changing the porosity of the semi-permeable diaphragm, we can easily slow down the delivery another 100 times. Therefore, the potential of applying this technology is to shrink the overall size of the system as well as to extend the lifetime of the device by the very fine control of delivery volume. The delay of operation is observed in the first three hours and that is the time required for water to fill up the osmotic salt chamber before pushing the actuation diaphragm. Afterwards, constant delivery is observed as expected based on the operation of osmosis. These results confirm many of the osmotic systems used currently in the macro scale that constant delivery profiles can be achieved and adjusted by modifying the properties of the semi-permeable membrane.

4.1.3 Water-Powered, Osmotic Drug Delivery System

The micro osmotic pump can be considered a micro drug delivery system. The devices were characterized in a well-controlled simulated environment that simulated the liquids in a real animal or human body. The preliminary studies were conducted by inserting devices into fresh meats bought from local supermarkets. In Figure 21 shown in Figure 21 is the testing result on a piece of pork. The device was inserted between the fat and lean regions to emulate its possible placement in a live animal or human. After 10 hours, the delivery of drug was clearly observed. The important information



Figure 21: Drug delivery (colored liquid) was observed after 10 hours by inserting the system into fresh pork meat

learned from this experiment is that fresh meats still have good moisture contents to activate and actuate the drug delivery system.

The analytical model and design consideration for the drug delivery system are discussed here. The system is composed of two major parts: the osmotic actuator at the bottom and microfluidic components including the drug storage reservoir and delivery channel at the top. The details of the micro osmotic actuator have been reported previously while the top part is made of polydimethylsiloxane (PDMS) to form the drug reservoir and the microfluidic channel and delivery port. Furthermore, a layer of Mylar film is bonded on the top of PDMS film as the diffusion barrier to reduce the water diffusion process and preserve drug inside the device as shown in Figure 22. Induced by the concentration difference across the semipermeable membrane at the bottom of the osmotic actuators, water from aqueous environment is drawn through the semipermeable membrane into the chamber filled with osmotic driving agent to power the drug delivery system. By virtue of the incompressibility of water, the top actuating membrane, which is hundreds of times more flexible than the bottom semipermeable membrane, expands to

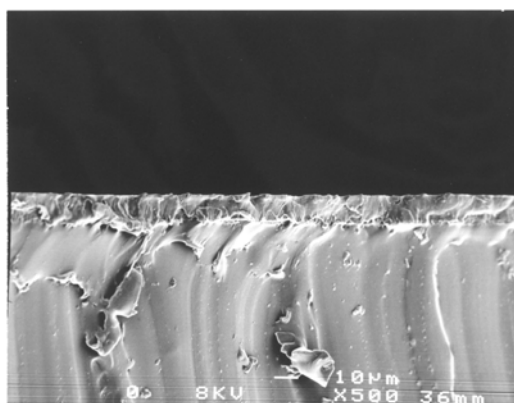


Figure 22: Cross-sectional SEM micrograph of the bonding interface between PDMS substrate and Mylar barrier film

drive and release the liquid drug stored in the reservoir. The convective flow rate of drug driven out of the reservoir can be represented as follows:

$$Q_{dc} = C_d \cdot Q_c \quad (4)$$

where Q_{dc} is the convective flow rate of drug, C_d is the concentration of drug in the formulation within reservoir, and Q_c is the overall convective flow rate of drug and its diluents, which is equal to the expansion rate of the actuating membrane. In addition to convective flow, drug is also released to outside environment through diffusion. The diffusive flow rate of drug through the delivery channel can be simplified as follows:

$$Q_{dd} = DA\Delta C_d / L \quad (5)$$

where Q_{dd} is the diffusive flow rate of drug, D is the diffusivity of drug through the delivery channel, A is the cross-sectional area of the delivery channel, ΔC_d is the difference of drug concentration between inside reservoir and outside environment, and L is the length of delivery channel. Generally, the drug concentration in the inside reservoir is much higher than the drug concentration in the outside environment such that ΔC_d can be approximated by C_d . It is desired to keep the diffusive flow rate of drug much less than the convective flow rate of drug such that the release rate of drug will be constant and controlled by osmosis. A performance index can be defined as follows:

$$I_c = \frac{Q_{dd}}{Q_{dc}} = \frac{DA}{Q_c L} \quad (6)$$

where I_c is the ratio of diffusive flow rate to convective flow rate of drug, which defines the consistency of drug flow and lower values indicate better consistency. With specified drug diffusivity and delivery rate, smaller cross-sectional area and longer length of the delivery channel will improve the consistency but also increase the pressure drop across the delivery channel, which can be represented as follows:

$$\Delta P = \frac{12Q_c \mu L}{wh^3} \left[1 - \frac{h}{w} \left(\frac{192}{\pi^5} \sum_{n=1}^{\infty} \frac{1}{n^5} \tanh\left(\frac{n\pi w}{h}\right) \right) \right]^{-1} \quad (7)$$

where ΔP is the pressure drop across the delivery channel, μ is the viscosity of the formulation within reservoir, w is the width of the delivery channel, and h is the height of the delivery channel. The pressure drop should be kept under less than 10% of the driving pressure the actuator can provide to assure normal operation of the overall system.

Flow rate measurement is conducted to verify the operation principles and design concepts and Figure 23 shows the SEM picture of the experimental setup. The released liquid flow from the fabricated micro drug delivery system is directed to a transparent polymer tube and the flow rate is estimated by tracing the movement of liquid-air interface in the tube. Polyimide tube of 310 μm in outer diameter, 275 μm in inner diameter, and 5 cm in length is inserted to the delivery port. The gap between tube and delivery port is filled by pouring and curing additional PDMS prepolymer mixture around

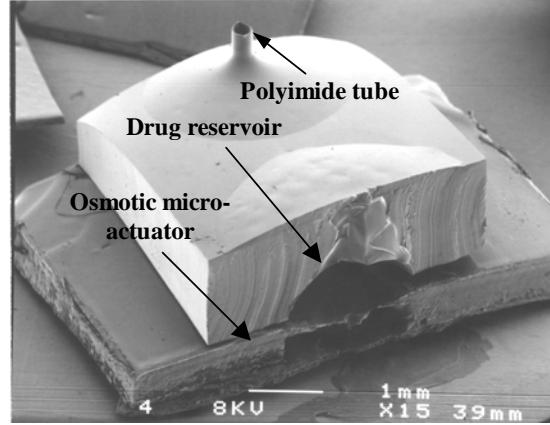


Figure 23: Measurement set up

the connection. This will prevent measurement error caused by leak. Another measurement error may come from the loss of liquid to the environment through evaporation and diffusion. To estimate the loss of evaporation and diffusion through the tube, the following equation is used:

$$Q_{dv} = \frac{D_v P M_w A}{R_0 T L} \ln \frac{P_{A_2}}{P_{A_1}} \quad (8)$$

where Q_{dv} is the rate of liquid loss through evaporation, D_v is the diffusivity through the tube, P is the total pressure, M_w is the molecular weight of liquid, A is the cross-sectional area of the tube, R_0 is the universal gas constant, T is the absolute temperature, L is the length of tube, and P_{A_i} is the partial pressure of air at each end. Using tube with small area to length ratio, this evaporation and diffusion loss can be reduced. Consider water evaporating in a tube of 5 cm in length and 275 μm in diameter at room temperature, this evaporation and diffusion loss is only 0.00256 $\mu\text{l/hr}$, which is 1.3% of the drug flow rate at 0.2 $\mu\text{l/hr}$ for an operation period of 10 hours.

4.1.4 A Frozen Water Micromachining Process

The third major accomplishment in this area is the new liquid encapsulation technique by using frozen water. In the osmotic pumping system, it is very difficult to encapsulate liquid buffer with zero or minimum dead volume. We have successfully developed a technology based on frozen water and fabricated a capillary-driven micropump as the demonstration example. The working principle of the micropump is illustrated as Figure 24. The whole device is composed of drain and source chambers connected by a long serpentine microchannel. A circle of 1300 μm in diameter defines the drain chamber and the source chamber is defined by a square of 500 μm in width. The heights of drain and source chambers are formed by water droplets that are 200 μm and 80 μm in height, respectively. Because silicon dioxide is hydrophilic, water is automatically dragged into the microchannel (self-prime) by surface tension force.

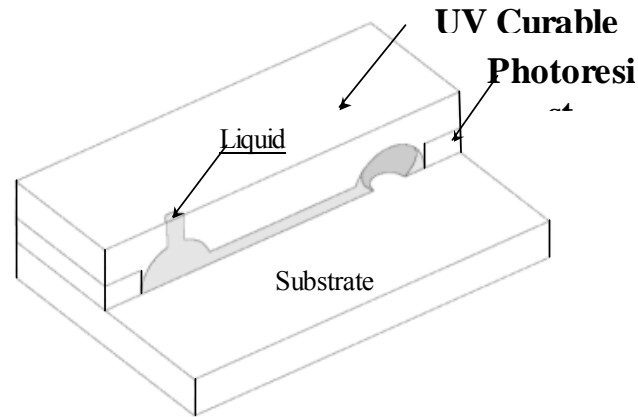


Figure 24: The schematic diagram of the disposable capillary micropump using frozen water technology

Figure 25 shows the fabrication sequence of the micropump. The process starts to grow a 0.8 μm -thick silicon dioxide on a clean silicon wafer. A 9 μm -thick photoresist (Shipley STR 1075) layer is patterned to define the microchannels and fluid reservoirs as shown in Figure 25(a). A plasma process is applied to make the surface of the photoresist hydrophobic (Figure 25(b)). Water is then poured onto the wafer. Due to the hydrophilic property of silicon dioxide, water is automatically and selectively placed into the microchannels and reservoirs as shown in Figure 25(c). The naturally formed water areas have different heights and shapes depending on the geometry of channels and the properties of hydrophobic/hydrophilic surfaces and working liquid. The substrate is then immersed into a liquid nitrogen bath for 1 minute and liquid water is transformed as solid ice as shown in Figure 25(d). The ice serves as the sacrificial layer when a 250 μm -thick UV curable polymer is coated and cured as illustrated in Figure 25(e). The water is driven out either naturally after a few days or by putting it in an oven for a few hours to complete the process as shown in Figure 25(f).

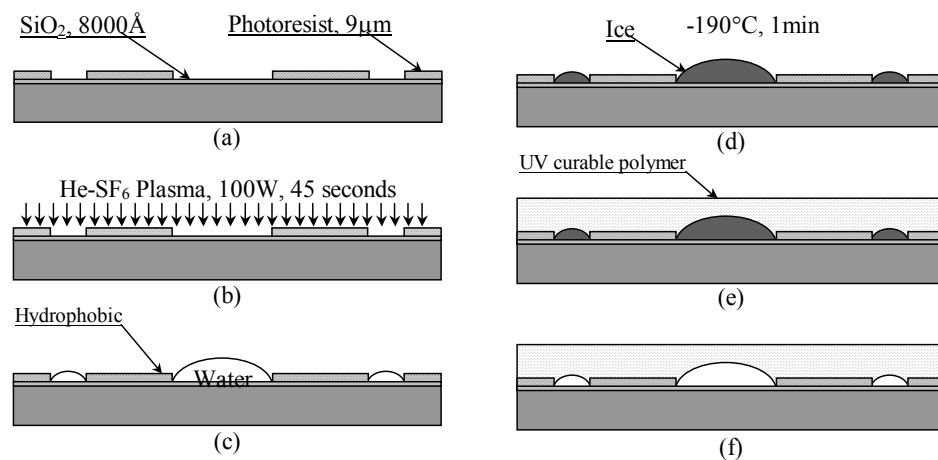


Figure 25: Fabrication sequence of the disposable micropump using frozen water as the sacrificial layer

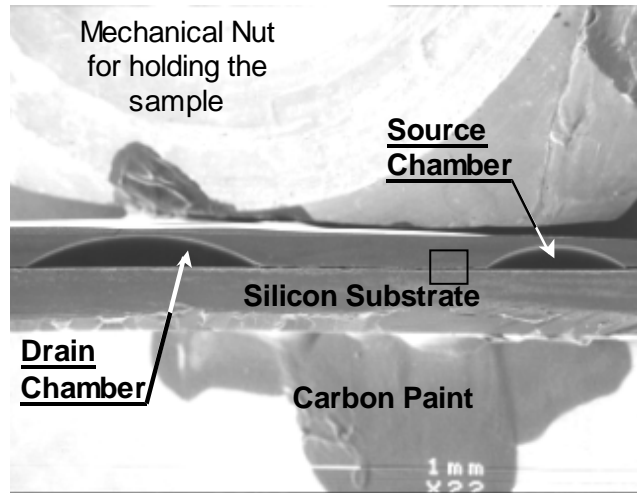


Figure 26: The SEM micrograph showing the cross-sectional view of the micro-chambers

Figure 26 is the cross sectional view of the fabricated micropump showing the drain and source chambers of $200\ \mu\text{m}$ and $80\ \mu\text{m}$ in height, respectively. The designated box area in Figure 26 is enlarged and shown in Figure 27, where the polymer layers are separated with the silicon substrate during the wafer dicing process. However, the shape of the two microchannels and the photoresist between them can be clearly observed. The estimated height of the microchannels is $5\ \mu\text{m}$ while the width is $20\ \mu\text{m}$. The total length of the microchannel is $6.5\ \text{mm}$, as shown in the Figure 28 SEM micrograph. The micropump operates when a hole is poked open and liquid is poured into the source chamber as shown in Figure 29. Capillary force drives the liquid toward the drain chamber at a high flow rate of about $2\ \text{nl}/\text{min}$ initially.

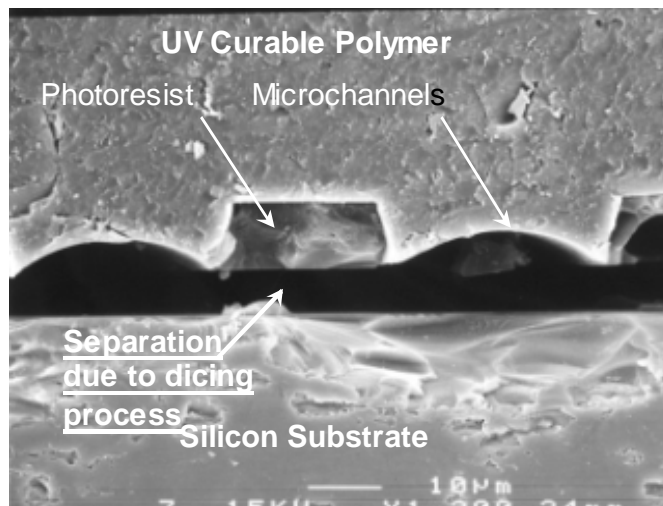


Figure 27: Higher resolution SEM micrograph of Figure 26 showing the microchannels

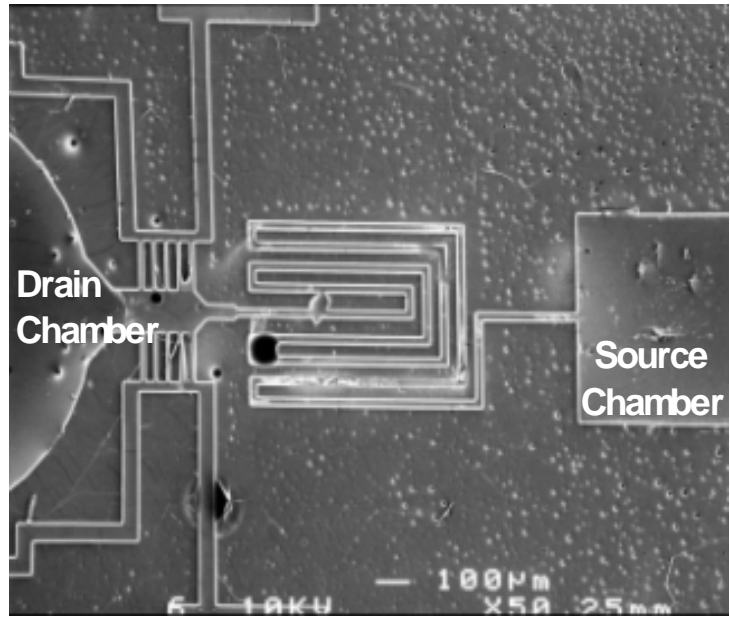


Figure 28: SEM micrograph of the micropump

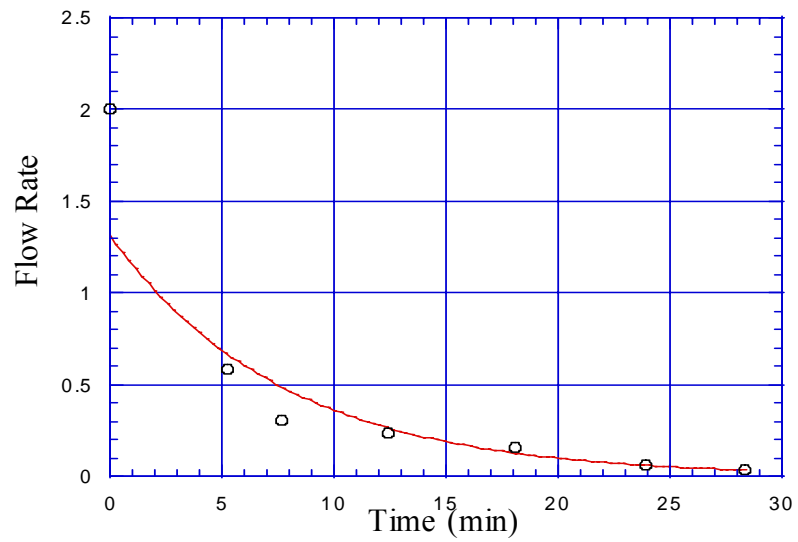


Figure 29: Measured flow rate of the one-mask, disposable capillary micropump

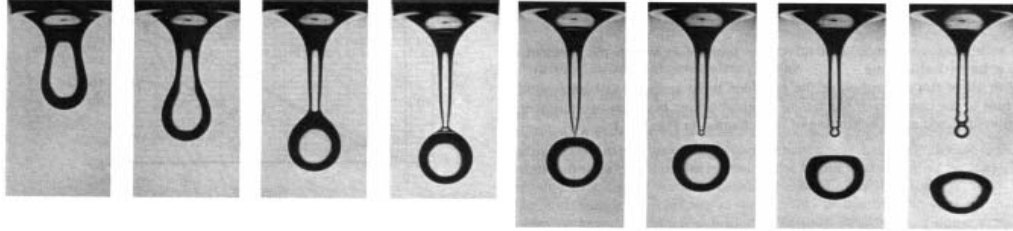


Figure 30: Slow dripping/separation of a droplet from a capillary

4.1.5 Micro Osmotic Pumping Nano Droplet Generator

Previously, we have demonstrated a micro osmotic pump that can pump microfluidics at flow rates of $2 \mu\text{l}/\text{hour}$. However, one of the important issues is the capability to separate the continuous flow for functions of mixing and buffering. This particular subtask has concentrated on the possibility to separate the continuous flow that has been generated by the osmotic pump into digital outputs. We have conducted detailed design with analytical models in this quarter. Separation of liquid segments from a continuous source has been studied for decades. For example, a pendent drop may break away under gravity as shown in Figure 30. When dimensions shrink, breakaway becomes more difficult because of stronger surface effects. Previously, researchers had presented micro droplet separation by using electro-wetting-on-dielectric, ink-jet printing, PZT actuation, or pressurized air. To achieve droplet separation, all these approaches require sophisticated actuation and control mechanisms, which are not practical for applications such as implantable drug delivery systems.

Figure 31 shows the operation principle: (a) a hydrophilic microfluidic channel is intersected by a designed hydrophobic region; (b) a steady liquid flow is driven into the hydrophobic region; (c) flow reaches the other side of the region; (d) accumulation of liquid in the hydrophobic region and enclosed air is squeezed and pressurized; (e) once surface tension (F_1) is overcome, flow reaches the entrance of the downstream microchannel and is first sucked into the hydrophilic channel; expelled out of the hydrophobic intersection; and finally squeezed by compressed air to cause necking and breakaway at the junction; (f) process completes.

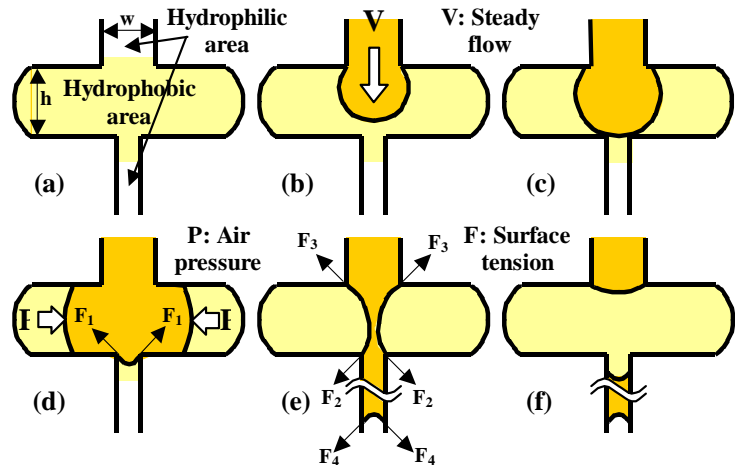


Figure 31: Microfluidic channel combining attractive and expulsive forces for flow discretization

(a) Geometry and surface properties (b) to (f) Splitting sequence

Figure 32 shows the schematic design of the proof-of-concept prototype. The liquid reservoir supplies the incoming liquid, the two air chambers are designed to store the air pressure to assist the separation process, and mask stoppers are designed to stop the masking material entering the designated hydrophilic channel regions in order to define the hydrophobic region. In operation, the pressure barrier built across the junction

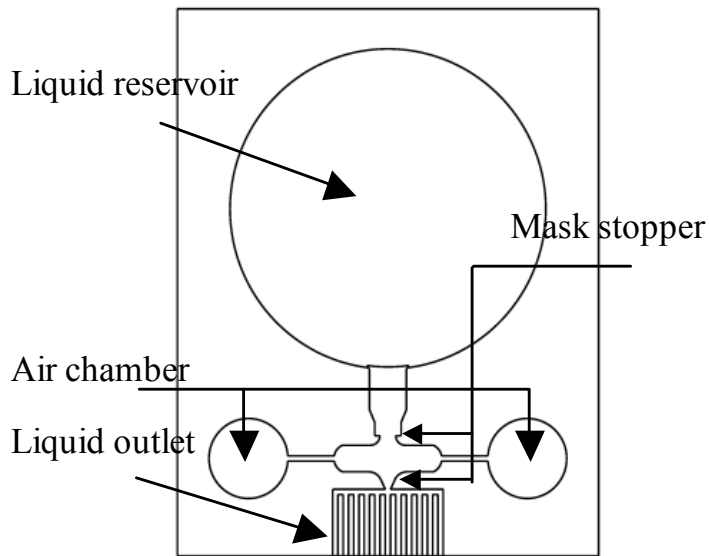


Figure 32: Schematic diagram of the flow discretizer

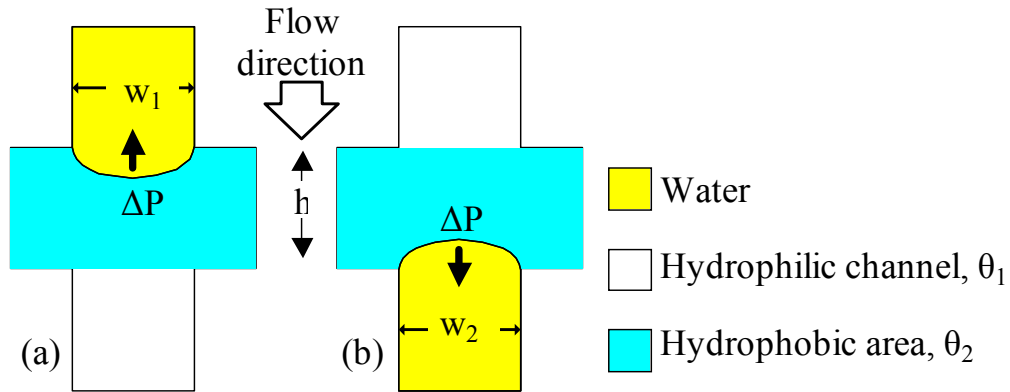


Figure 33: Pressure barriers built across the junction prevent water from (a) entering and (b) staying in the hydrophobic area

the junction (as indicated in Figure 33 is derived by the virtual work principles and can be simplified and approximated as:

$$\Delta P = 2 \frac{\gamma}{w} \sin \theta_1 \quad (9)$$

where γ is the surface energy of gas/liquid interface, w is the width of the microfluidic channel, and θ is the contact angle of the channel surface. In Figure 33(a), the pressure barrier is the required minimum external pressure to push the working liquid into the hydrophobic region. In Figure 33(b), the pressure barrier assists the separation of the flow by pushing the working liquid away from the hydrophobic region into the hydrophilic microchannel.

The most critical step in the splitting sequence is the final breakaway process in Figure 31(e). The pressure barriers built across the junction don't necessarily provide enough forces to break the flow. To have better understanding and to identify critical parameters related to the splitting of flow, a simulation program, Surface Evolver, is employed. First, an initial shape is applied and that defines the constraints that surfaces should satisfy. Energy functions associated with three-dimensional surfaces are specified afterwards. Surface Evolver then discretizes the surfaces into small triangular elements and modifies these elements, subject to the given constraints, to minimize the overall surface energy. Considering an individual triangular element, as shown in Figure 34, its surface energy can be expressed as:

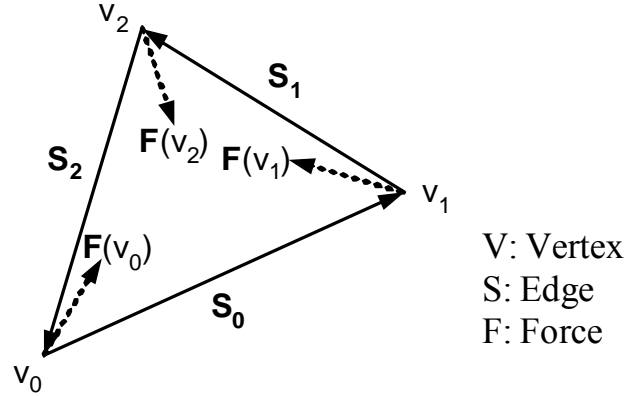


Figure 34: Schematic diagram of the basic element used in the simulation program for surface energy minimization

$$E = \frac{T}{2} \|\bar{s}_0 \times \bar{s}_1\| \quad (10)$$

where T is the surface energy per unit area and two edge vectors of the element. Since the derivative of strain energy with respect to displacement equals the corresponding force, the surface tension force induced at one specific vertex can be expressed as:

$$\bar{F}(v_0) = \frac{T}{2} \frac{\bar{s}_1 \times (\bar{s}_0 \times \bar{s}_1)}{\|\bar{s}_0 \times \bar{s}_1\|} \quad (11)$$

By moving each vertex along the net force induced at it, the overall surface energy will eventually reach its minimum and the equilibrium state can be found. In the current case, the overall energy is the sum of surface energy corresponding to its free surfaces and its contact energy with the channel walls. Figure 35 shows an evolving sequence that predicts a successful breakaway in the microfluidic channel. In this case, the junction length (h) is long enough to cause the surface to become unstable and breakaway will naturally occur to minimize the overall surface energy. The depth (d) and widths (w) of the hydrophilic microfluidic channel and the length (h) of the hydrophobic junction are identified as the critical parameters and numerical simulations are performed to characterize the criteria of natural breakaway. Figure 36 shows the simulation results, which will be employed as design guidelines, with filled areas (including data from the prototype design parameters) indicating breakaway will naturally occur. PDMS is used to fabricate the device for the prototype demonstration and the fabrication process is shown in Figure 37. A patterned SU-8 layer of 20 μm in thickness on top of a silicon

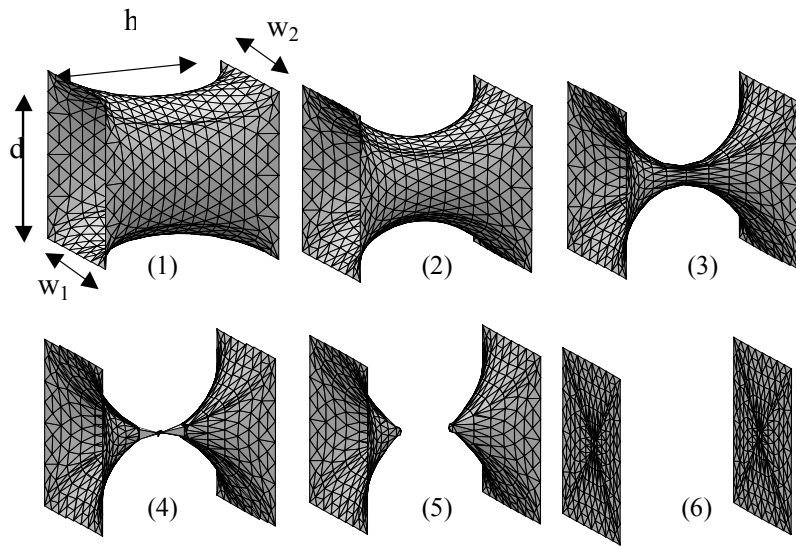


Figure 35: A successful breakaway sequence simulated by Surface Evolver

wafer is employed as a mold to duplicate microfluidic channel in the following casting process. First, a mixture of 10:1 PDMS prepolymer and curing agent (Dow-Corning Sylgard 184) is poured into the mold and cured for 2 hours at 85 °C. Once PDMS is fully cured, it is peeled off from the mold. The major challenge in fabricating the flow

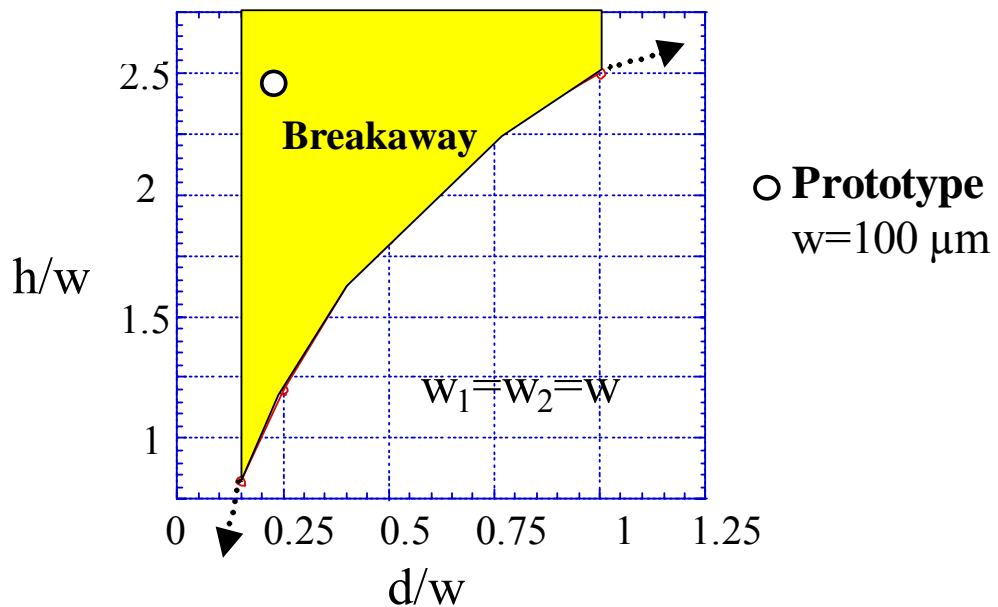


Figure 36: Simulation results of Surface Evolver
Breakaway will naturally occur in the filled areas.

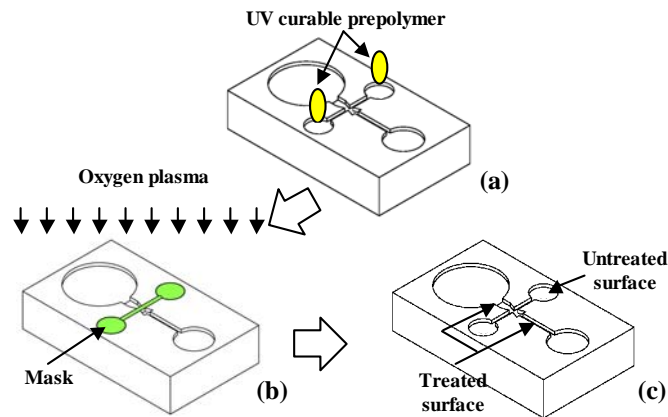


Figure 37: Fabrication process (a) Selectively casting of liquid pre-polymer (b) Oxygen plasma surface treatment and (c) Final result

discretizer is the patterning of hydrophobic and hydrophilic regions inside the PDMS microfluidic channel. Because of the depth and 3-dimensional characteristics of microfluidic channel, conventional 2-dimensional masking processes are inappropriate for patterning the walls of channel. Based on the knowledge that natively hydrophobic PDMS surface can be converted to hydrophilic using oxygen plasma treatment, a new self-aligned mask process is developed and UV curable adhesives are chosen as the masking materials. First, UV curable prepolymer (Norland Optical Adhesive 83H) is poured into the air chambers to fill up the designate hydrophobic region and the flow of prepolymer is stopped automatically by the geometry design of the mask “stoppers” as indicated in Figure 37. Afterwards, the prepolymer is cured and Figure 38 shows the SEM micrograph of the mask that is selectively covering the Microfluidic channel. The

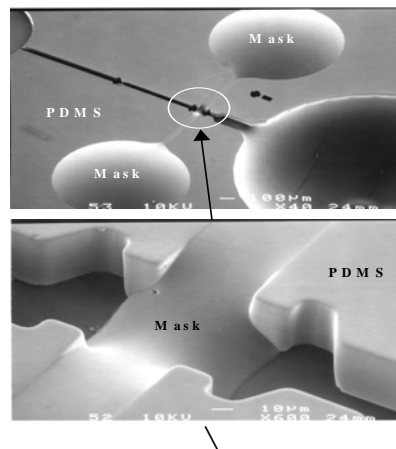


Figure 38: SEM micrographs of microchannel partially filled and covered by self-aligned mask and a close view near the junction

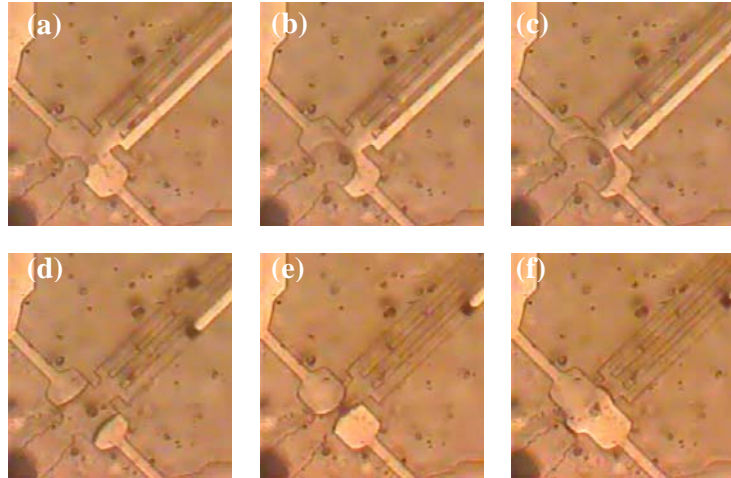


Figure 39: A complete flow discretization sequence

(a)-(b) Liquid is propelled into the hydrophobic area (c) Liquid front reaches hydrophilic area (d)-(e) Liquid is attracted and expelled into the hydrophilic area (f) Flow is split.

solidified 3-dimensional mask is used to protect the designated areas during the following surface treatment process and keep these surface areas staying in hydrophobic after the treatment. Oxygen plasma surface treatment is then applied to modify the surface as shown in Figure 37(b). After the treatment, desired hydrophobic/hydrophilic pattern is generated and the mask is forcefully peeled off from the channel. A glass or PDMS cover is added to complete the fabrication.

The dimensions of the microfluidic channel are specified following the rules acquired from the simulation results to ensure successful breakaway. Figure 39 is the sequence of a flow separation in experiment. Figure 40 shows the measured segment sizes of 10 to 40 nanoliters controlled by the channel geometry and the accumulation step lasts roughly 10

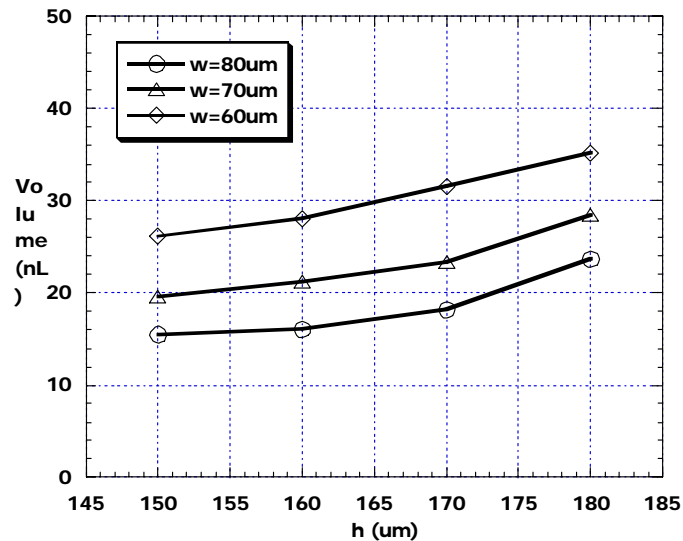


Figure 40: Measured segment volume with respect to geometry of the flow discretizer

minutes. The breakaway process takes less than 10 seconds to complete and is controlled by the incoming flow rate. The volume of discretized segment is determined by the dimension of channel, especially the width (w) of the channel and the length (h) of the junction as indicated in the previous simulation. The depth will also affect the results but currently all the experiments used microfluidic channels with a fixed depth of $20\ \mu\text{m}$. Because of the low elastic modulus of PDMS, volume variation caused by channel deformation is observed. Fluidic delivery and contamination caused by diffusion is a major concern when designing microfluidic channel. The diffusion rate through the delivery channel can be simplified as follows:

$$Q = DA \frac{\Delta C}{L} \quad (12)$$

where D is the diffusivity through the liquid in the channel, A is the cross-sectional area of the channel, ΔC is the concentration difference across the channel, and L is the length of the channel. Generally, the channel needs to have small cross section and significant length to reduce the diffusion rate into and out of the delivery channel. When employ a flow discretizer to provide pulsatile delivery profile, air in the junction area serves as an excellent diffusion barrier because it blocks the diffusion pathway in most time and the only period diffusion occurs is during the breakaway period that is in the range of seconds based on experimental observations. Consider a case of leuprolide acetate diffusing through water with $D = 2 \times 10^{-10}\ \text{m}^2/\text{s}$, $A = 30 \times 100\ \mu\text{m}^2$, $\Delta C = 0.4\ \text{mg}/\mu\text{l}$, and $L = 100\ \mu\text{m}$. The diffusion rate is $2.4 \times 10^{-6}\ \text{mg}/\text{s}$ and the total diffusion mass in 10 seconds is $2.4 \times 10^{-5}\ \text{mg}$, which is only about 0.15% of one digitized fluid segment as observed in experiments. For practical applications, this flow discretizer can be integrated with the previously demonstrated water-powered delivery system as shown in Figure 41 to provide either site-specific intermittent or pulsatile releases of drugs.

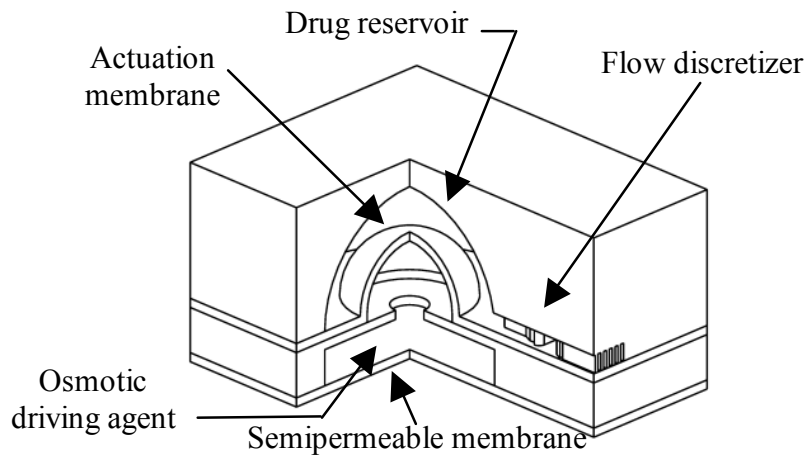


Figure 41: A schematic diagram of the integrated drug delivery system

4.2 Ultra Low-Leakage, Low-Power Gate Valve

The successful function of the BioFlips system requires that the flow of the working fluid be controlled with the utmost level of precision. Developing and implementing ultra low-leakage valves will allow the FATOP to accurately regulate flow within the micro-fluidic channels.

4.2.1 Design of “Hole-in-the-Wall” Ultra Low-Leakage Valve

Micro fluidics now includes a large collection of flow control devices, including valves. Examples of gas and liquid, passive and active, organic and inorganic valves have successfully demonstrated the control of fluid on the micro scale. From the classic to more current designs, the deformation of a membrane to obstruct out-of-plane flow remains a fail-safe means of control. Valves of this type seal very well and exhibit, overall, high performance. Yet, every valve must be designed as a component in a micro fluidic system, and integrating out-of-plane valves with other micro fluidic components may prove difficult. The limitations in the process used to create the valve and the increase in the complexity of the system design to accommodate out-of-plane flow will have an impact on whether a valve becomes broadly adopted. Work has shown that micro fluidic design can be greatly simplified by adhering to a planar design paradigm. Designs of this fashion locate all of the fluidic channels and actuation means within a single wafer. The processes used allow for the simultaneous construction and integration of mixers, pumps and valves. Unfortunately, the simplicity of planar design often hurts the performance of micro fluidic valves. The ratio of closed-to-open fluidic resistance for planar valves can be orders of magnitude less than that of a comparable out-of-plane valve. This is because moving structures in planar designs (gates, flaps, etc.) are often created by the removal of a sacrificial layer to release the structure from the substrate. This opens up a leakage path below or above the moving part that remains even when the valve is closed. Leakage above or below sealing surfaces has often been blamed for causing a large reduction in valve performance for otherwise attractive designs. The valve shown in Figure 42 was built with our new “hole-in-the-wall” process. This

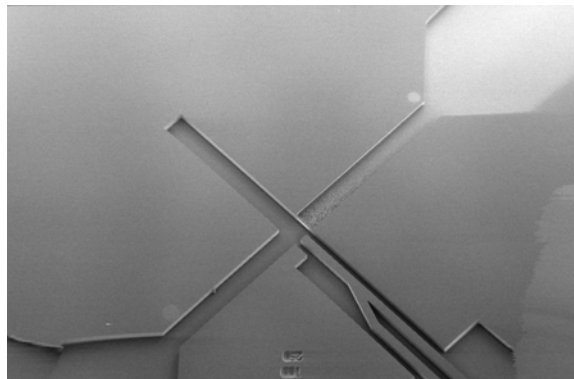


Figure 42: To close the valve, the sliding gate is positioned across the inlet channel using a probe tip

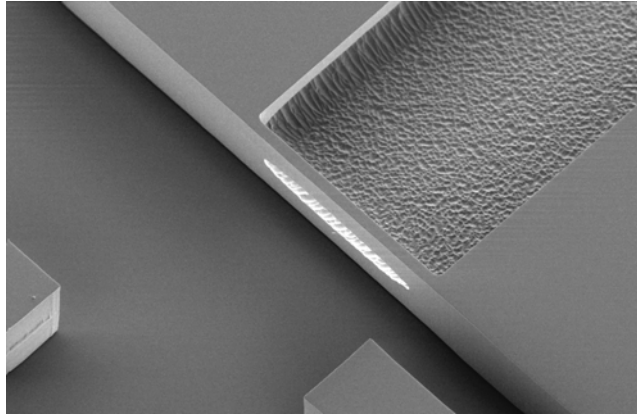


Figure 43: Superior sealing is developed by the “hole-in-the-wall” valve seat due to the removal of the leakage path above and below the gate

fabrication process adds a degree of freedom to planar silicon micro fluidic design. It combines certain aspects from the SCREAM process with a Dual-Depth Berkeley DRIE to create an orifice in the center of the wall of the channel etched in an SOI wafer. This geometry makes an ideal valve seat because gaps above and below moving structures no longer play a significant role in the sealing of the valve, as shown in Figure 43.

The valve shown in Figure 42 was built with our new “hole-in-the-wall” process. This fabrication process adds a degree of freedom to planar silicon micro fluidic design. It combines certain aspects from the SCREAM process with a Dual-Depth Berkeley DRIE to create an orifice in the center of the wall of the channel etched in an silicon on simulator (SOI) wafer. This geometry makes an ideal valve seat because gaps above and below moving structures no longer play a significant role in the sealing of the valve, as shown in Figure 43.

A dual-depth etch step was performed using the Bosch process and an LPCVD silicon oxide mask. See Figure 44, Step 1. The deeper channels reach all the way to the buried oxide layer. The shallow channels were etched only one half the thickness of the device layer (Step 2). The entire wafer was then briefly exposed to an SF_6 plasma (Step 3). This isotropic silicon etch performed two functions: it pushed the silicon wall underneath the passivating oxide layer, for reasons explained later, and it removed some of the scalloped-wall artifacts left by the Bosch process.

The wafer was then thermally oxidized to grow a passivation layer on the exposed silicon of the channels (Step 4). This growth functioned as an oxide polish of the channel walls also. A directed CF_4/CHF_3 plasma was then used to remove the oxide from the bottom of the channels while oxide on the walls remained intact (Step 5). (The oxide protecting the upper edge of the channel wall is often over-etched in this step, becoming too thin to protect the silicon during subsequent etching steps. The etch in Step 3 pushed the channel wall further under the protective oxide layer, mitigating the effects of the over-etch). The wafer was then returned to an isotropic SF_6 plasma to undercut the passivating oxide, puncturing the thin silicon wall separating the inlet and the outlet

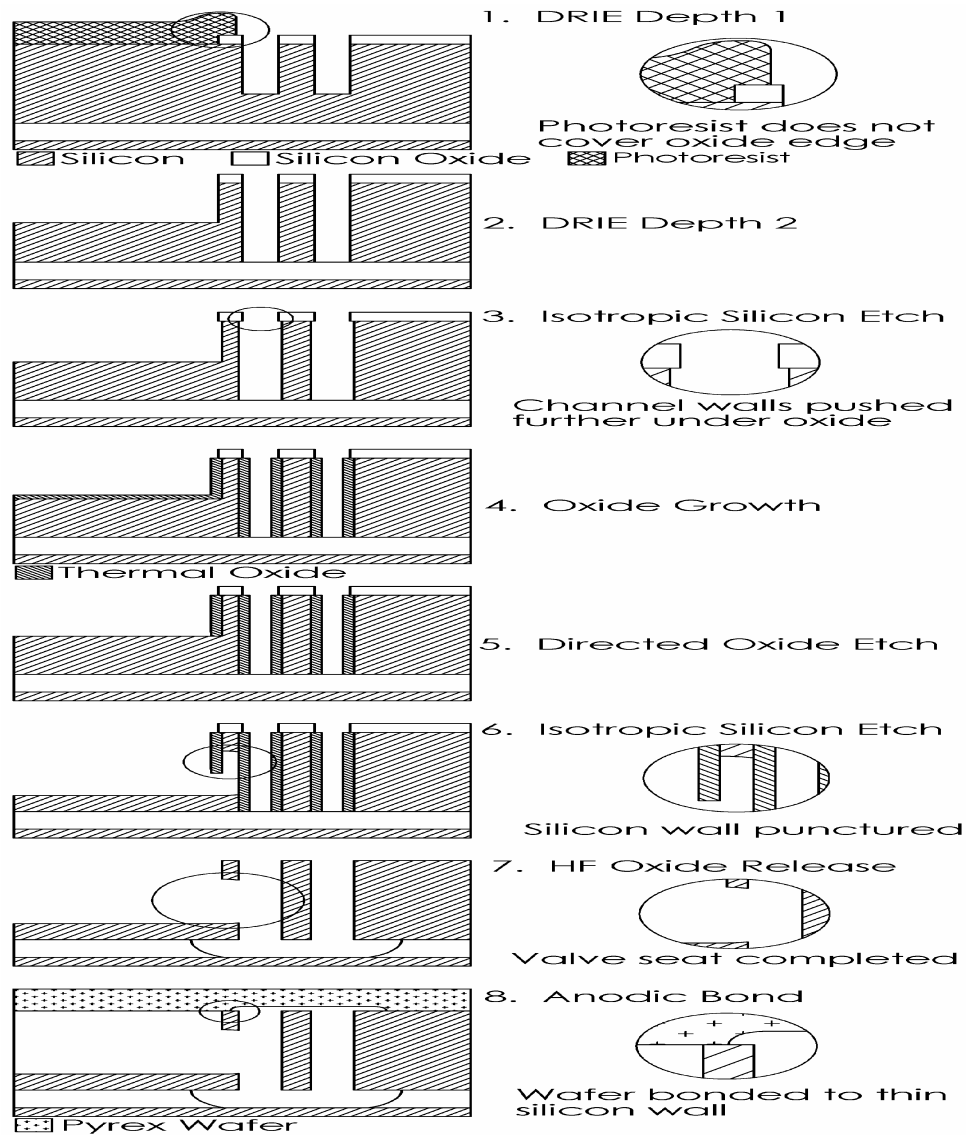


Figure 44: The “hole-in-the-wall” process combines features of both the SCREAM and Dual-depth DRIE processes

channels (Step 6). This step formed the self-aligned valve seat for the valve. The oxide was then removed in an HF etch that also released the sliding gate for the valve design (Step 7). Each gate was still secured with silicon tethers to the device layer. Finally, the appropriate reliefs were etched in a Pyrex wafer and this wafer was anodically bonded to the device wafer (Step 8).

4.2.2 Characterizations of Low-Leakage Valve

Figure 45 shows a simple model on the low-leakage valve to gain insight into the ratio of closed-to-open fluidic resistance of these valves. Assuming only 2 dimensional

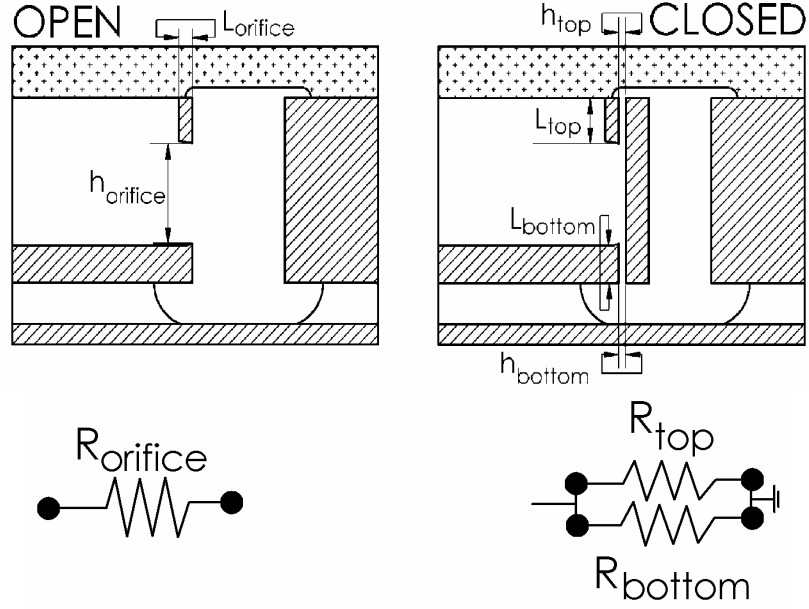


Figure 45: The open and closed configurations of the valve can be modeled by equivalent fluidic resistor circuits

flow, a simple fluidic resistor circuit can be constructed for both the open and closed states of the valve. We know

$$R_{fluidic} = \frac{12\mu L}{wh^3} \quad (13)$$

and for the specific circuits we are using, the dominant fluidic resistance for the open valve is

$$R_{open} = R_{orifice} = \frac{12\mu L_{orifice}}{wh^3_{orifice}} \quad (14)$$

and the dominant resistance for the closed valve is

$$R_{closed} = \frac{R_{top}R_{bottom}}{R_{top} + R_{bottom}} \quad (15)$$

where

$$R_{top} = \frac{12\mu L_{top}}{wh^3_{top}} \quad (16)$$

and

$$R_{bottom} = \frac{12\mu L_{bottom}}{wh^3_{bottom}} \quad (17)$$

All flow resistances are affected by the device layer thickness, d . In terms of the seat geometry, we can write:

$$d = L_{top} + L_{bottom} + h_{orifice} \quad (18)$$

and from inspection of fabricated structures, it is reasonable to assume that:

$$L_{top} = L_{bottom} \quad (19)$$

and

$$h_{top} = h_{bottom} \quad (20)$$

The non-dimensional term, is defined as:

$$\alpha = \frac{h_{orifice}}{d} \quad (21)$$

and

$$L_{top} = \frac{1}{2}d(1-\alpha) \quad (22)$$

Combining these,

$$\frac{R_{closed}}{R_{orifice}} = \frac{1/4 d^4 (1-\alpha)\alpha^3}{L_{orifice} h_{top}^3} \quad (23)$$

where $L_{orifice}$ is the separation between the inlet and valve seat as defined by the oxide mask and h_{top} is the equivalent gap between the gate and the seat. While it is difficult to determine the exact value of h_{top} , this model does suggest that there is an optimal valve seat geometry. Equation (17) is maximized for $\mu = 0.75$. Upon inspection, the valves tested had $\mu = 0.3$, indicating that the ratio of closed to open fluidic resistance may be increased by as much as a factor of five.

Each individual valve was characterized in a simple test setup using DI water, a syringe pump and a +/-15 psi pressure transducer connected by 1/16" ID FEP tubing. See Figure 46. Both the syringe pump and pressure transducer were controlled and calibrated with a LabVIEW interface. Fluidic connections were made to the backside of each valve using 1 cm lengths of flexible tubing. Each valve was glued Pyrex-side up to the bottom of a microscope slide using cyanoacrylate adhesive. This was to allow for visual inspection of the valve during testing. Valves metering the flow of different channel widths were created in the device layer of an SOI wafer. These valves were solely designed to investigate valve seat performance and had no means of micro actuation. The gate of each valve was positioned using a probe tip. (See Figs. 47 & 48). Access to

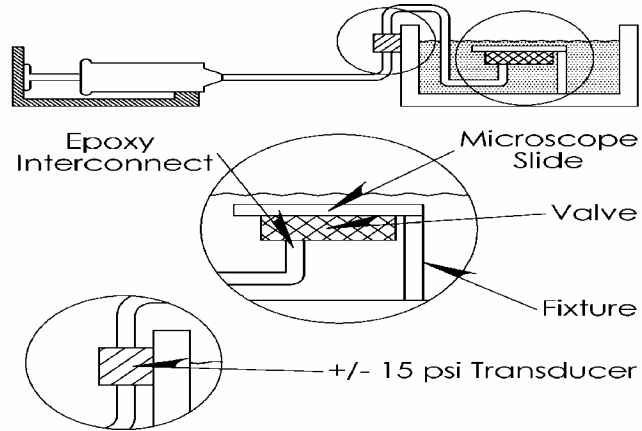


Figure 46: Our test apparatus was designed to reduce dead volume and fluidic capacitance

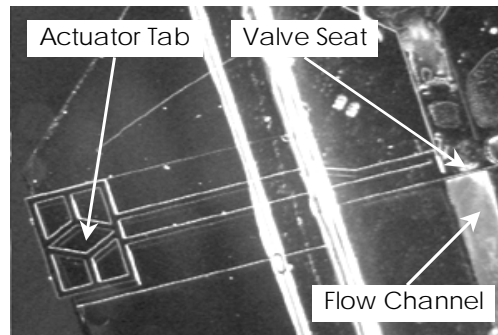


Figure 47: Valve open

The flow channel at right is unblocked by the gate.

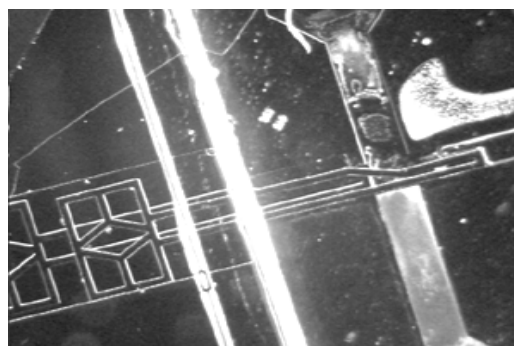


Figure 48: Valve closed

The flow channel is now blocked by the gate wedged across the seat. The ghost image of the gate is due to raised silicon that was not consumed during the wall oxidation. The gate had not been released by this step and the silicon below the gate was not oxidized.

Table 1. Results for Valves with 250 μm and 500 μm Wide Channels.

			250 μm	500 μm
Open	Fluidic	Resistance	4.58×10^{11} +/-	1.54×10^{11} +/-5%
			5%	
Closed	Fluidic	Resistance	$>1.24 \times 10^{16}$	$>1.24 \times 10^{16}$
Closed: Open Resistance Ratio			$>27,000$	$>80,000$

the valve gate was accomplished by selectively cracking off a piece of the bonded Pyrex cover wafer similar to a method used by Zimmermann, *et al.* The valve was connected to the system and submerged under water to remove any fluctuations in pressure due to dripping at the exhaust. We took data for both the open and closed states during the same test run. This minimized the introduction of error between the two measurements due to slight modifications in the system between tests. This open and close process was repeated up to four times per valve. The valve performance did not deteriorate over several manual actuations. The results for valves with two different channel widths are reported in Table 1. Determining the open fluidic resistance for our valves was straightforward: four or five different flow rates were set for the system and the resulting pressure drop across the valve was measured. The linear regression for the pressure drop as a function of flow rate yielded the fluidic resistance and uncertainty. The closed leakage rate could not be determined using the current test setup. The pressure sensors were not rated high enough to measure the pressure drop across the valve at the lowest usable flow rate set by the syringe pump. Additionally, the pressure decay rates for the system when the syringe pump was turned off were close to the decay rates of the system when the line was purposely plugged. This indicates that the leakage rates through the valve approach the intrinsic leakage of our apparatus. Thus, we are only able to measure fluidic resistances less than 1.24×10^{16} Nsec/m⁵.

We have created a gate valve that demonstrates the effectiveness of the “hole-in-the-wall” valve seat and when the gate valve is pushed to the closed position with a probe tip. Figure 49 shows the experimental plot of pressure drop vs. flow rate when the gate valve was open and close, respectively. Results show that the fluidic resistance of the valve increases over 255 times that of the open state. This marks a huge improvement over previous planar gate and check valves that have fluidic-resistance ratios of only 5:1 and 100:1, respectively. With the capability of this low-leakage valve, we worked toward the demonstration of a working "pump+valve" system in the next stage of the project.

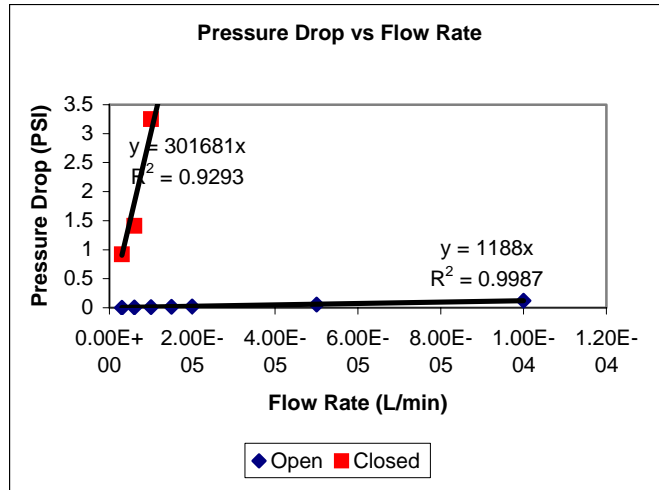


Figure 49: When the valve is closed, the fluidic resistance increases 255 times the fluidic resistance of the valve in the open position

This is 50X better than existing planar gate valve designs.

4.2.3 Ultra-Low-Leakage and Ultra-Low-Power Valve in a Microsystem

We have also conducted system integration in this sub-task by combining the low-leakage valve with micro pumps. The planar micropump, as shown in Figure 50, consists of flow channels and

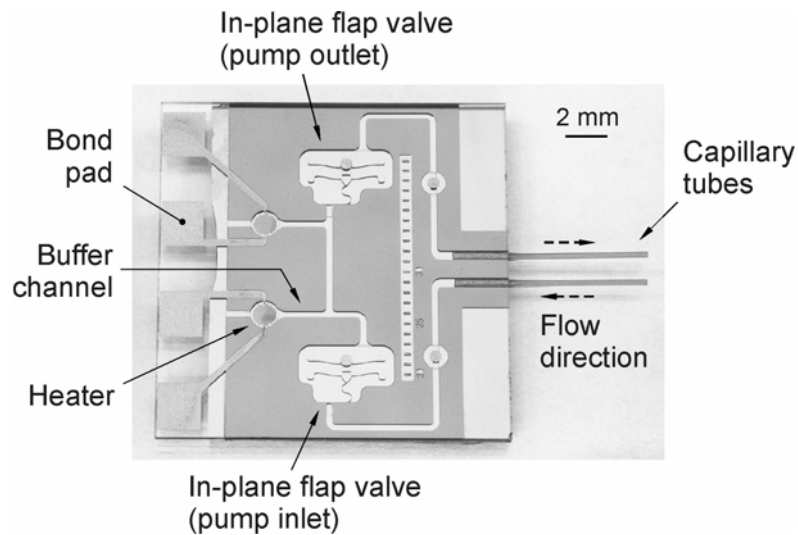


Figure 50: Photograph (top view through the Pyrex[®] cover onto the silicon substrate) of the planar micropump

There are two platinum heaters (including one "backup" heater, 2.3 kΩ resistance) for thermopneumatic actuation and two in-plane flap valves.

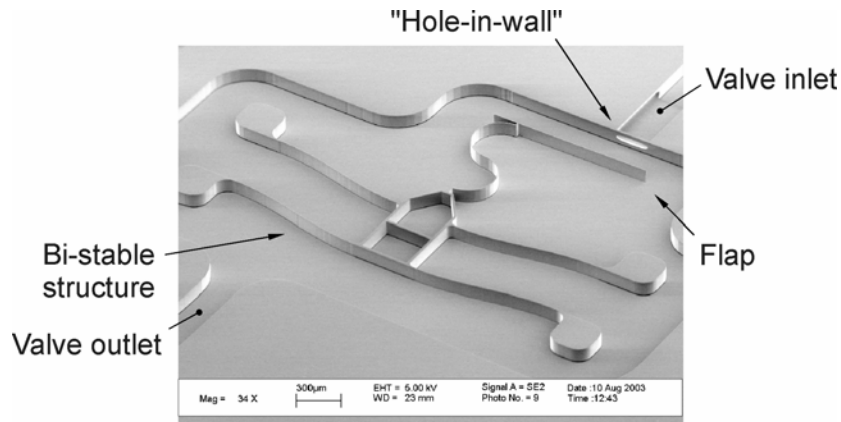


Figure 51: SEM micrograph of the in-plane flap valve

Before flipping the bi-stable structure into the normally closed position.

two in-plane flap valves structured into a silicon-on-insulator wafer and an anodically bonded Pyrex[®] cover with two-platinum resistive heaters (2.3 k Ω). Cyclic pulsing of the resistive heaters causes a bubble to expand and collapse in the bubble chamber. Thus, the bubble serves as the piston of the micropump. The bubble chamber is separated from the flow channel by a buffer channel to avoid direct heating of the working fluid. Capillary tubes glued into in-plane fluid ports serve as fluidic interconnects. The in-plane valves consist of a flexible flap that covers a hole etched through the wall of the valve inlet, Figure 51. This geometry has been shown to create well-sealing valve seats. The flap is attached to a bi-stable suspension that is flipped before wafer bonding, applying a preload on the flap and holding the valve in its normally closed position, Figure 51. The mathematics used to design the bi-stable suspension was previously discussed. The bi-stable suspension is also a fabrication necessity since it is not possible to fabricate an in-plane flap valve in its closed position. Doing so would require etching a submicron thin trench to separate the flap from the valve seat while ensuring maximum sealing. The bi-stable suspension compensates for this short fall. It allows the valve to be closed after fabrication by flipping the bi-stable structure. The suspension also serves as an anchor for the flaps, ensuring that none of the moving parts are lost after they have been released.

Fluid flow in the forward direction causes the flap to bend open while the bi-stable structure remains flipped as shown in Figure 52. The preload from the flipped bi-stable structure combined with the restoring moment of the bent flap returns the flap to the seat for stopped or reversed flow conditions. Since fluid drag is not required to close the valve, the transition time from open to close is minimized which improves the efficiency of the pump. Previous planar micropumps utilizing valves with moving parts had poor performance mainly due to the low fluidic-resistance ratios of these valves. To create in-plane flexures or moving parts, a sacrificial layer needs to be removed from

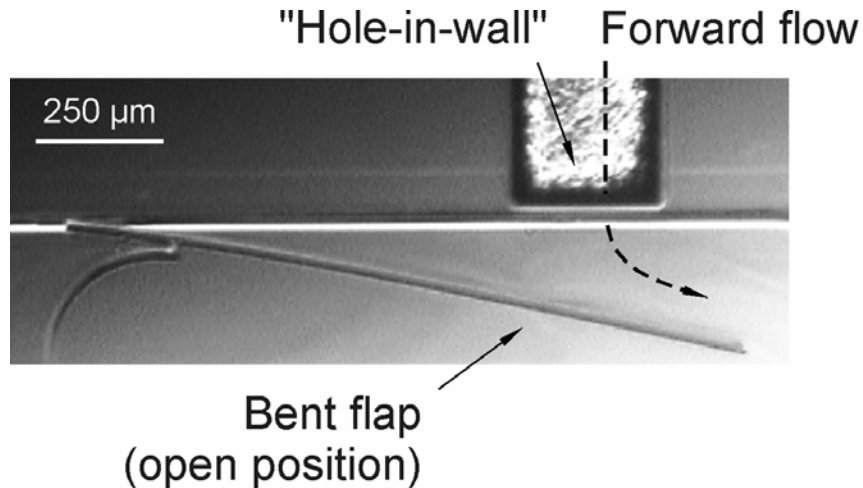


Figure 52: Photograph (top view through the Pyrex[®] cover) of the flap (bent in the open position) during fluid flow through the "hole-in-the-wall"

below the moving part and a recess is required in the cover. This opens up leakage paths below and above the flexure that previous planar valves could not address. The “hole-in-the-wall” design seals off this leakage around the moving flap and greatly enhances performance of the valve and the pump. The pumping process has two steps. Powering the heater causes a bubble to expand in the bubble chamber, forcing fluid through the outlet valve of the pump. During the cooling step the bubble collapses, drawing fluid through the inlet valve. No working fluid is drawn into the bubble chamber since the volume of the fluid displaced by the bubble is less than the volume of the buffer channel.

The pump is wafer-level fabricated with a four-mask process utilizing the “hole-in-the-wall” fabrication method. First, trenches of two different depths are etched (DRIE, vertical sidewalls) in the device layer of an SOI wafer (100 μm thick device layer and 4 μm buried oxide) using a two-layer oxide/photoresist mask. The deeper channels are etched completely down to the buried oxide while the shallow trenches are etched only half way through. The deeper channels make up the majority of the fluidic pathways whereas the shallow trenches are only necessary to create the valve seat. Conformal silicon dioxide is grown in a wet oxidation step to passivate all exposed silicon. The wafer is then subjected to a directed SiO₂ plasma etch to remove the oxide from the bottom of the shallow channels.

An isotropic silicon etch (plasma etch in SF₆ atmosphere) is used to form the valve seat by undercutting the thin silicon wall. This timed etch is halted when the thin wall separating the shallow and deep channels is punctured. Finally, the silicon oxide is removed in HF, which also releases the moving portions of the flap valves. Shallow trenches are etched 20 μm in the Pyrex[®] cover, ensuring that the free-moving parts do not anodically bond to the glass cover. Additionally, the metal meander-shaped heaters, bond pads and connecting traces are patterned in these trenches. Thus, the metal heaters are recessed into the Pyrex[®] so that the two wafers are in close contact for the anodic

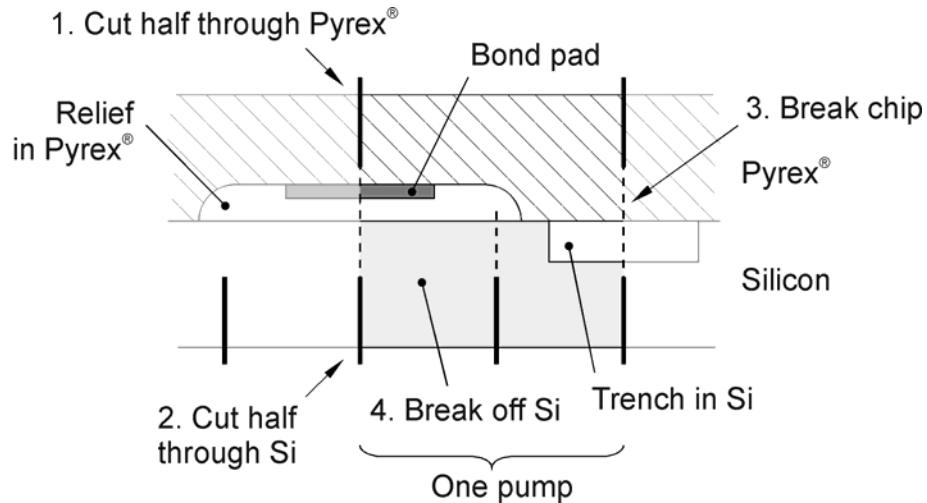


Figure 53: Schematic diagram of the dicing sequence

This sequence prevents particles from contaminating the pump since all channels remain sealed while dicing. Furthermore, it enables bond pad access after wafer-level anodic bonding.

bonding. Due to its inert nature and temperature stability, platinum is used for the heaters. A thin titanium film serves as an adhesion layer between the platinum and the Pyrex®. After anodic bonding, the wafer stack is diced from both sides half way through the silicon and Pyrex® so that the fluidic channels remain sealed while dicing as shown in Figure 53. This prevents particles from entering the pump, which may cause the pump to malfunction. The wafer-stack easily breaks into chips, which opens the in-plane fluid ports. The chip design also allows easy bond pad access after wafer dicing. Since the bond pads are located in shallow trenches in the Pyrex®, the silicon overlapping the bond pads remains unbonded. Thus, the overlapping silicon breaks off readily after dicing the wafer stack, giving access to the bond pads.

4.3 Fore-and-Aft Throttled Osmotic Pump (FATOP)

A portable, continuously monitoring bioassay would alleviate harmful effects of many illnesses. In particular, if the glucose concentration of the patient's blood was maintained within appropriate levels. Such a device would be composed of low-power components operating on wristwatch batteries that deliver 1mA at 1.55V for 180 hours. Therefore, the assay must not only require low power, but also low current and low voltage to avoid further losses to DC-DC voltage conversion. The portable bioassay system must be capable of transporting biological fluids to a sensor. Many pumping mechanisms have been introduced to the MEMS community such as those displayed in Table 2. These devices require either currents or voltages that exceed the limits of the batteries by one to two orders of magnitude. Although the osmotic pump is an exception, it suffers from slow time response and low volumetric-pumping rates.

Table 2. Power Requirements of Micro Pumping Mechanisms.

Pumping Mechanism	Power[mW]	Voltage[V]	Current [mA]
Thermal Bubble	130	20	13
Electroosmosis	0.1	100	0.001
Electrostatics	1-5	200	0.005-0.025
Peristaltic	Power to external compressor and controllers		
Electrowetting	170	2.3	74
Osmotic	0	0	0

4.3.1 A Micro Fluidic Accumulator

On the macroscale, an efficient pumping system has been implemented by water utilities. Drinking water is pumped by the utility at the average daily-consumption rate. When the demand for water is below the pumping rate, excess fluid is accumulated in a system of water towers. When the demand is greater than what the pumps can deliver, the accumulated fluid in the water tower system supplies the excess volumetric flow rate. The creation of the micro fluidic accumulator, MFA, allows for the realization of the micro analog of the macroscale utility system. Bioassays may be performed with a working fluid displaced by a low-power low-voltage pump and stored at an elevated pressure in the MFA. As the length scale decreases, surface-energy phenomena dominate body force phenomena. Exploiting surface-energy effects, it is possible to use reverse-capillary action to store fluid at elevated pressures at small-length scales. The MFA shown in Figure 54 is composed of many hydrophobic micro capillaries. As the pressure of the water in the main channel increases, it will be forced further into the hydrophobic capillaries to be stored at an elevated pressure for later use.

Production of an infinitesimal increase in the surface area while keeping the volume and temperature constant requires an infinitesimal amount of reversible work is

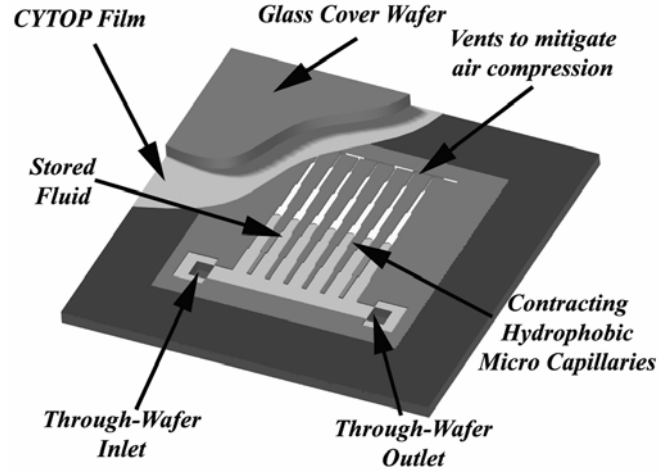


Figure 54: A conceptual drawing of the micro fluidic accumulator (MFA)

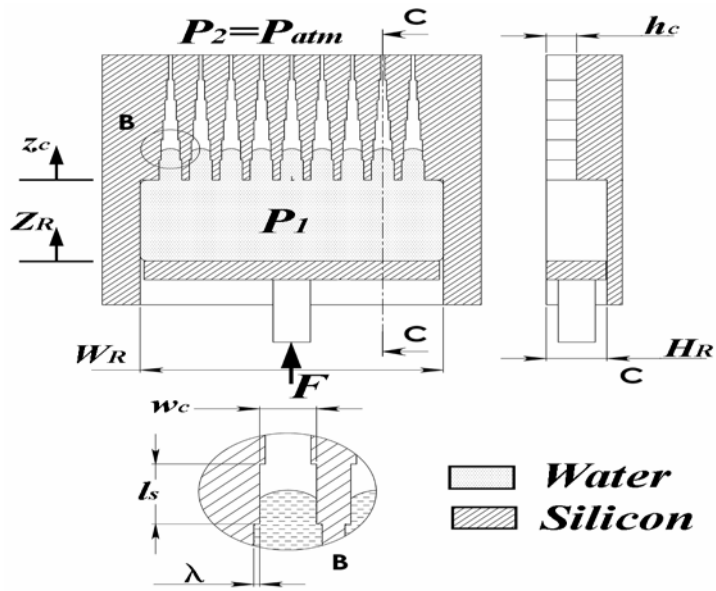


Figure 55: Micro fluidic accumulator schematic

done. For simplicity of modeling, we will consider a smooth, continuous, monotonic contraction of the capillaries. A schematic of the MFA is shown in Figure 55. The following derivation is valid for a continuously contracting capillary width, $w_c(z_c)$.

The fluid in the system is subjected to the continuity relation, $W_R H_R dZ_R = n w_c h_c dz_c$, conserving the volume of water in the system. The total surface energy for the system, U_T , is written in Eq. 24 where A_{la} , A_{sa} , and A_{sl} are the liquid-air, solid-air, and solid-liquid interface areas, and γ_{la} , γ_{sa} , and γ_{sl} are the corresponding surface energies.

$$U_T = \gamma_{la}A_{la} + \gamma_{sa}A_{sa} + \gamma_{sl}A_{sl} \quad (24)$$

Surface tension is a function of temperature. The differential surface energy relationship for an isothermal process is expressed in Eq. 25.

$$dU_T = \gamma_{la}dA_{la} + \gamma_{sa}dA_{sa} + \gamma_{sl}dA_{sl} \quad (25)$$

For the system $-dA_{sa} = dA_{sl}$ and the surface energies are related to the contact angle, θ_c , by Young's equation (Eq. 26).

$$\gamma_{la} \cos \theta_c = \gamma_{sa} - \gamma_{sl} \quad (26)$$

The differential liquid-air interface at the end of the micro capillary is represented by a rectangle. Eqs. 27 and 28 define the differential change in areas for the system. The instantaneous rate of change of the capillary width is $w_c'(z_c)$. The above derivation has also been performed with a contact angle of 180° with $h_c > w_c$. For the design case considered the variance in the differential change in the liquid-air interface is insignificant.

$$dA_{la} = n w_c'(z) h_c dz \quad (27)$$

$$dA_{sa} = 2n w_c h_c \left[\frac{\sqrt{1 + \left(\frac{w_c'}{2}\right)^2}}{w_c} + \frac{1}{h_c} - \frac{1}{W_R} - \frac{1}{H_R} \right] \quad (28)$$

The work done by the external load, F , forces the water into the hydrophobic micro capillaries causing an internal pressure in the system, P_I . The system is vented at the end of the capillaries; the external pressure is atmospheric pressure, $P_2 = P_{atm}$. Eq. 29 defines the infinitesimal amount of work required to create an infinitesimal amount of surface area.

$$\begin{aligned} \partial W &= P_1 W_R H_R dZ_R - P_2 n w_c h_c dz_c \\ &= \Delta P n w_c h_c dz_c \end{aligned} \quad (29)$$

The principle of virtual work requires that the infinitesimal amount of work to create surface area is equal to the increase in surface area. Therefore the pressure in the MFA is derived as Eq. 30.

$$\Delta P = \gamma_{la} \left[\frac{w_c'}{w_c} - 2 \cos \theta_c \left(\frac{\sqrt{1 + \left(\frac{w_c'}{2}\right)^2}}{w_c} + \frac{1}{h_c} - \frac{1}{H_R} - \frac{1}{W_R} \right) \right] \quad (30)$$

One may simplify Eq. 30 to a previously reported relation by Hosokawa *et al.* for a constant width channel. One may also reduce Eq. 30 to the Young-Laplace relation. It is worth noting that the pressure is independent of the number of capillaries that are present in the system. Therefore the area footprint of the MFA is only a function of the quantity of fluid that one would like to store at the elevated pressure. Several clinical chemical and immuno assays can be performed with picoliter to microliter volumes. Main channel dimensions on the order of hundreds of microns would only require hundreds to thousands of Pascals to obtain microliter per minute flows with water. Eq. 30 demonstrates the MFA with capillary width dimensions on the order of ones to hundreds of micrometers may achieve hundreds to hundreds of thousands of Pascals. Furthermore, the MFA is capable of achieving pressures necessary to provide adequate flow for chemical and immuno assays.

The MFA devices were fabricated using the planar wafer-level process displayed in Figure 56. The capillaries and main channel of the MFA are defined by a 100 μm

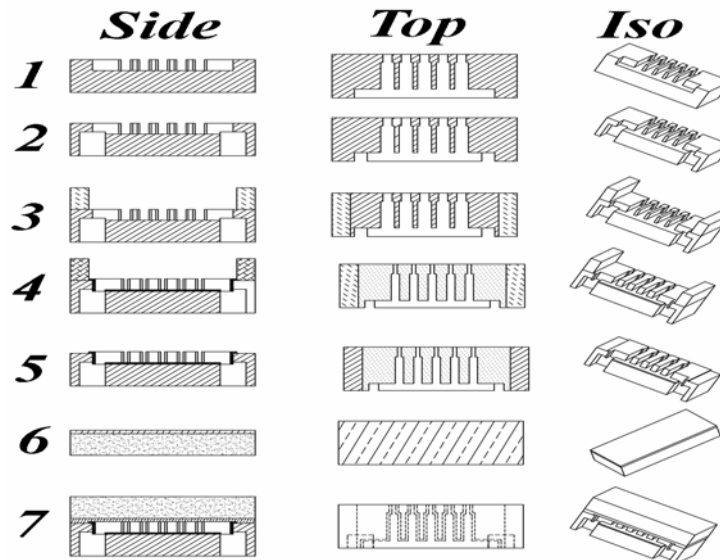


Figure 56: Planar wafer-level Fabrication Process for the MFA

1.) DRIE device features. 2.) DRIE through-wafer fluid ports. 3.) Pre-bond a silicon shadow mask to the device side to define hydrophobic regions. 4.) Plasma-assisted hydrophobic polymer deposition. 5.) Remove screen wafer. 6.) Spin CYTOP™ on Pyrex wafer. 7.) Bond device wafer to Pyrex wafer using Han *et al.* process.

DRIE. The through-wafer fluidic ports are etched into the substrate by backside DRIE. The device wafer is then cleaned in a piranha bath followed by an HF dip to remove the native oxide. A silicon-to-silicon pre-bond is formed with another wafer that has vias in the regions where the Teflon-like plasma-deposited film is desired. The Teflon-like film is deposited via C_4F_8 plasma. Following the deposition the wafers can be easily separated with a razor blade. Using the process defined by Han *et al.*, CYTOP™ is spun on a glass substrate and then bonded to the silicon substrate at 160°C at 5 MPa for

10 min. Following the bond, the wafers are scored with a dicing saw and then broken apart to yield individual MFAs.

4.3.2 Fabrication and Characterization of MFA

The MFAs fabricated have capillaries that are characteristic of the stepped capillaries shown in Figure 55. Mask pattern generators are limited in angular resolution. Finer contracting-capillary angle control may be achieved by contractual stepping of the capillaries. The number of stepped contracting sections was increased from 5 shown in Figure 55 to 20 per capillary. There are 100 micro capillaries for each MFA, allowing the storage of 2 μL . Fabricated MFAs are shown in Figure 57. Fabricated devices had an inlet capillary width, $w_c=35 \mu\text{m}$, a capillary height and reservoir height, $h_c=H_R=100 \mu\text{m}$, a capillary contraction step parameter $\lambda=0.5 \mu\text{m}$, and a section length, $l_s=400 \mu\text{m}$.

Two tests were performed to evaluate the performance of the MFA. The first was to validate the modeling for the static pressure achievable from the MFA, and the second

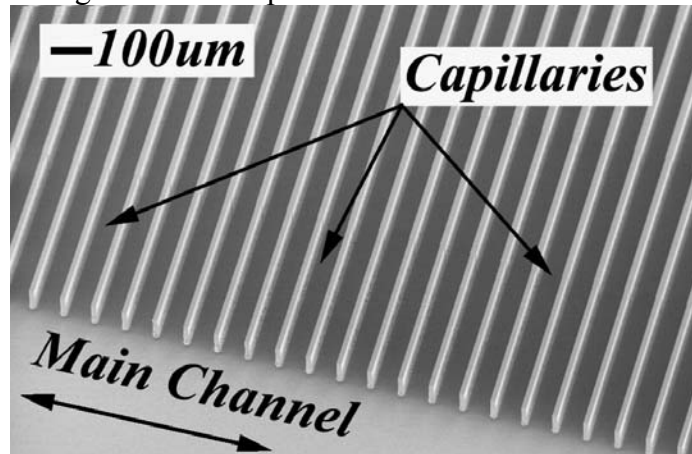


Figure 57: Fabrication results for the planar wafer-level process

was to determine volumetric flow rates delivered by the MFA. A schematic of the testing system is displayed as Figure 58. The first test consisted of purging the system with water, closing the outlet valve, and raising the variable-height water column. Measurements of the pressure were made as the water progressively filled each of the capillary sections. During testing the outlet valve remained closed. The results for the fill test are shown in Figure 59. Theoretical pressures are stepped due to the stepped profile of the micro capillaries for increases of z_c . Uncertainty calculations include variations in temperature, contact angle, sensor bias, sensor resolution, and fabricated dimension variation. The empirical values agree with the theoretical model. All were found to be within 8.4% of theoretical values.

The second test consisted of filling the MFA by using the water column as the fluidic source, then closing the inlet, waiting, and then expelling fluid from the MFA by opening the outlet valve (the inlet valve remains closed). Upon actuation of the outlet valve, the fluid was quickly expelled from the MFA. To capture the release of fluid, an 80 μm wide, 12 mm long, and approximately 100 μm deep micro-machined fluidic resistor was placed on the outlet reservoir side of the outlet valve in series with the MFA.

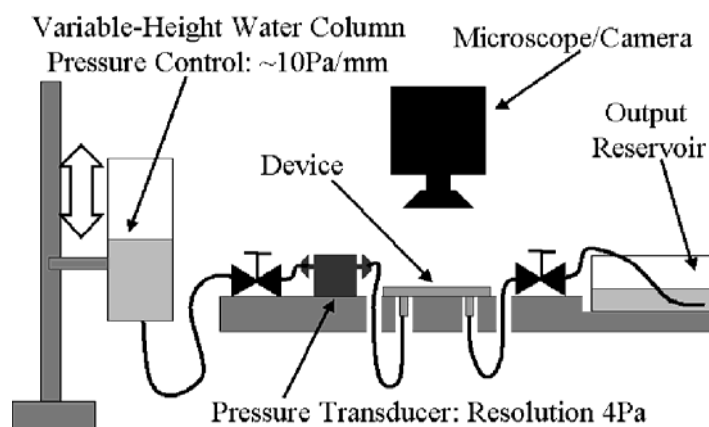


Figure 58: Testing system schematic

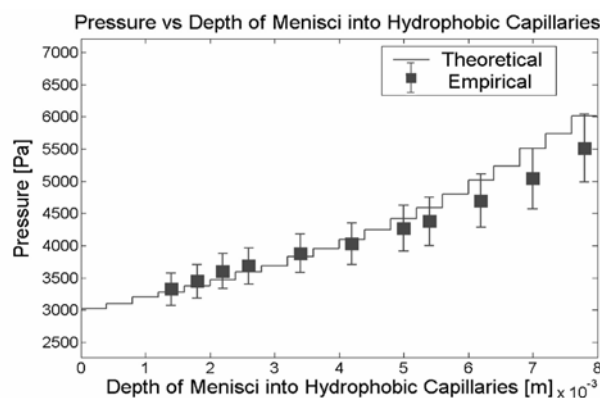


Figure 59: Pressure as a function of z_c for the MFA

The MFA was filled to approximately $\frac{1}{2}$ capacity with $1.2 \mu\text{L}$ of deionized water. The rate of flow was monitored visually by camera. Prior to opening the outlet valve the static pressure was 6060 Pa (0.88 psi). The fluidic resistor allowed for visualization of an average flow rate of $7.2 \pm 0.8 \mu\text{L}/\text{min}$ yielding a total flow of $1.2 \pm 0.1 \mu\text{L}$. The amount of time the water was in the capillaries resulted in a diminished response from the MFA. After 10 filling and dispensing cycles and total storage time of 30 minutes, the flow rate had decreased from $7.2 \mu\text{L}/\text{min}$ to $4.7 \mu\text{L}/\text{min}$. In addition, fluid was being retained in the first section of the hydrophobic capillaries. Further degradation of the hydrophobic layer is noticed after longer periods of time.

The accumulator was also designed to make use of hydrophobic surfaces. This is because capillary forces increase greatly as device size shrinks. The accumulator is composed of many hydrophobic capillaries. The mode of operation of the accumulator is shown in Figure 60. The osmotic pump will force fluid into the main channel. If the valve at the outlet is closed, the pressure of the fluid in the main channel increases. At a characteristic design pressure the fluid is forced into the hydrophobic capillaries and stored at an elevated pressure until the outlet valve is closed.

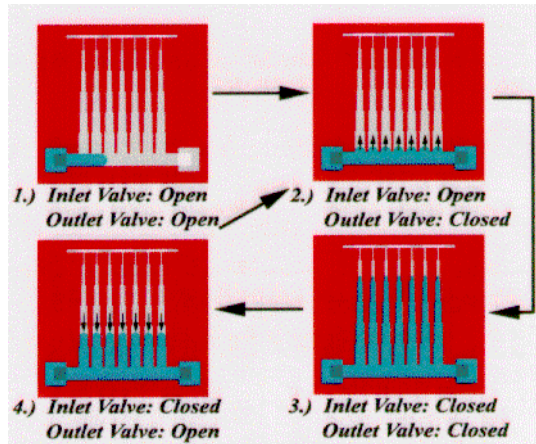


Figure 60: Mode of operation of the micro accumulator

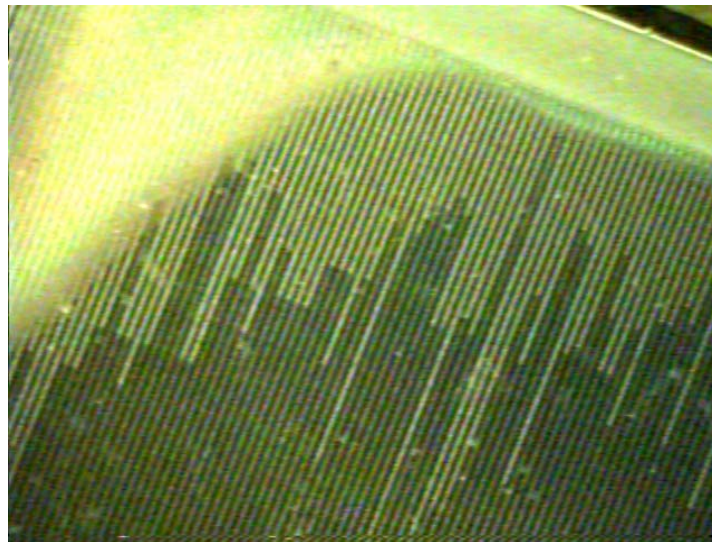


Figure 61: Fluid remains in the microfluidic accumulator after 5-10 filling cycles

It was found that after 5-10 filling cycles residual fluid remained in the microfluidic accumulator, see Figure 61. Hypothesis of the failure mode included a variation of the hydrophobicity of the film, surface roughness concerns, and geometric design issues. The test matrix displayed in Table 3 was performed. Various hydrophobic films are in the first column and various sidewall etching processes are listed in the first row. It was found that by pulsing the C_4F_8 plasma, to mitigate trapped free radical density in the fluorocarbon films, and also implementing a KOH etch, that assured the capillary sidewall was very smooth, the device lifetime could be increased by 3-7 times.

Table 3. Test Matrix for Evaluation of Hydrophobic Surfaces.

	DRIE Etch	KOH	DRIE w/ Sidewall Polish
C ₄ F ₈ Plasma	5 cycles		
SAM OTS	DNE		DNE
Pulsed C ₄ F ₈		~35 cycles	
CYTOP	1-2 cycles		1-2 cycles
Teflon AF			

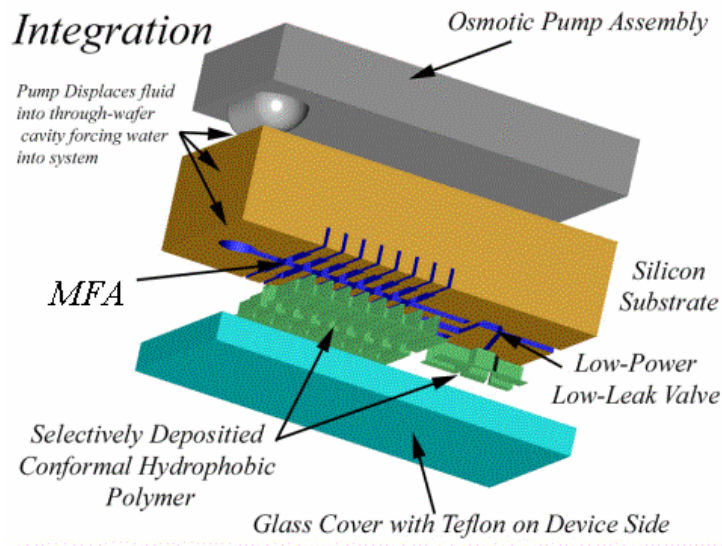


Figure 62: The system integration

Shown are the osmotic pump, low-power-low-leakage valve and the micro accumulator.

The system integration of the osmotic pump, the microvalves, and the accumulator will be integrated as shown in Figure 62. The accumulator and microvalves have been designed in planar wafer-level processes and therefore can be fabricated adjacent to one another on the silicon wafer. The osmotic pump was fabricated using PDMS, and therefore can be attached to the backside using an O₃ discharge.

4.4 Micro Dialysis Needle

The goal of this subtask is to demonstrate a micro dialysis needle for the acquisition of body fluids for the BioFlips system. When microdialysis needles are used to sample interstitial fluid, biosensor stability and lifetime can be extended if metabolites are filtered through a micro dialysis membrane before fluid is moved onto the sensor. Protein adsorption onto a sensor seriously affects the stability and lifetime of a sensor. For this reason, many commercial enzyme based biosensors (e.g. glucose sensors) are single-use systems. Current dialysis needles which are used to increase sensor stability and lifetime have a very large bore, consume a large amount of fluid, and are uncomfortable during insertion and prolonged wear. They also require a serial assembly in which a dialysis membrane is inserted and bound into each needle. In addition, the large needle is inserted directly into the blood stream that causes discomfort for the patient.

4.4.1 Micro Fabricated Dialysis Needle

A micro fabricated dialysis microneedle as shown in Figure 63 has been developed which is permeable to small molecular weight molecules and excludes large

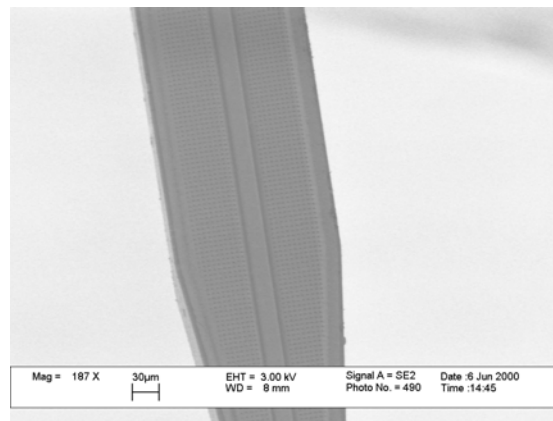


Figure 63: SEM micrograph of a micro dialysis microneedle

molecular weight compounds such as proteins. This microneedle compared to existing technologies, is an order of magnitude smaller in almost all characteristics, while meeting a similar performance criterion. It is also completely fabricated by standard microsystem technologies. Thus, no further assembly is necessary. In addition, the needle can be integrated with planar electrochemical sensors. The fluid channel is only 10 μm high as shown in Figure 64. This dramatic miniaturization results in smaller sample volumes, more rapid diffusion equilibrium of analytes between interstitial fluid and dialysis fluid, and a lower overall power consumption to operate the system. The needle penetrates just below the stratum corneum which is the topmost layer of the skin, and analyte concentrations equilibrate between the interstitial fluid and dialysis fluid. Fortunately the concentration of many analytes in interstitial fluid, including glucose, is strongly correlated with blood concentrations, while the superficial penetration of the needle under the skin minimizes patient discomfort. This microdialysis needle is fabricated as a polysilicon microshell on top of a silicon substrate while the silicon on insulator (SOI) device layer serves as a mechanical support. The diffusion membrane is fabricated using a layered polysilicon sandwich with a thin thermally grown oxide of 10 - 50 nm thickness between the layers, and appropriate etch access holes.

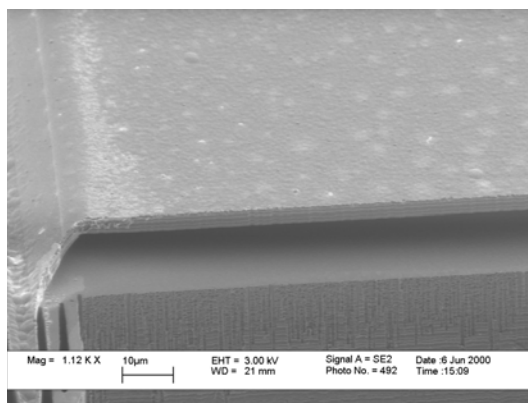


Figure 64: SEM micrograph of the fluid channel of a microneedle

To fabricate the diffusion membrane 10 μm of sacrificial low temperature oxide (LTO) is first deposited at 450 $^{\circ}\text{C}$ onto a 50 μm -thick device layer of a SOI wafer by low pressure chemical vapor deposition. The oxide is annealed afterwards at 900 $^{\circ}\text{C}$ in a nitrogen atmosphere and patterned by a plasma etch process in a CF_4 atmosphere to define the flow passage. Then 2 - 3 μm of the polysilicon is deposited to define the microshell. The polysilicon is annealed in a nitrogen atmosphere at 900 $^{\circ}\text{C}$ to ensure a tensile stress in the film. Afterwards the 2 μm open holes are structured by plasma etching in a Cl_2 atmosphere. The polysilicon is then oxidized in a dry oxygen atmosphere

at 900 °C to grow 10 - 50 nm of thermal oxide that defines the diffusion passage. A layer of 200 nm of polysilicon is then deposited and annealed as before and structured to define adhesion anchors by etching the thin oxide in hydrofluoric acid. A 500 nm polysilicon layer is deposited, annealed and structured to intersect with the thinly grown oxide. The needle shape is then patterned and the needle is etched down to the buried oxide of the SOI wafer in a surface technologies systems (STS) deep reactive ion etcher. Finally the needles are released in concentrated hydrofluoric acid for several hours until all the sacrificial oxide is removed. This release also opens up the diffusion channel. Since all the polysilicon has been annealed to be tensile, there should be no buckling between layers that could pinch off the channels.

For faster diffusion and easier integration a new dialysis membrane with a simplified fabrication process as shown in Figure 65 and higher porosity such as porous poly-silicon is necessary. Furthermore the mechanical stability of the micro needle has to be improved. A polymer coating might reinforce the brittle silicon needle. To fabricate this micro dialysis needle 10 μm of sacrificial low temperature oxide (LTO) is deposited at 450°C onto a 50μm thick device layer of a SOI wafer by low pressure chemical vapor deposition (LPCVD). The oxide is annealed afterwards at 900 °C in nitrogen atmosphere and patterned by a plasma etch process in CF₄ atmosphere to define the flow channel. Then 2-3 μm of poly-silicon is deposited by LPCVD to form a shell that bounds the channel. The poly-silicon is annealed in nitrogen atmosphere at 900°C to ensure a tensile

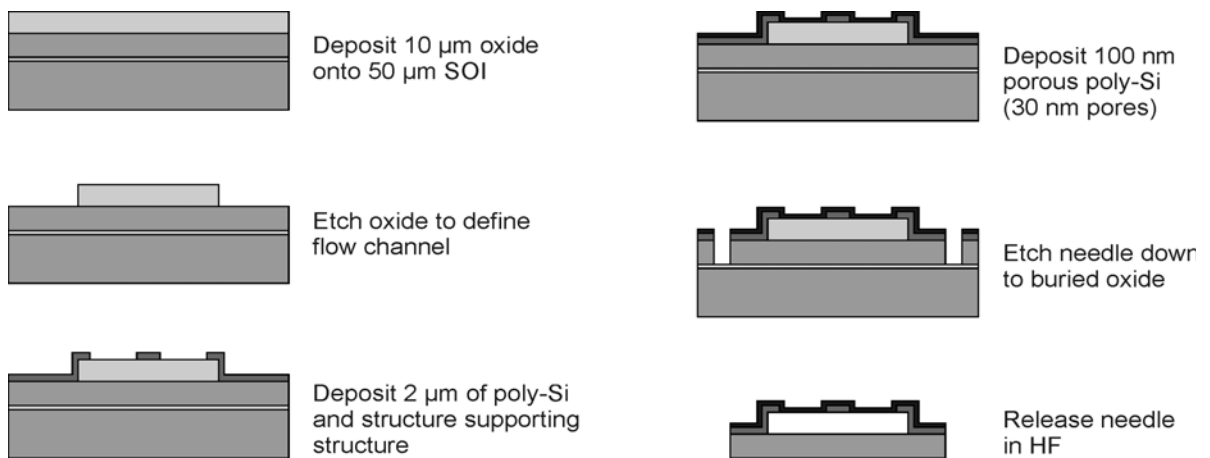


Figure 65: Fabrication process of the improved micro dialysis needle

stress in the film and structured by plasma etching in Cl_2 atmosphere. Afterwards 100 nm of porous poly-silicon is deposited to form the dialysis membrane. The needle shape is then patterned and the needle is etched down to the buried oxide of the SOI wafer by plasma etching in a surface technology system (STS). Finally the sacrificial oxide is removed in concentrated hydrofluoric acid that opens up the diffusion channel.

4.4.2 Theoretical and Numerical Simulation on Micro Dialysis Needles

In order to predict the effectiveness of a microdialysis needle, the mass transfer characteristics have been modeled in relevant medical situations. Since one of the largest applications of electrochemical sensors is for diabetics most of the modeling is done assuming glucose is diffusing into the needle. Therefore, it is assumed that the needle is bathed in interstitial fluid with a constant concentration source of glucose in the physiological range of 5 mM. In order to describe the mass transfer characteristics in the channel Fick's second law for single component diffusion is considered:

$$\frac{\partial C}{\partial t} + \bar{u} \cdot \bar{\nabla} C = D \bar{\nabla}^2 C \quad (31)$$

where C is the concentration and D is the diffusivity of the component of interest. For small molecules such as glucose D is assumed to be 10^{-9} m²/sec. If one-dimensional unsteady diffusion is assumed, then (31) simplifies to (32).

$$\frac{\partial C}{\partial t} = D \frac{\partial^2 C}{\partial y^2} \quad (32)$$

This can be solved by separation of variables with the boundary conditions $C = C_0$ at $y = 0$, $t \neq 0$, a no penetration boundary condition, $\partial C / \partial y = 0$ at $y = 2a$ at the opposite wall of the flow channel for all times, and the initial condition that $C = 0$ everywhere at $t = 0$.

$$C = C_0 \left[1 - \sum_{i=1,3,5,\dots}^{\infty} \frac{4}{i\pi} \sin\left(\frac{i\pi y}{4a}\right) \text{Exp}\left(-\frac{(i\pi)^2 Dt}{16a^2}\right) \right] \quad (33)$$

If diffusion out of the needle into the ambient is considered, then the needle can be modeled as a constant source diffusing into a semi-infinite medium. The diffusion equation can be solved as follows.

$$C = C_0 \left[1 - \text{erf}\left(\frac{y}{\sqrt{4Dt}}\right) \right] \quad (34)$$

is the dialysis membrane. Since the pore sizes are much larger than the molecules of interest, permeability can define where k is a partition coefficient, assumed to be 1, p is the porosity or volume fraction of pores versus total membrane volume, and T is the tortuosity of the membrane because the diffusion distance is larger than the thickness of the membrane. For the diffusion channel membrane described with its 30 nm diffusion channels, 2 μm membrane thickness and 4 μm total diffusion length through the membrane $T = 2$ and $p = 0.016$.

$$P_n = \frac{Dkp}{dT} \quad (35)$$

The time for such a membrane to come to equilibrium is therefore approximated by compartment diffusion where V is the volume of the needle, and A_m is the area of the membrane for diffusion.

$$\frac{V}{A_m P_n} = \frac{2a}{P_n} \quad (36)$$

This expression becomes the height of the flow passage divided by the permeability of the membrane. The Stokes-Einstein relation can approximate the diffusion coefficient for a large component in a pore:

$$D_n = \frac{kT}{6\pi a \mu} \propto M^{-1/3} \quad (37)$$

where M is the molecular weight of the molecule. As the molecular weight of a molecule increases, its diffusion coefficient is smaller causing slower migration. Eq.(36) predicts that in a channel with a height of 10 μm , the microdialysis membrane should come to equilibrium in 2.5 seconds. In addition Eq.(33) predicts that the dialysis solution in the channel will come to equilibrium in 0.3 seconds if a one dimensional diffusion solution is assumed. However, the largest resistance to mass transfer is the dialysis membrane and not free diffusion of small molecules into dialysis fluid.

It should be noted that the above analysis assumes a constant concentration at the flow channel boundary for all times. It does not take into account the mass transfer delay of material diffusing through the membrane, nor the discrete diffusion channels through which material can enter the flow channel. When material enters the flow channel it first diffuses out in the radial direction from the 30 nm wide pores. The spacing between the 30 nm wide diffusion channels is 2 μm . Since the diffusion channel is made from a thin oxide, each pore may be considered to be a line source with a gradient in both the x and y directions. Computational methods must be employed to observe the transient behavior of material diffusing out of such pores in two dimensions and to consider convection from fluid flow in the flow channel. The fluid is assumed to be moving through the needle at 1 nl/s while the concentration of the line sources is still supposed to be constant.

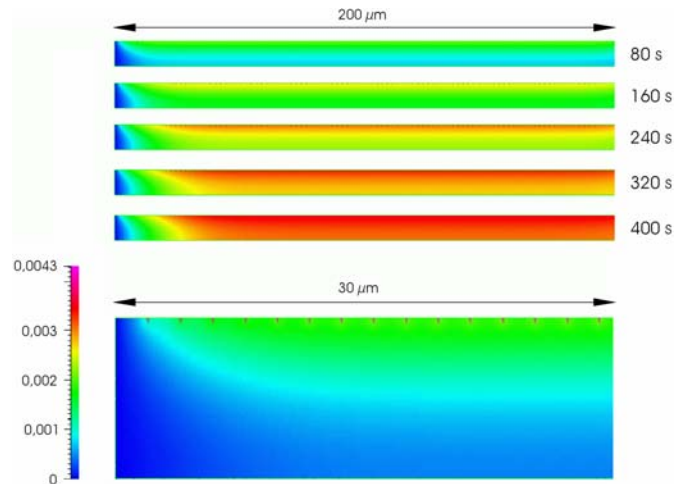


Figure 66: Calculated 2-dimensional diffusion

Top- from the 30 nm sources with parabolic fluid flow at 1 nl/s.
 Bottom- Close up of 30 nm sources at the channel entrance.

The simulation results in Figure 66 shows that already 200 μm down the channel from the entrance region the two-dimensional diffusion problem collapses to one dimension. Since the total length over which diffusion may occur is 2 mm, the former assumption that there is no concentration gradient in flow direction is valid. More important is that the diffusion progresses is much more slow than previously assumed, since there is no longer a constant source boundary condition and the area of the pores is only 1.5 % of the total surface area of the membrane. The discrete sources allow less mass flux into the channel creating a longer transient to equilibrium than is predicted from a constant source boundary condition. The system comes to equilibrium in about 500 seconds based on the simulation result. In order to visualize that the diffusion membrane allows mass transfer across it, fluorescein dye with a molecular weight of 322 has been visualized diffusing from the needle. Therefore the needle was submerged in water to avoid high surface tension due to free surface and dye was infused at a rate of 10 nl/s. As shown in Figure 67, the microdialysis membrane will allow mass to permeate. Large proteins should be

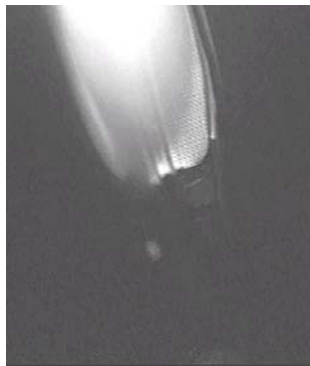


Figure 67: Fluorescent dye in equilibrium with a water droplet on the needle
 The pores can be seen as small dots on the needle surface.

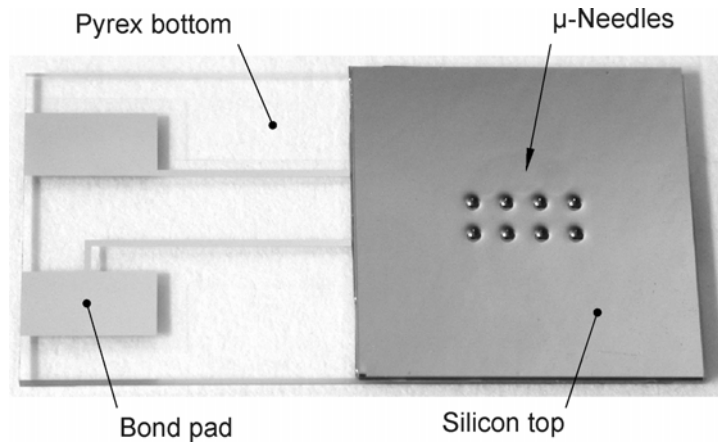


Figure 68: Photograph of the μ -needle-based glucose monitor

The glucose sensor is placed inside a shallow trench underneath an array of 8 μ -needles.

selectively excluded from permeating the microdialysis membrane since they cannot fit inside the small channels. Smaller proteins may be able to permeate the membrane but their motion should be retarded. Even if some protein does permeate the membrane, the concentration in the dialysis fluid should be at a significantly lower concentration than in the bulk which will extend the performance lifetime of a biosensor.

4.4.3 Integrated Microneedle and Bioassay System

The capability to easily and continuously monitor blood glucose levels would be a tremendous improvement in the treatment of diabetes. A painless approach is to measure the glucose level of the interstitial fluid. We demonstrate this for the first time using an integrated μ -needle-based glucose monitor as shown in Figure 68. We also present an in-device immobilization technique that is essential for wafer-level fabrication of enzyme-based BioMEMS. Interstitial fluid from a fingertip has been pulled through μ -needles in Figure 69 by capillary forces into an enzyme-based glucose sensor. The resulting signal

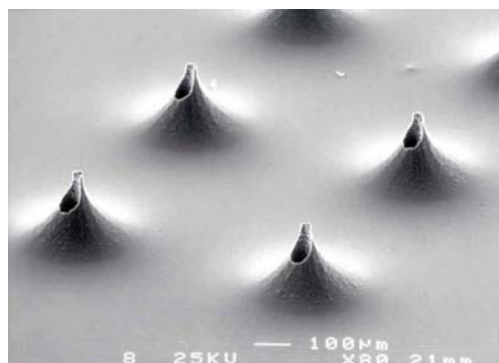


Figure 69: SEM micrograph of 200 μ m long hollow μ -needles with an inner diameter of 40 μ m

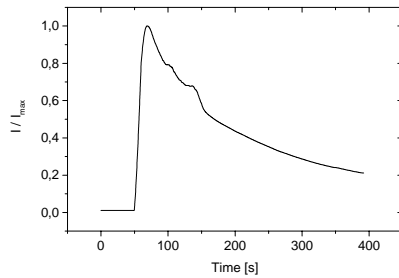


Figure 70: Sensor response of the single use glucose monitor after sampling interstitial fluid

peak in Figure 70 corresponds to the glucose concentration in the fluid. This simple concept can be extended to a more complex system for continuous long-term monitoring where the glucose sensor is placed in a flow channel as shown in Figure 71. An integrated porous polysilicon dialysis membrane separates the interstitial fluid inside the needles from the dialysis fluid inside the flow channel. This prevents diffusion of larger proteins to the sensor improving its long-term stability. Wafer-level fabrication of BioMEMS usually requires high temperature bonding methods such as anodic bonding. Enzymes denature at high temperatures. Thus, enzymes need to be immobilized after wafer bonding. Our novel in-device enzyme immobilization technique allows wafer-level patterning of enzyme inside flow channels. It uses a photosensitive polymer (PVA-SbQ) mixed with buffer containing the enzyme. Each system is filled with this solution after anodic wafer bonding. Auxiliary channels connect all devices and allow filling of the entire wafer by capillary forces through a single inlet in Figure 71. The polymer is

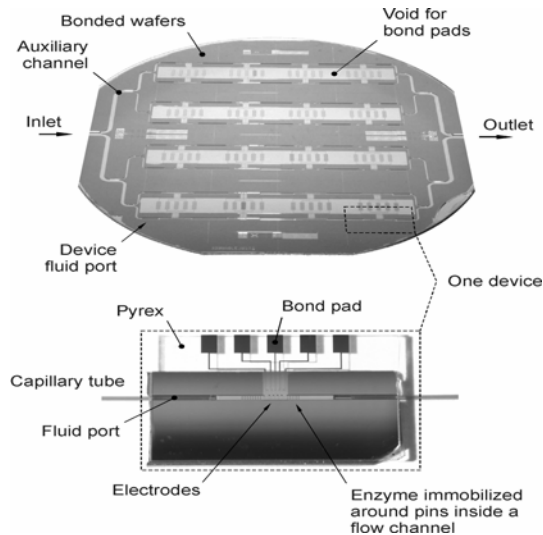


Figure 71: Photograph of a bonded wafer pair showing the inlet and outlet for wafer-level enzyme loading (top) and single chip with an integrated glucose sensor inside the flow channel (bottom)

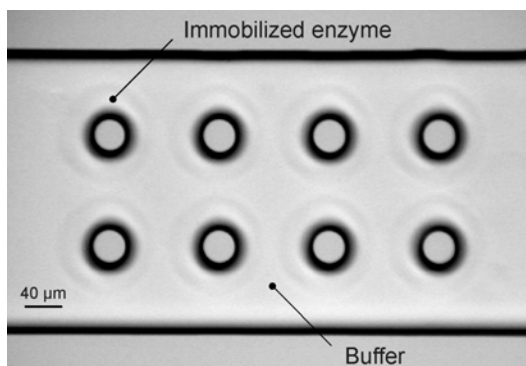


Figure 72: Photograph of 15 μm thick gel sleeves immobilized around silicon pins inside the flow channel

then crosslinked under UV light through the Pyrex cover using a shadow mask so that the enzyme is entrapped in the locally formed gel. The unlinked solution is rinsed out of the chips while the active gel remains inside the flow channel in Figure 72. Our design also allows easy bond pad access after dicing the wafer stack into chips. The overlapping silicon breaks off automatically in Figure 71.

The reaction kinetics and the long-term stability of immobilized glucose oxidase have been investigated in detail. The calibration curve in Figure 73 yields an apparent Michaelis constant of $K_m = 11.2$ mM which is below $K_m = 33$ mM for free enzyme in solution. This indicates rapid diffusion of glucose into the gel as well as enzyme activity similar to free enzyme but also an oxygen-limited response at higher glucose concentrations. The reaction kinetics is diffusion controlled in the range 0 - 120 mg/dl in Figure 73. In order to store such a device the gel can be dehydrated and rehydrated later without significant loss of enzyme activity. Continuous sensor operation at 25 °C causes the signal to drop by only 65 % within 24 hours, which is sufficient for a disposable system. Loss of activity due to enzyme leakage out of the gel can be minimized by crosslinking the enzyme to the PVA-SbQ backbone. No loss of activity for exposure energies up to 18 J/cm² was measured.

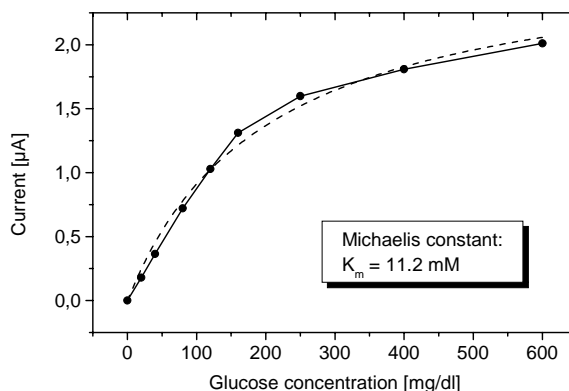


Figure 73: Calibration curve of the glucose monitor

The linear range is 0 - 120 mg/dl. The sensor response time is 45 seconds.

4.5 Complete Water-Powered Bioassay System

The complete system requires integration of various microfluidic components. We have developed several technologies in the areas of device integration (bonding), bioassay and control circuits in this task.

4.5.1 Localized Plastic Bonding for Assembly, Packaging and Liquid Encapsulation

Localized plastic bonding schemes for plastics-to-silicon, plastics-to-glass, and plastics-to-plastics assembly, packaging and liquid encapsulation have been successfully demonstrated. These schemes are important for the integration of various components to be developed in this project as a final bioassay system. Aluminum thin films are deposited and patterned as resistive heaters for the purpose of localized heating and bonding. In the experiments, plastic thin films are successfully bonded on silicon, glass, and plastic substrates in 0.25 seconds under a contact pressure of 0.4 MPa. Local temperature at the bonding interface can reach more than 140°C for bonding and the global substrate remains at room temperature. The approach of localized heating for bonding of plastic materials while maintaining low temperature globally enables direct sealing of polymer based MEMS processing without using additional adhesive and without damaging pre-existing, temperature-sensitive substances on the bonding substrate. Water encapsulation by plastics-to-plastics bonding is performed to demonstrate the capability of low temperature processing. As such, this technique can be applied broadly in plastic assembly, packaging and liquid encapsulation for microsystems, including the water-powered bioassay system in this program.

In recent years, plastic micro devices are becoming increasingly important in microfluidic applications for biosensors and biological assays. Unlike silicon, there is no established batch processing techniques for plastic materials that are subject to different thermal, physical, and chemical constraints. One major problem in the area of plastic MEMS is the bonding of components made of different materials. Most existing bonding techniques in MEMS focus on the bonding of semiconductor, metal and ceramic materials that can sustain high processing temperature but these schemes are not applicable to temperature-sensitive plastic materials. Therefore, a reliable and repeatable bonding process, which does not alter the properties and performance of plastic materials during the bonding process, is required.

During the past few years, efforts have been undertaken to find a reliable bonding process that can be conducted at low temperature for plastic microsystems, and using polymer as an intermediate bonding layer looks promising. Several polymer materials have been reported to be able to serve as the adhesive layer for bonding with silicon substrates [9-11]. However, these thermoset polymers require long curing time (hours) and high curing temperature (150°C) during the bonding processes that may damage plastics and other temperature-sensitive materials. For examples, the bonding process of cell encapsulation must be able to occur in the presence of the biological materials to be transplanted without affecting their functionality [12]. In general, these materials can only survive in temperatures as low as 45°C for a period of about two minutes [13]. In this work, soft thermoplastic materials with low glass transition temperatures are introduced to perform localized plastic bonding. Three types of localized bonding

processes have been investigated: plastics-to-silicon bonding, plastics-to-glass bonding, and plastics-to-plastics bonding. Direct microencapsulation of liquid using localized heating is also demonstrated for the first time.

Bonding processes should operate under two basic conditions. First, the two bonding surfaces must have intimate contact for bonding. Second, proper processing temperatures are required to provide the bonding energy and the lowest possible processing temperature should be employed to reduce the detrimental effect of thermal mismatch and to prevent degradation of plastic materials. The elastic properties of thermoplastics reduce the stress in the bonded materials caused by the bonding process and the force required to keep intimate contact. Localized heating provides the energy for bonding and is achieved by using microheaters instead of global heating furnaces [14,15]. These microheaters are constructed in a way that heating is restricted in a small region that is surrounded by insulation materials. The effectiveness of localized heating depends on the selection of materials and the design of the geometrical shape of the overall structure. Two bonding schemes are demonstrated as shown in Figure 74: (a) bonding by built-in type heaters and (b) bonding by reusable type heaters. For silicon substrates, a silicon dioxide layer of 1 μm thick is grown for electrical and thermal insulation before heaters are fabricated. If glass substrates are used, no oxide insulator layer is required. An aluminum thin film is then deposited and patterned as heaters on the surface of substrates. When an electrical current is applied, the temperature rises to activate the bonding process. Plastic materials are localized melted and bonded with the substrates. The example shown in Figure 74(a) is a MYLAR film coated with a

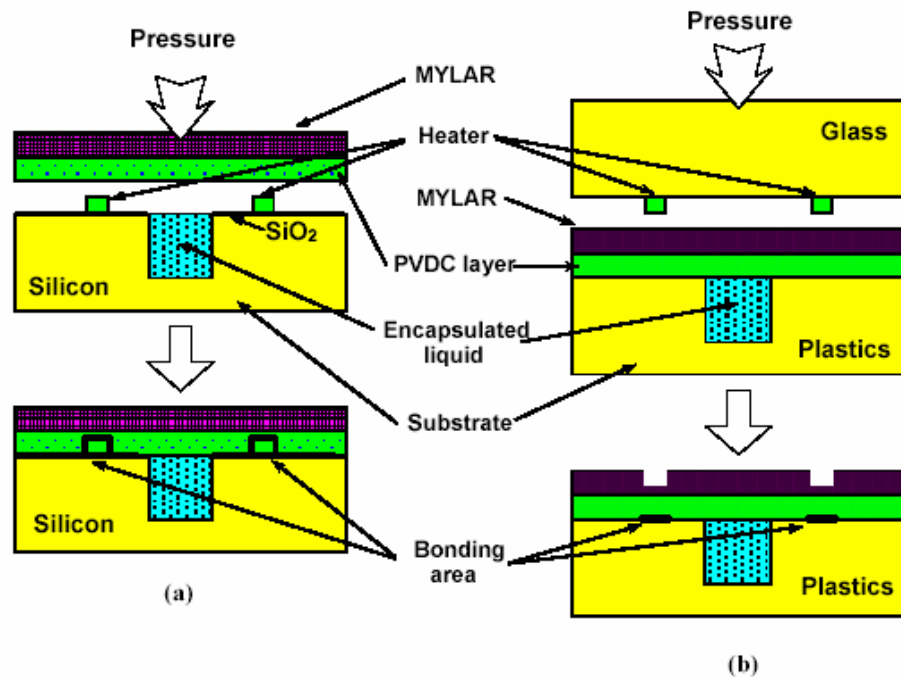


Figure 74: Schematic of bonding processes (a) built-in heater configuration (b) reusable heater configuration

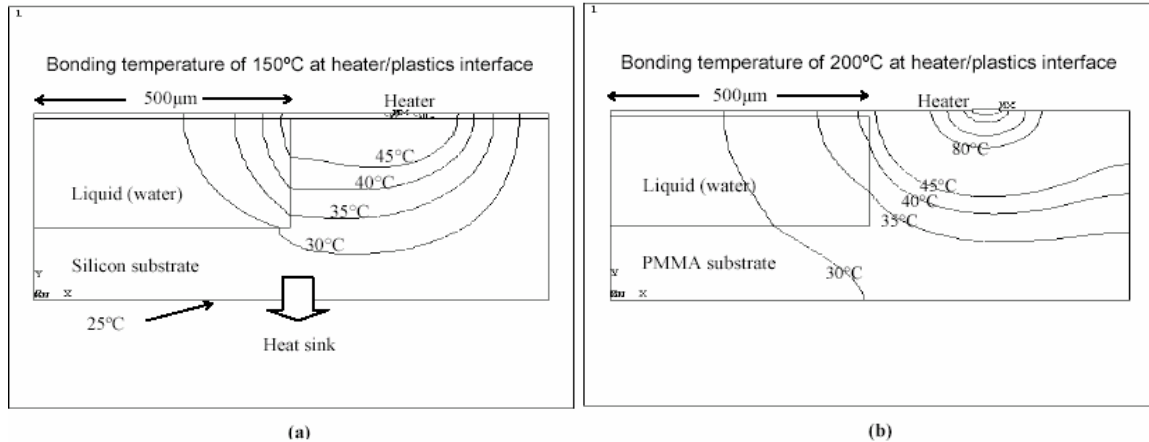


Figure 75: Temperature distribution of substrates after 0.25second of heating period (a) built-in heater with silicon substrate (b) reusable heater with plastic substrate.

thermoplastic polyvinylidene chloride (PVDC) copolymer layer. This scheme is suitable for bonding thick plastic materials with various types of substrates such as glass or silicon. For bonding of thin plastic films with substrates, a more efficient approach is employed as shown in Fig 74(b). Reusable heaters provide required bonding energy instead of built-in heaters. Heat is transferred through plastic thin film and a heated zone is generated locally in the bonding interface where the bond is formed. In this case, the plastic thin films have two layers as drawn. The material on the top layer should have a higher melting temperature to prevent bonding with the reusable heaters such that heaters can be removed at the completion of the bonding process and be reused repeatedly. Both bonding processes can be completed in 0.25 seconds and under about 0.4MPa of contact pressure

Finite Element Model (FEM) simulations have been performed to investigate the heat transfer behavior during the localized plastic bonding process with different material combinations [16]. Figure 75(a) and 75(b) are the transient thermal analyses showing the isotherms of the bonding experiments in Figure 74(a) and 74(b), respectively. In both cases, the thickness of aluminum is $6\mu\text{m}$, the thickness of the plastic thin film is $15\mu\text{m}$ and the cavity is 1mm in diameter and $300\mu\text{m}$ in depth. Both the silicon and plastic substrates are $500\mu\text{m}$ in thickness and the heaters are placed $200\mu\text{m}$ away from the encapsulation area. In the case of bonding plastic materials on a silicon substrate with built-in heaters, it is observed the edge of the encapsulation chamber will reach a temperature about 45°C in about 0.25 seconds. This is achieved by an insulating silicon dioxide layer of $1\mu\text{m}$ in thickness and a good heat sink on the backside of silicon substrate. The silicon dioxide layer provides good insulation to prevent global heating and the heat sink absorbs most of the extra energy supplied by the heaters. In the case of bonding by using reusable heaters, the low thermal conductivity of plastic materials prevents global heating if the heating period is short. As shown in Figure 75(b), the temperature increase caused by a heating period of 0.25 seconds will only raise a maximum temperature of $35\sim 45^\circ\text{C}$ around the cavity. These simulation results provide important information in controlling heat pulses to generate enough bonding energy without damaging the encapsulation materials.

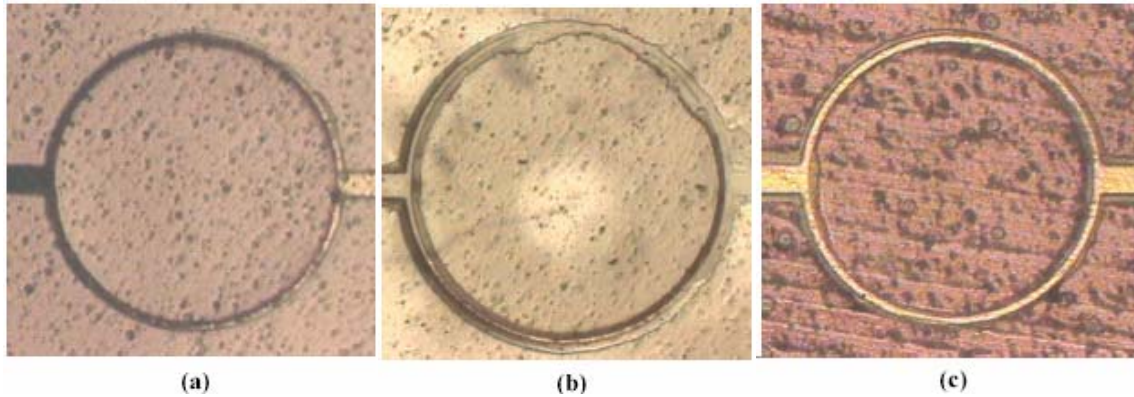


Figure 76: Bonding results of various substrate materials

(a) MYLAR on silicon (using built-in heater), (b) MYLAR on glass (using built-in heater) and (c) MYLAR on PMMA (using reusable heater).

Based on the principles of localized heating, microheaters have been built for various bonding experiments. In both schemes, aluminum wires of 30~70 μm wide and 6 μm thick are deposited and etched as the heating elements to form a bonding area of 2mm in diameter on either silicon or glass substrates. Because of the small bonding area (the area of the resistive heater is less than $9 \times 10^{-7} \text{ m}^2$), about 1 Newton of force is enough to provide the bonding pressure of 0.4MPa. In order to characterize the localized plastic bonding process, a series of experiments with different combinations of bonding conditions and materials have been conducted. Figure 76 shows localized plastic bonding results of various bonding systems, including plastics-to-silicon, plastics-to-glass and plastics-to-plastics. In these experiments, poly methyl methacrylate (PMMA) and polycarbonate (PC) substrates with thickness of 1~1.5mm are chosen as thick plastic materials for bonding. MYLAR plastic films [17] with a thermoplastic PVDC copolymer or ethylene vinyl acetate (EVA) layer on one side (complies with U.S. Food and Drug Administration regulation) of 15 μm in thickness are chosen as thin plastic film in the tests. The specific types used in the experiments, MYLAR M44 and RL53, are transparent such that the whole bonding process can be observed. By using the built-in heaters, a MYLAR film is placed directly on the top of aluminum microheaters for bonding. When a short pulse of 0.25 seconds is applied, the PVDC (heat-seal temperature at 140°C) layer is melted and adhered to the silicon substrate as shown in Figure 16(a). The width of the aluminum heater is 30 μm and it appears that the finished bonding width increases to around 50 μm .

On the other hand, when the MYLAR film is bonded with glass substrate as shown in Figure 76(b), the finished bonding width increases to about 70 μm . Glass substrate is not a good heat sink as compared with silicon substrate. As such, a wider heating area is expected to create a wider bonding stripe as shown. By using the reusable heaters, the MYLAR film is aligned with heaters. In this case, a higher heating power is provided such that the heat can penetrate through the thin film and provide energy at the bonding interface. The MYLAR film (melting point at 254°C) is not damaged in this case because the temperature of aluminum heater is controlled at around 200°C. Standard

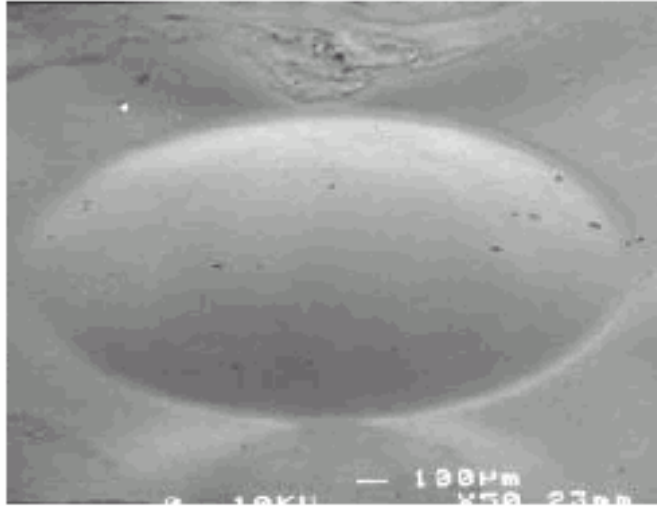


Figure 77: A dome shape is formed under SEM micrograph of MYLAR to PMMA showing good seal is achieved

heating period, temperature, and contact pressure of 0.25 seconds, 140°C, and 0.4MPa, respectively are applied for the plastic bonding experiment. Shown in Figure 76(c) is the result of MYLAR on PMMA substrate by using reusable heater and the finished bonding width is about 100µm. Because of the requirement for heat penetration of the thin MYLAR film for bonding, the localized heating zone is the largest one among the three tested bonding systems and has the largest finished bonding width.

To test the quality of plastic bonding, several experiments have been designed. First, bonded systems are put into a vacuum chamber and observed under an optical microscope. It is found that the top of the encapsulated chamber expands to form a dome shape due to the pressure unbalance as soon as the vacuum chamber is turned on. Figure 77 is a micrograph taken under SEM showing the result of MYLAR bonded on PMMA. It takes about 50 days for the air inside the cavity to diffuse out. Second, leak tests in liquid have been conducted to verify the seal. The leak tests are conducted by immersing sealed cavities into isopropanol alcohol (IPA). Because of its good wettability, IPA can easily penetrate small openings to verify the seal under an optical microscope. The testing results show 95% successful rate out of 50 samples and failures are caused by particles in the bonding interface. The yield can be further improved if the bonding process is conducted in the clean room. Finally, the plastics-to-plastics bond is forcefully broken to examine the bonding interface. After breaking the MYLAR to PMMA bond, the bonding interfaces are examined under SEM as shown in Figure 78. It is observed that the bonding result is uniform and part of the MYLAR film is attached to the bonding substrate. These indicate that very strong bonding is achieved.

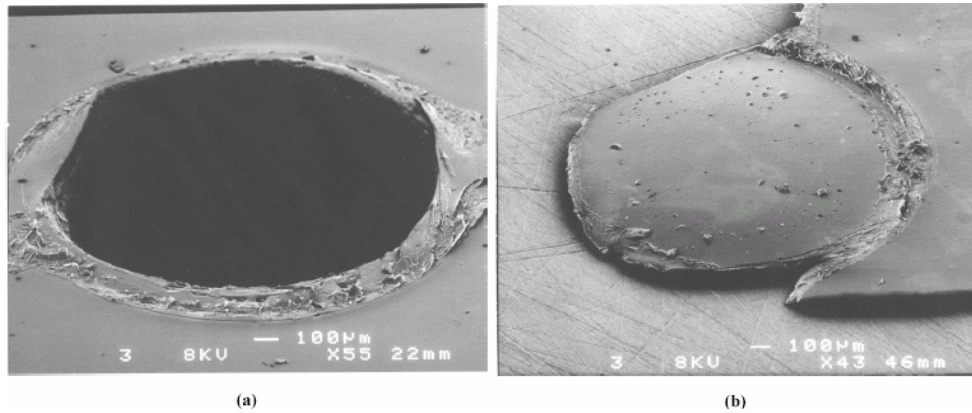


Figure 78: SEM micrographs of bonding interface
(a) PMMA substrate and (b) Mylar layer.

The encapsulation of water in the micro cavities is also performed to demonstrate the low processing temperature and good sealing of localized plastic bonding. The process of MYLAR to PMMA bonding with reusable-type heaters is performed to encapsulate about $1\mu\text{l}$ of water in the cavity as shown in Figure 79. The close view photograph on the topside shows two small bubbles in the water-filled and encapsulated chamber. These bubbles provide an easy way to verify the existence of water in the chamber. No leakage path can be identified and it takes about 2 months for the water to evaporate by the diffusion process through the top MYLAR membrane.

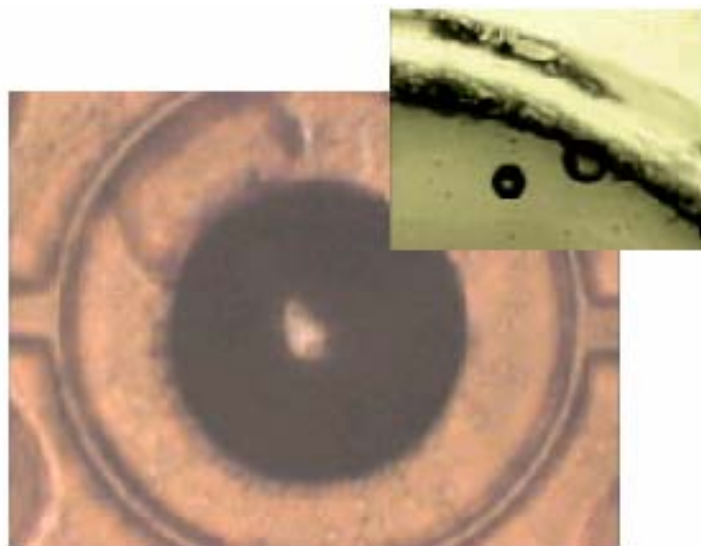


Figure 79: Photograph of water encapsulation result

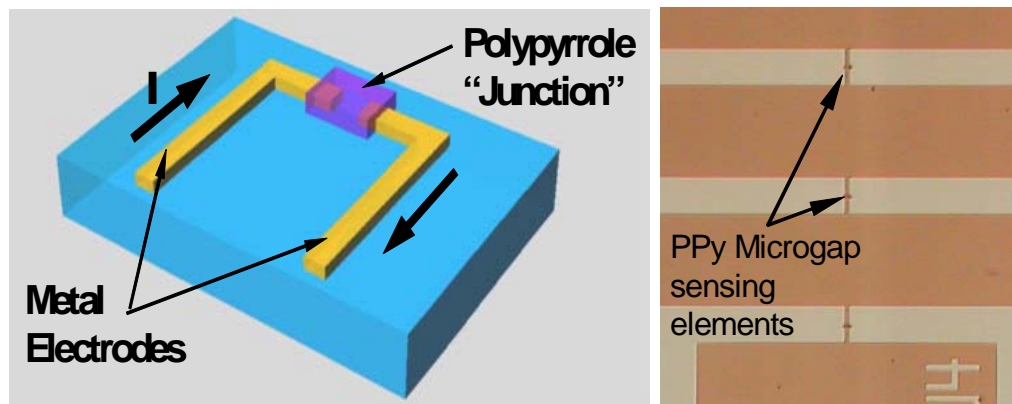


Figure 80: Conceptual design of a polypyrrole (PPy) micro-gap sensor array

It consists of a disjointed pair of metal electrodes bridged by a PPy junction. The PPy junction acts as a sensing element whose conductivity is modulated by analytes such as water molecules, cations and anions.

4.5.2 A Micro-gap PH Sensor

A novel and mediatorless glucose bioassay has been constructed, as shown in Figure 80. Instead of using the conventional Clark-type amperometric sensing technique, glucose sensing through simple conductance measurements will be demonstrated. The merits of this method versus conventional amperometric sensing include: 1) its simplicity in fabrication and measurement (which only requires an I-V measurement, as compared to cyclic voltammetry or amperometry), 2) electron mediators, usually toxic in nature, may not be required, and 3) it can be easily scaled up into a multi-analyte sensor. The sensor will consist of a pair of metal line electrodes deposited on top of an insulating substrate (Pyrex™, or Si_xN_y on Si) in a collinear fashion, whereby a 2 μm gap separates them.

Two proof-of-concept sensors for humidity and pH sensing are demonstrated first in this section. The micro-gap is bridged by a layer of electropolymerized polypyrrole (PPy), forming a conductive sensing junction across which most of the potential drop occurs. The conductivity of PPy can be reversibly modulated by humidity and pH change, due to charge alteration to the delocalized π-electron system in the polymer backbone. Figure 81 outlines the sensor fabrication process. Ti/Pt line-electrodes are first sputter-deposited and patterned on an insulating substrate via a ‘lift-off’ process. Next, 2000Å of low-temperature oxide (LTO) is deposited at 400°C and patterned by an anisotropic reactive ion etch (RIE) in CF₄ plasma to expose the micro-gap electrode which will form the sensing site. A room-temperature, one-step electropolymerization process is next performed in an aqueous solution that contains 0.1 M each of pyrrole (Py) monomers and sodium dodecylbenzenesulfonate (NaDBS). During the polymerization, PPy is potentiostatically (0.55V vs. Ag/AgCl) deposited onto the metal electrodes as an

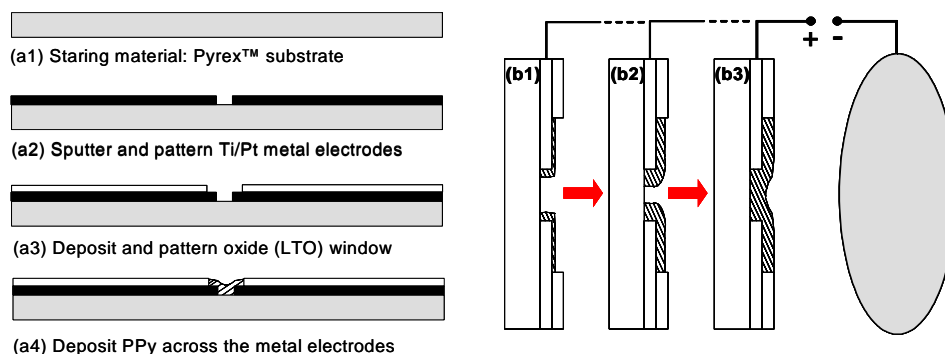


Figure 81: A micro-gap sensor

Illustrated in (a1-a4) is the wafer fabrication procedure, while (b) shows the electropolymerization process of PPy across the micro-gap. (a1) The fabrication process begins with an insulating substrate, Pyrex™ (a1), and followed by the deposition and patterning of Ti/Pt (a2) and LTO (a3). Next, the wafer is immersed in 0.1M of pyrrole solution for PPy electropolymerization (+0.55V vs. Ag/AgCl)(a4). (b1-b3) show how the isotropic growth of PPy from pyrrole monomers eventually leads to the bridging of the metal electrodes. The cathode (-) is made up of a Pt coated Si wafer.

opaque film (nominal thickness $\sim 5 \mu\text{m}$), the opacity of which increases with thickness. The film is then rinsed and soaked in deionized (DI) water overnight to remove trapped protons, which were released near the electrode surface during the electropolymerization process. Finally, the film is dried at ambient temperature with a nitrogen gun, and stored at 4°C .

Figure 82 shows the micro-gap electrodes prior to and after PPy deposition, and SEM micrographs of the PPy surface morphology. The deposition rate is optically measured to be $\sim 0.167 \mu\text{m}/\text{min}$, yielding PPy films of $5 \mu\text{m}$ thick in a 30-minute deposition process as portrayed in Figure 82(a'). As seen in Figure 82(b), PPy has a surface texture characterized by sub-micron diameter nodules, which agrees with previously observed morphology. The nodular surface texture increases the overall surface area of PPy, and could improve the detection sensitivity of gas molecules.

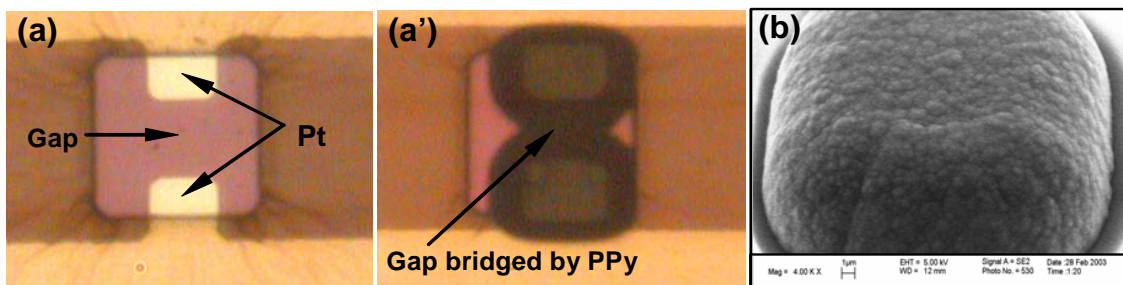


Figure 82: Pt electrodes

(a) and (a') show the electrode (Pt) prior to and after deposition of PPy. The width of the electrode and the gap are 8 and $10 \mu\text{m}$, respectively. The nominal thickness of the PPy film is $\sim 5 \mu\text{m}$. (b) The surface morphology of PPy grown at 0.55V (vs. Ag/AgCl) for 30 mins.

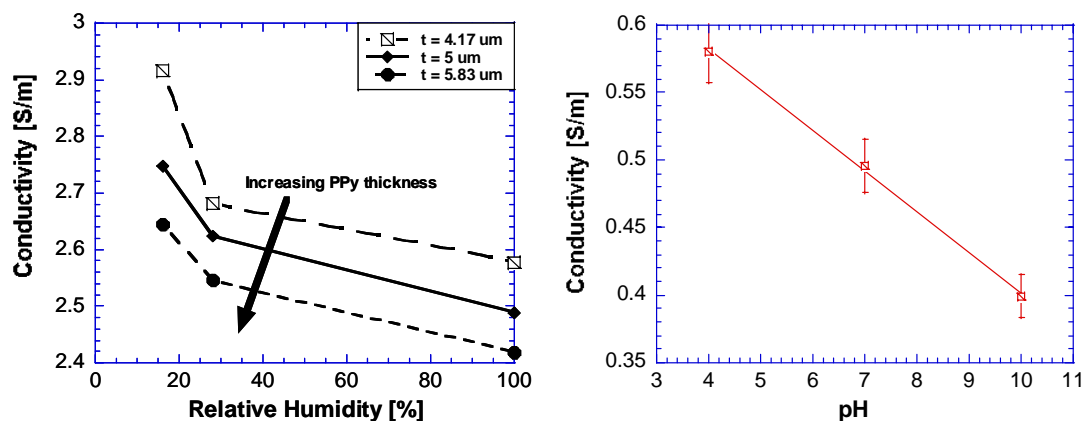


Figure 83: (a) Humidity sensing results showing conductivity change for different PPy film thickness (t) and (b) pH sensing results showing decreasing conductivity with increasing pH

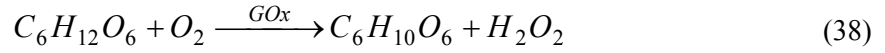
Figure 83(a) shows the humidity sensing results at room temperature. Compared to conventional humidity sensors that have typical response times of 15-60s, the PPy-based micro-gap sensor equilibrates and stabilizes within 5s. Sensitivity of the sensor is ensured by the large PPy resistance change (6-8 k Ω) at various moisture contents. As seen, conductivity of PPy decreases with increasing moisture content in the polymer due possibly to lower charge mobility caused by the polymer chain-stretching, as a consequence of the insertion of water molecules into the polymer mesh. In addition, we also hypothesize that water molecules may form proton traps which decrease the conductivity of the polymer. This observation has been previously made on hydrogen gas sensor based on fullerene molecules (C₆₀), where in the presence of moisture, fullerene molecules lose its hydrogen sensing property due to the formation of electron traps by water molecules. These explanations could be partially verified by subsequent experiments where the conductivity of dry PPy film, upon being immersed in aqueous solutions, decreases by an order of magnitude.

Figure 83(b) shows pH sensing results under room temperature. By immersing the sensor in pH 4, 7 and 10 calibrating fluids and rinsing with copious amount of DI water in between sampling, the resistance is observed to increase from 343.8 k Ω to 403 k Ω to 500 k Ω . The higher conductivity at lower pH is likely due to increased p-doping brought about by excess H⁺ ions, and also to deprotonation at higher pH, where OH⁻ acts as a nucleophilic agent which effectively cleaves the N-H bond by removing the H.

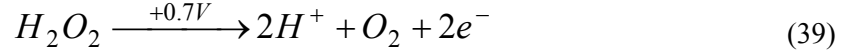
4.5.3 A Polypyrrole-Carbon-Nanotube Nanocomposite Glucose Sensor

To date, amperometry remains the de facto method for detecting glucose concentration. In the Clark-type or amperometric glucose sensing method, glucose molecules are detected at the enzyme-modified anode following enzymatic reaction with the glucose-specific redox enzyme, glucose oxidase (GOx). GOx is typically immobilized on the anode by means of physisorption, physical entrapment or covalent attachment. In the presence of oxygen, glucose (C₆H₁₂O₆) is enzymatically oxidized at the anode to yield

gluconolactone (C₆H₁₀O₆) and hydrogen peroxide (H₂O₂) according to the following equation:



Subsequently, at an oxidizing potential of +0.7V, H₂O₂ is oxidized by donating 2 electrons at the anode, which is detected as a current flow that correlates linearly with the concentration of glucose.



Albeit chemically simple, this reaction cascade masks the fact that electron mediators, usually cytotoxic by nature, are often required to effectively shuttle electrons from the enzyme active site, flavin adenine dinucleotide (FAD), to the working electrode. Also, as the potentiostatic measurement scheme requires the use of a reference electrode made of Ag/AgCl, additional fabrication steps are usually necessary, adding to the complexity and cost of production. Finally, as the current flow is directly proportional to the area of the electrode, miniaturization of electrodes significantly reduces the magnitude of the current detected into the nA range, hence necessitates the use of ultra-precise measurement equipments such as a biopotentiostat. For this reason, traditional biopotentiostat-based amperometric glucose sensor remains the benchmark for glucose sensing. However, its bulkiness, operating complexity and high cost of electronics prohibits its adoption as a point-of-care system outside of hospitals and research laboratories. Hence, real-time, accurate and low-cost glucose sensing continues to represent an elusive goal to biomedical researchers and the diabetic population.

A simple, versatile and rapidly-regenerable two-terminal glucose sensor was constructed that was consist of the passive glucose sensing element made of a conducting polymer-organic nanocomposite material – polypyrrole-multi-walled carbon nanotube (PPy-MWNT). The sensor architecture obviates the need for a reference electrode as well as electron mediators. In addition, PPy-MWNT is an attractive sensing material due to its redox-modulated electronic conductivity, non-cytotoxicity, low cost of production and superior environmental stability. PPy is one of the most researched conducting polymer inasmuch as its relative environmental stability and interesting properties such as biocompatibility, redox-tunable conductivity and ease of processibility. In the absence of dopant, pristine PPy (E_g ~ 3.2 eV) is an insulator. However, once it is doped, it functions as a polymeric semiconducting material whose conductivity can be altered to different extents via the incorporation of anionic dopants such as perchlorate (ClO₄⁻), tetrafluoroborate (BF₄⁻), sulfate (SO₄⁻), chloride (Cl⁻), dodecylbenzenesulfonate (DBS⁻), and p-toluene sulfonate (PTS⁻). Additionally, depending on the charge and size of the specific dopant added, the conductivity may be reversibly modulated by external parameters such as temperature and pressure, as well as secondary dopants such as water molecules, protons, and reducing/oxidizing gas molecules (NH₃, Cl₂).

In spite of these advantages, unlike metal, most conducting polymers, including PPy, are still very much sensitive to the environment, and their electrical properties also tend to deteriorate over time due to overoxidation (an irreversible oxidative degradation

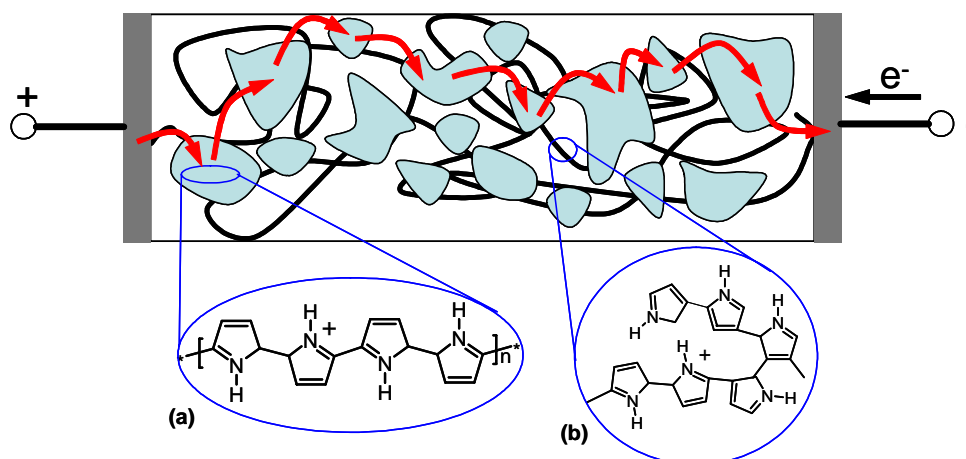


Figure 84: General scheme of polypyrrole conduction

The shaded patches (a) indicate the conductive (charge delocalization) region and the solid curve (b) shows the insulating (charge localization) region. Due to the existence of conductive and non-conductive regions, charge transport proceeds through a ‘hopping’ mechanism (as indicated by the arrows), whereby charge-induced defects, or polarons, hop between islands of conductive region, from the positive to the negative terminal.

process), mechanical perturbation (twisting and bending), moisture, temperature (heat introduces permanent configuration change of its polymer backbone such as coiling) and chemical alteration (such as nucleophilic attack initiated by strong bases). The sensitivity to environment could be understood from its charge transport mechanism.

Figure 84 shows a simplified model of charge transport mechanism in PPy. An as-polymerized, doped PPy consists of a random mixture of conducting and non-conducting domains. Upon the injection of a hole, a defect in the polymer chain (‘polaron’) is created, and it propagates along the chain via a ‘hopping’ mechanism, where conduction is achieved when the polarons hop over islands of conducting domains. The sizes and proportions of such conducting domains, however, can be greatly diminished by the aforementioned detrimental factors. Hence, to reduce the hopping resistance and to facilitate smoother flow of charges, one of many ways is to reduce the dependence of the electrical property on the polymer backbone configuration by increasing the charge carrying paths within the polymer structure. This can be achieved via incorporating conducting nano-sized domains such as multi-walled carbon nanotube (MWNT), activated carbon black, as well as inert and highly conductive nanoparticles such as gold and platinum. In particular, MWNT not only increases the charge carrying capacity, due to its high surface-area-to-volume ratio, composite of PPy and MWNT has also been reported to be good charge storage device. The latter property greatly prolongs the stability of PPy by ameliorating the effect of overoxidation. We will exploit this property in designing a stable glucose sensor.

Figure 85 (a) and (c) illustrates the conceptual schematic view and an oblique SEM photo of a fabricated PPy-MWNT glucose sensor, where the sensing circuit comprises a pair of metal line-electrodes separated by a $5\mu\text{m}$ gap. The micro-gap is

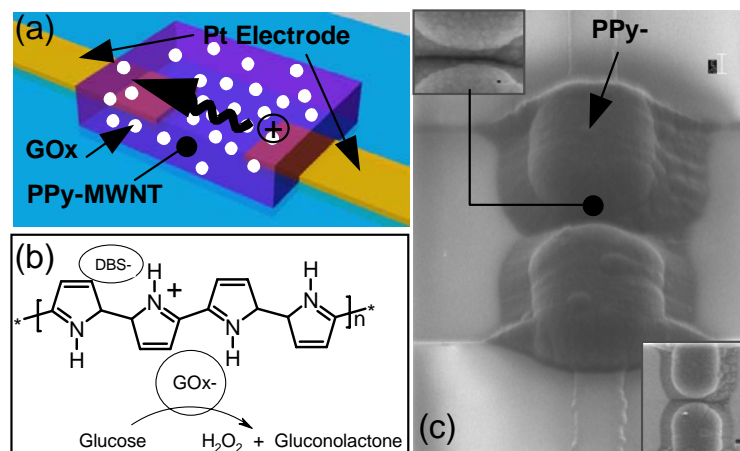


Figure 85: Glucose sensor

(a) Schematic of a PPy-MWNT glucose sensor that operates based on redox-induced conductivity change of the nanocomposite junction. (b) 2-D representation of the DBS-doped PPy-MWNT with GOx embedded. GOx oxidizes 1 mole of glucose to produce 1 mole each of H_2O_2 and gluconolactone. H_2O_2 thus produced is found to enhance the conductivity of PPy-MWNT proportionately. (c) Oblique view of a fabricated PPy-MWNT sensor as seen through a scanning electron microscope. Top & bottom insets show the closed-up view of the bridged microgap, and the top view of the sensor.

connected by a layer of GOx-encapsulating, electropolymerized PPy-MWNT, forming a conductive sensing junction across which most of the electric potential drop occurs. Figure 85 (b) illustrates the glucose enzymatic reaction that produces hydrogen peroxide (H_2O_2), a strong oxidant which enhances the conductivity of PPy-MWNT by injecting holes into the delocalized π -electron system in the polymer backbone.

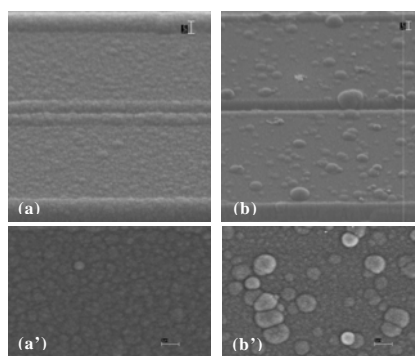


Figure 86: PPy and PPy-MWNT

The oblique (45°) views of the PPy (a) and PPy-MWNT (b) microgap sensor ($1000 \mu m$ wide x $5 \mu m$ gap). The original gap region produces a groove after polymerization, as shown at the center of (a) and (b). The surface morphologies of the PPy (a') and PPy-MWNT (b'), respectively, as seen from the top. PPy-MWNT has a more nodular grain structure and higher surface roughness than PPy.

The fabrication process is similar to the previous section, 4.5.2. Figure 86 juxtaposes the post-deposition SEM micrographs of the electropolymerized PPy and PPy-MWNT surface morphologies. In the absence of MWNT, as illustrated in Figure 86 (a, a'), the surface roughness of PPy is relatively lower. With the embedding of MWNT, as shown in Figure 86 (b, b'), the formation of PPy nodules is favored and causes the surface roughness of PPy-MWNT to increase. The deposition rate is optically measured as 0.43 $\mu\text{m}/\text{min}$, yielding PPy films of 6.5 μm in a 15-minute interval. Figure 87 shows the room-temperature conductivity change of both PPy and PPy-MWNT sensors (1000 μm wide x 5 μm gap) at concentrations of β -D-glucose ranging from 0 to 20mM. As seen, in the low detection range (0-10mM), the conductivities of both sensors rise with increasing glucose concentrations, with PPy-MWNT increases to a larger extent than PPy. However, at 20mM, only PPy-MWNT continues to function. We hypothesize that, since PPy is the only conductive path carrying charges in PPy, H_2O_2 produced in the enzymatic oxidation of β -D-glucose likely overoxidizes the PPy polymer chain beyond its maximum charge capacity threshold and causes its conductivity to decrease due to extensive localization or trapping of charges within the polymer. On the other hand, for PPy-MWNT, its superior specific capacitance allows it to store the excess redox charges, and prevent them from damaging the PPy backbone by overoxidation, hence preserving its electrical integrity. To verify that H_2O_2 causes the change in the device, various concentrations of H_2O_2 have been added to a PPy-MWNT sensor (12 μm wide x 5 μm gap). The results (Figure 88) illustrate that PPy-MWNT is able to detect H_2O_2 in a linear fashion between 0-400mM and validates the aforementioned hypothesis that H_2O_2 acts as a powerful oxidizing agent. It p-dopes the PPy-MWNT composite to enhance its conductivity, and PPy-MWNT nanocomposite has superior capacitance that allows it to function even at high levels of oxidation.

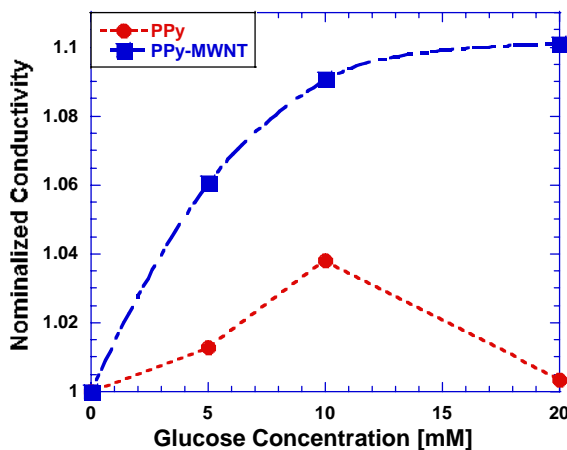


Figure 87: Conductivity v. Glucose Concentration

Both PPy and PPy-MWNT sensors detect glucose, however, PPy-MWNT exhibits a larger detection range (up to 20mM), and also a larger change in conductivity per unit glucose concentration. This capability could be due to the much-enhanced specific capacitance of PPy-MWNT which helps preserve the electrical integrity of PPy polymer backbone and prevent it from being overoxidized by H_2O_2 .

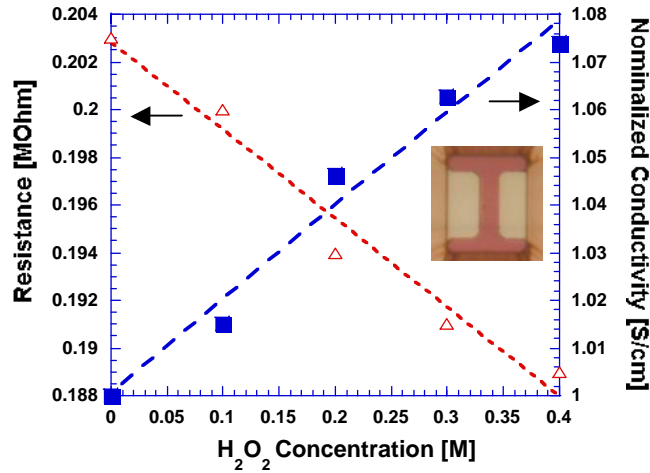


Figure 88: The nominalized conductivity and resistance of the microgap PPy-MWNT sensor

The inset shows a pair of microgap electrodes (12 μ m wide x 5 μ m gap) used for this measurement and prior to PPy-MWNT deposition.

4.5.4 Control Circuitry

The control and sensing circuits must have high resolution and low power consuming and can be programmed. We are working to build a prototype circuit to accomplish this task at this moment. After the testing circuit is complete and its performance is demonstrated, the part will be processed on the silicon chip and integrated with all the other parts of the system to complete the bioassay system. A low-power Digital Signal Processor (DSP) is chosen as the microprocessor and display part such as LCD is selected to display the measured result. The sensor from water-powered bioassay system is in the developing process such that other sensors available in the commercial market are picked up to test the control program and circuit. Figure 89 shows the diagram of control and sensing circuit.

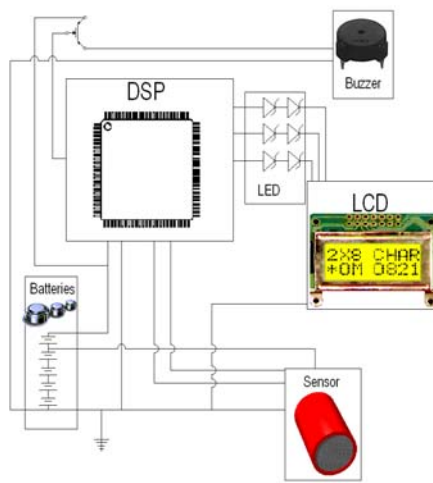


Figure 89: Diagram of control and sensing circuit

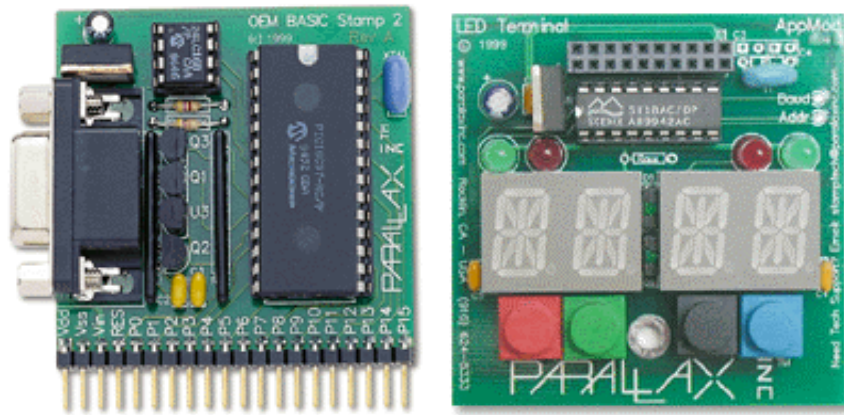


Figure 90: Parallax microprocessor (left) and LED (right)

To make the control and display unit prototype easier to accomplish and more compatible to the simple function and structure at this stage, the first prototype was fabricated with a Parallax, Inc. OEM™ microprocessor and LED, providing ease and flexibility of integration (Figure 90). The OEM has a relatively simple logic, so the chip and the peripheral components were much simpler than using a DSP. The basic control and display functions were demonstrated before upgrading the system to a higher level. Together the OEM and the LED were also easily and highly programmable.

The housing unit of the first prototype was changed to accommodate all the components (Figure 91). The final prototype had three layers. The upper layer was a LED, the second layer was the OEM, and the bottom layer was the circuit board and the power station. The main reason that a bigger housing was chosen was the size of the OEM and LED. The minimum space between the layers was determined by the tallest component on the lower layer. This system size will be greatly reduced at chip-level system integration.

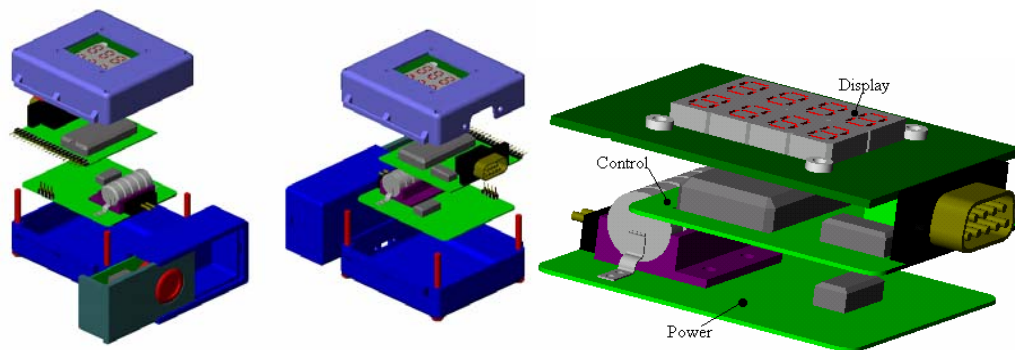


Figure 91: The housing unit of the system
An enlarged view of the internal unit is on the right.

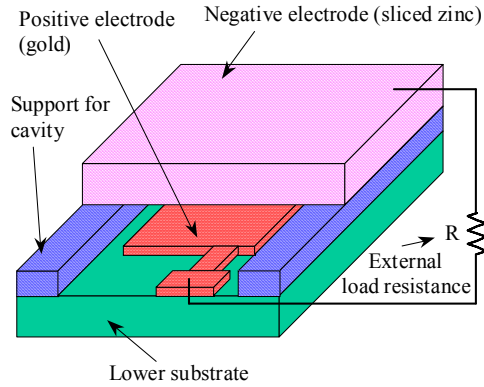


Figure 93: Schematic of a liquid-electrolyte microbattery

Both positive electrode (gold) and supports for forming the electrolyte cavity are placed on the lower substrate while the negative electrode (zinc) is constructed on the cap substrate; the microbattery works after putting liquid electrolyte (see Figure 95).

The power source is an indispensable component for a MEMS device. Previously, principles of solar cells and micro combustion have been investigated by using rather complicated micromachining processes. This work presents an alternative approach by using electro-chemical reaction of liquid electrolyte as the power source. Liquid electrolyte is placed in a micro cavity that is formed by two electrodes with opposite polarity as shown in Figure 93. In this preliminary demonstration, sulfuric acid (H_2SO_4) is chosen as the liquid electrolyte, gold is used as the positive electrode and zinc is used as the negative electrode. The cap substrate can be thermally bonded to the lower substrate or simply glued together by using an adhesive agent. The operation of the battery can be on-demand by putting a droplet of electrolyte in front of the cavity. Surface tension force drove the electrolyte in, causing the cavity to fill as shown in Figure 94. When the battery is connected to an external load, the electro-chemical reaction of $Zn + H_2SO_4 \rightarrow ZnSO_4 + 2e^-$ occurs and electrons are collected at the positive electrode (gold).

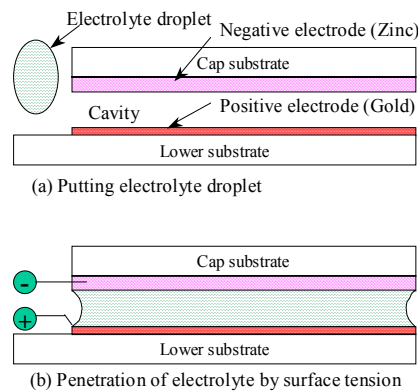


Figure 94: Working principle of the microbattery

(a) By upon putting a liquid-electrolyte droplet in front of the cavity, the electrolyte penetrates into the cavity by surface tension and (b) the microbattery supplies power.

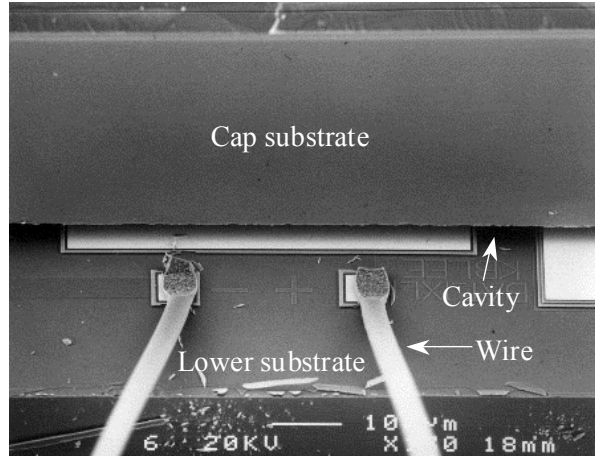


Figure 95: SEM micrograph of capped microbattery before inserting liquid-electrolyte

In Figure 95 is shown the capped microbattery fabricated by a standard surface-micromachining process before inserting liquid electrolyte. Two wires for experimental measurements are also shown. The output voltage of the battery is measured with respect to time by using a load resistance of $1\text{M}\Omega$ as shown in Figure 96 with one droplet of electrolyte. It is found from the diamond indicator of Figure 96 that the measured voltage decreases gradually with time with a maximum value of 1.06V about 15 minutes after operation and the value reduces to 0.36V after 50 minutes of operation. The estimated battery capacity is $1.1\mu\text{W}\cdot\text{hour}$. It is foreseeable that the voltage, current and capacity of the microbattery can be improved by making series, parallel battery designs as well as by choosing other electrolyte systems. This microbattery appears to be feasible for on-demand and disposable MEMS devices that urgently require low cost, small size power sources that are compatible with common MEMS fabrication processes, including the CMOS process.

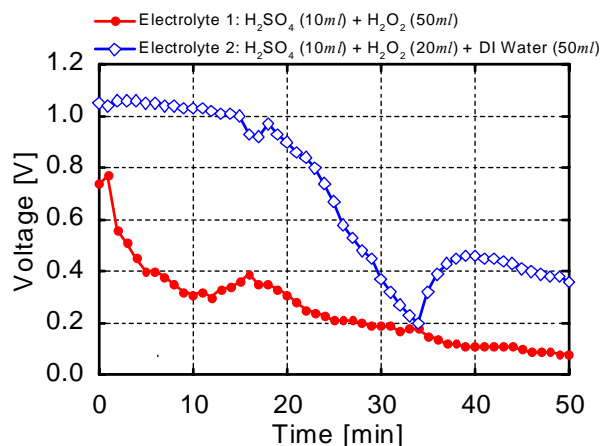


Figure 96: Measured voltage of the microbattery with a load resistance of $1\text{M}\Omega$

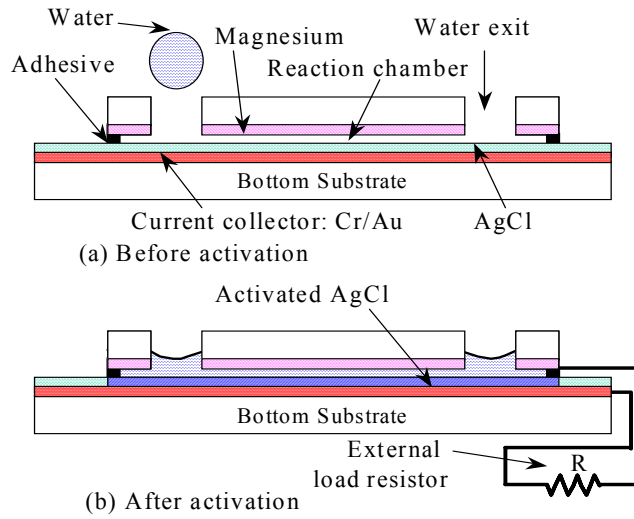


Figure 97: Working principle of the water activated microbattery

- (a) Chemicals are not activated before putting water into the system (b) Water activates silver chloride, and the microbattery becomes functional to supply power.

4.6.2 Water-activated, Long Shelf-Life Microbattery

The major accomplishment here is the design of a water-activated microbatteries with long shelf life. Figure 97 shows the operation principle of the microbatteries that use magnesium (Mg) as the anode on the top substrate, and silver chloride (AgCl) or cuprous chloride (CuCl) as the cathode on the bottom substrate. The two pieces are bonded together by an adhesive to create the reaction chamber. Before water is added, there is no contact between these chemicals and no reaction is expected such that these microbatteries could have a long shelf- life. When water is added into the system, surface tension force drives it to fill the reaction chamber. Chemicals dissolve and react to produce electricity. The chemical reactions for the water-activated magnesium-silver chloride microbatteries at the anode (oxidation) and cathode (reduction) are represented as Eqs. (40) and (41), respectively:



The overall reaction is:



If cuprous chloride is used as the cathode, Eq. (10) is modified as:



and the overall reaction is:



It is observed from Eqs. (40)-(44) that when electrons flow through the external load resistor, ions such as Cl^- and Mg^{2+} flow within the electrolyte. The theoretical voltage of a cell is a direct function of the anode and cathode materials. The standard potential of a cell can be calculated from the standard electrode potentials as the sum of the anode potential and the cathode potential:

$$E^0 = E_{anode}^0 - E_{cathode}^0 \quad (45)$$

where E_{anode}^0 and $E_{cathode}^0$ are the anode oxidation potential and cathode reduction potential, respectively. The oxidation potential of a material is the negative value of its reduction potential. Using Eq. (45), the standard potential of the Mg-AgCl microbattery is calculated as 2.585V. Similarly, the theoretical voltage of the Mg-CuCl microbattery is calculated as 2.487V.

The capacity of a cell, as defined by coulombs (C) or ampere-hours (A-hr), can be expressed as the total quantity of electricity involved in the electrochemical reaction. Theoretically, one gram-equivalent weight of a material that is defined as the molecular weight divided by the number of electrons involved in the reaction will deliver one Faraday (96,500C) or 26.8A-hr. Hence, the theoretical electron capacity per unit weight, C_{el} , can be defined as follows:

$$C_{el} = \sum \frac{nF}{\text{weight of reactants}} \quad (46)$$

where n is the number of electrons exchanged in the reaction and F is Faraday's number. Using Eq. (46) and the material properties from Table 4, the theoretical capacity per unit weight for the Mg-AgCl battery is 620.62 C/g or 0.172 A-hr/g. Similarly, the theoretical capacity per unit weight for Mg-CuCl battery is 868.20 C/g or 0.241A-hr/g. The energy capacity per unit weight of batteries, C_{en} , is derived using $(C_{en} - E^0 C_{el})$, where C_{en} is in W-hr/g, E^0 is in Volts, and C_{el} is in A-hr/g. Consequently, the energy capacities of the

Table 4: Reduction Potential and Weights of Chemicals.

<i>Anode</i>	<i>Cathode</i>	$E^0 [V]$	$C_{el} [A-hr/g]$	$C_{en} [W-hr/g]$
Mg	AgCl	2.585	0.172	0.445
	CuCl	2.487	0.241	0.599

Table 5. Theoretical Performance of Mg-CuCl and Mg-AgCl Microbatteries.

Material	Balanced-half reaction	Reduction Potential E^0 [V]	Weight [g/mol]
Mg	$Mg^{2+} + 2e^- \rightleftharpoons Mg(s)$	-2.363	24.31
AgCl	$AgCl(s) + e^- \rightleftharpoons Ag(s) + Cl^-$	0.222	143.34
CuCl	$CuCl(s) + e^- \rightleftharpoons Cu(s) + Cl^-$	0.124	99.00

Mg-AgCl and Mg-CuCl batteries are 0.445 and 0.599 W-hr/g respectively. Table 5 summarizes the theoretical performance of the microbatteries presented here.

The fabrication process is illustrated in Figure 98. The water supply openings on the top substrate (Figure 98(a)) are fabricated using the Deep Reactive Ion Etching (DRIE) process to etch through a 4-inch silicon wafer. A 15 μ m-thick magnesium film is then deposited by using the evaporation process. It is expected that magnesium will also be deposited partially onto the sidewall. In Figure 98(b), a Cr/Au layer of 200 \AA /2000 \AA is deposited using the sputtering process first as the current collector. Afterwards a layer of 20 μ m-thick Ag layer is deposited by sputtering and then chlorinated to form the AgCl cathode. For CuCl, a 1.5 μ m-thick CuCl can be evaporated as the cathode. Alternatively a 20 μ m-thick CuCl can be deposited by a screen-printing process as an inexpensive way to increase the amount of the chemicals for longer battery operation. Figure 98(c) shows that both substrates are bonded to create a reaction chamber. The height of the chamber was controlled to be 50 μ m, 100 μ m, and 200 μ m, by using various spacers in the binding process. Moreover, microbatteries with different electrode areas have been fabricated, including 12mmx12mm, 8mmx8mm, 6mmx6mm, and 4mmx4mm. These microbatteries were tested experimentally to characterize the effects of geometrical variations. The fabrication process for microbatteries is compatible with most MEMS processes such that

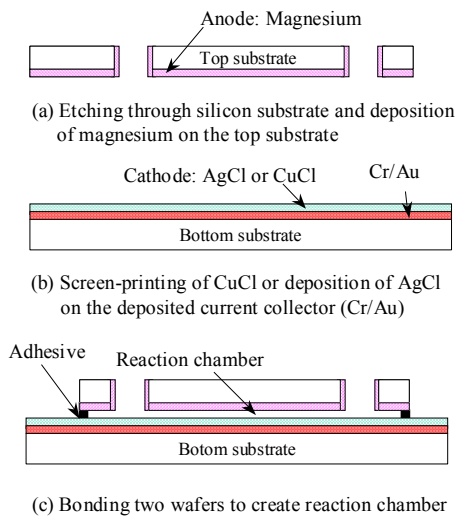


Figure 98: Fabrication process for the microbattery

An adhesive bonds two wafers and creates a reaction chamber.

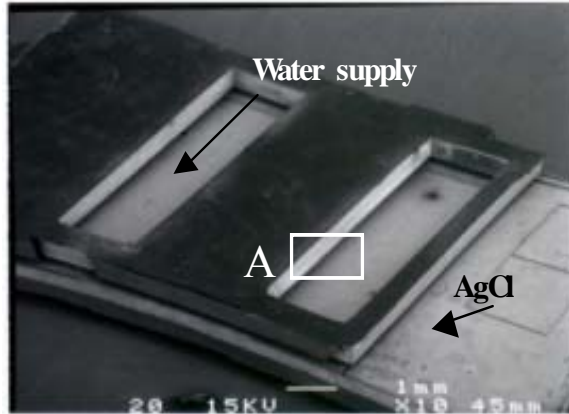


Figure 99: SEM micrograph of a fabricated microbattery

The electrode area is $8\text{mm} \times 8\text{mm}$.

direct integration could be possible for disposable microsystems to have on-chip power sources. Figure 99 shows an SEM of a fabricated microbattery. The electrode area of the microbattery is $8\text{mm} \times 8\text{mm}$. Figure 100 is the close up of the marker “A” in Figure 99 showing chlorinated AgCl at the bottom, the $100\ \mu\text{m}$ -high reaction chamber, and Mg deposited on the sidewall of the top substrate.

The output voltages of the microbatteries have been measured with respect to time under various discharge loads, electrode areas, cathode materials, and gap widths of the reaction chamber. Placing a droplet of water of $40\ \mu\text{l}$ in all experiments activated these

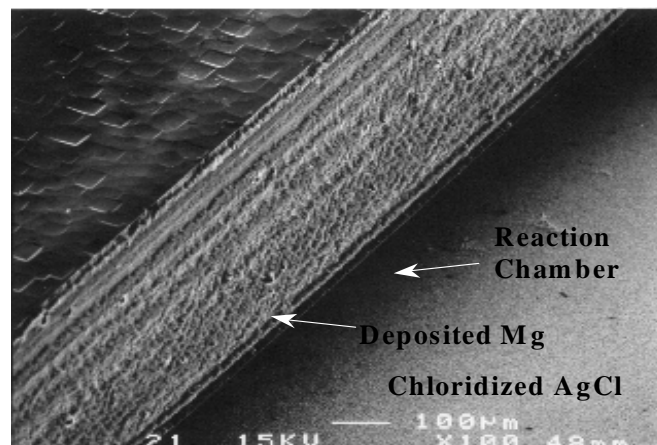


Figure 100: Magnified SEM micrograph of Figure 99

Chlorinated AgCl, gap of the reaction chamber and magnesium deposition on the sidewall of the top substrate.

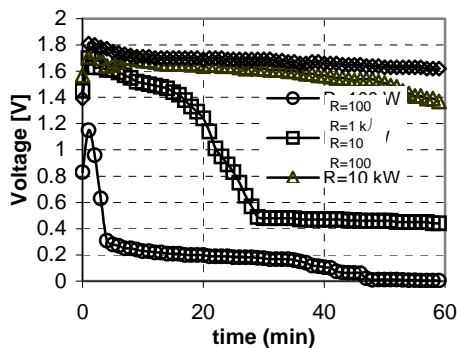


Figure 101: Measured voltage of the 8mmx8mm microbattery with AgCl as the cathode and a 100 μm -high chamber

microbatteries. Figure 101 shows the measured voltages of an 8mmx8mm microbattery that has a reaction chamber of 100 μm in height and uses AgCl as the cathode. When discharged at 1 k Ω , the voltage reached a maximum of 1.7 V after 1 minute of operation and the value reduced to 0.46 V after 25 minutes and remained at about this value for the rest of the operation. As noted in Figure 101, the measured voltage decreased with time and this is due to the chemical consumption within the batteries. Moreover, the voltage was lower when the batteries were discharged at a higher load resistance. The measured voltage, V_m could be approximately expressed as:

$$V_m = \frac{E_o R}{R + R_i} \quad (47)$$

where E_o is the theoretical voltage, R is the load resistance, and R_i is the internal resistance. It could be deduced from Eq. (47) that as load resistance increases, discharge voltage increases. Figure 102 shows the discharge curves under a 1k Ω load resistor for various electrode areas with AgCl as the cathode and the chamber height is 100 μm . As shown in Figure 102, the voltage decreases as the area decreases because batteries with larger electrode areas have less internal resistance.

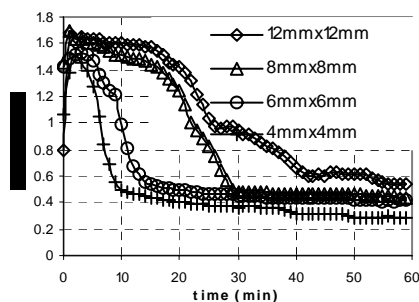


Figure 102: Measured voltage of microbatteries with AgCl as the cathode and a 100 μm -high chamber discharged at 1k-ohm

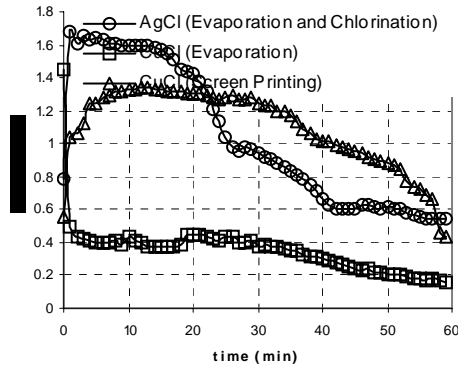


Figure 103: Measured voltage of the 12 mmx12mm micro-battery with a 100 μm -high chamber discharged at 1k-ohm

The performance of the microbattery for various cathode materials is compared in Figure 103. The measured voltage of the AgCl microbattery was higher than that of the screen-printed CuCl for about 22 minutes after which the measured voltage from the screen-printed CuCl microbattery was higher than that of the AgCl microbattery. Theoretically, CuCl microbatteries have lower output voltage than AgCl microbatteries. However, it is suspected that the rough topology of the screen-printed CuCl will result in larger electrode area to that of evaporated and chlorinated AgCl. This argument could explain the observed discharge behavior, namely that higher cathode area prolonged the discharge life of the screen-printed CuCl microbattery. On the other hand, the evaporated CuCl had an inferior performance in contrast to screen-printed CuCl because of the unavoidable presence of Cu atoms within the CuCl film during the evaporation process that consequently decreased the effective cathode area. The effect of reaction chamber height on the performance of the microbattery has also been studied. Figure 104 shows that the performance of the microbattery is enhanced as the chamber reaction height is reduced. As the gap between the cathode and anode is decreased, the resistance of the electrolyte within the reaction chamber is reduced. This results in a reduction in the internal resistance of the microbattery that consequently enhances the performance.

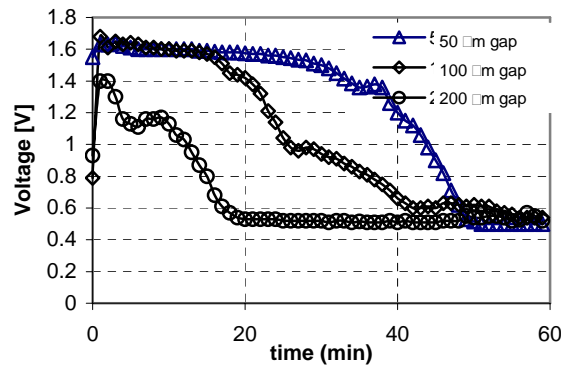


Figure 104: Measured voltage of the 12mmx 12mm microbattery with AgCl discharged under a load resistor of 1k-ohm

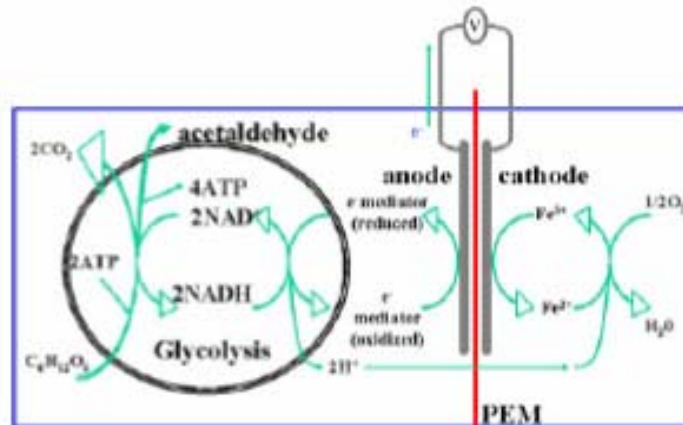


Figure 105: Operational principle of a microbial fuel cell

4.6.3 A Micro Microbial Fuel Cell

On the other hand, we have completed the micromachined microbial fuel cell task. Figure 105 shows the operation principle of a microbial fuel cell. In the anode compartment, bacteria, such as *Saccharomyces cerevisiae* (baker's yeast) is used as the bio-catalyst, and put into a buffer solution. Glucose (fuel) is fed to the microorganisms. Hydrogen protons, electrons and carbon dioxide are generated during the fermentation process. Two factors affect the design considerations of the microbial fuel cell: 1) the biocatalytic reaction should take place at the immediate vicinity of the Proton Exchange Membrane (PEM) such that the proton traveling distance can be minimized and the energy transfer efficiency can be optimized; and 2) the surface area-to-volume ratio of the anode and cathode compartments should be maximized to achieve high energy density as well as high coulombic-yield. Figure 106 shows the exploded-view of the micromachined microbial

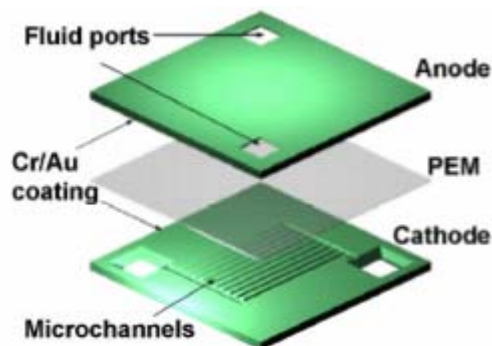


Figure 106: Design of a miniaturized microbial fuel cell

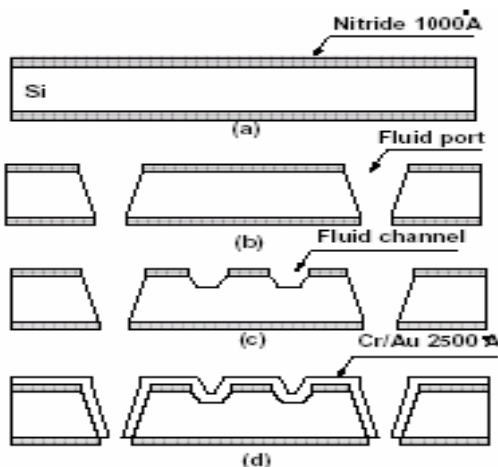


Figure 107: Fabrication process of the silicon micromachined microbial fuel cell

fuel cell. Based on the two design considerations described above, micromachined fluid channels are designed to form in the anode and cathode compartments to achieve high surface-to-volume ratio and grant the bio-catalyst and fuel access to the PEM. The microchannel surfaces are coated with Cr/Au as current collectors. Dupont Nafion-117TM film is used as the PEM and is sandwiched between the anode and cathode. The size of the microchannel is designed such that it allows the microorganisms to flow through and clogging can be avoided. Typically, the size of yeast cell is about 10 μm in diameter. Therefore, microchannels with sizes of 100 μm wide and 80 μm deep are designed.

The fabrication processes are shown in Figure 107. Silicon wafer is deposited with LPCVD low stress nitride of 1000 \AA in thickness as a hard mask (Fig 35(a)). The first step is used to define the fluid ports. The anisotropic etchant, KOH:H₂O=1:2 by weight at 80°C, is used to etch through the silicon wafer (Fig 107(b)). The second photolithography step is then used to define the fluid channel (Figure 107(c)). In this step, thick spin-on photoresist (thickness of 9 μm) is used to overcome surface roughness resulted from the first KOH etch. Timed etch in KOH etchant is then used to make 80 μm deep fluid channels. After the fluid ports and channels are formed on the silicon wafer, Cr/Au of 2500 \AA thick is thermally evaporated on to the silicon microchannel as the current collector (Figure 107(d)). The slanted channel wall enables a conformal deposition of Cr/Au and makes the electrical connection to the external world possible.

Figure 108 shows the SEM micrograph of a fabricated fluid port and channel. The area of the fluid port is 1000x1000 μm^2 and the channel width and length are 100 μm and 6200 μm , respectively. The total electrode area is 0.51cm² and the surface area-to-volume ratio is about 500 cm⁻¹ (the surface area-to-volume ratio with a plain electrode surface is only about 120 cm⁻¹ in this case). PEM is prepared. The cleaning procedure would allow metallic and organic contaminations on the PEM surface to be removed. Care must be taken when handling the PEM after it has been cleaned to maintain its

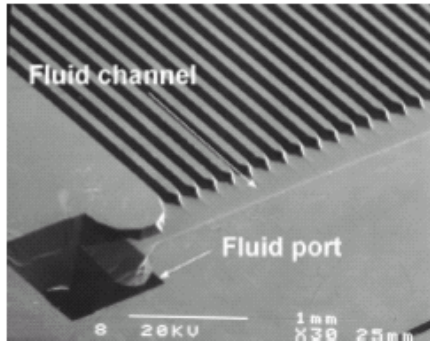


Figure 108: SEM micrograph showing the fluid port and micro channel of the micromachined microbial fuel cell

protonconducting capability. As shown in Figure 109, the PEM is then glued to the silicon substrates at the edges and syringe needles are used to establish the fluid interconnects. The electrical connection to the outside world is made by attaching aluminum foil to the Cr/Au surface. The final assembly is shown in Figure 110.

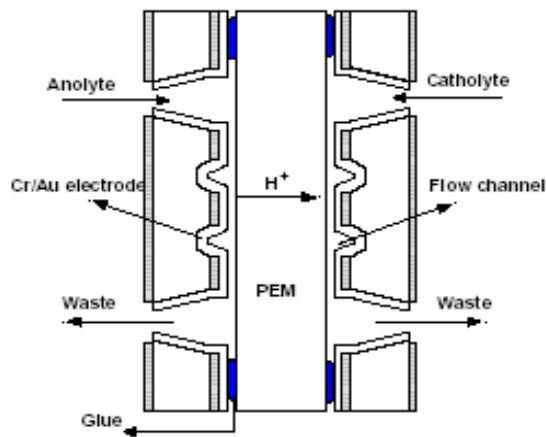


Figure 109: Cross-sectional view of micromachined microbial fuel cell

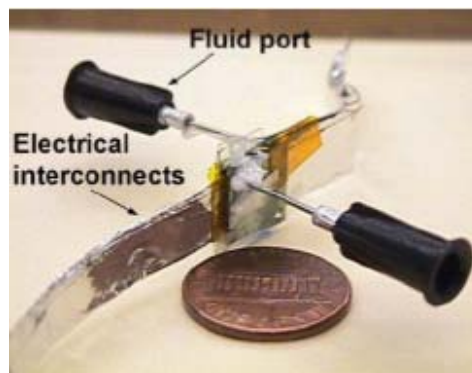


Figure 110: An assembled micromachined microbial fuel cell

The culturing of *Saccharomyces cerevisiae* follows the biology laboratory protocol. The nutrient suitable for yeast to grow is prepared by mixing agar powders with glucose, yeast extracts and dissolved in distilled water. The agar nutrient is then put into autoclave chamber for 1 hour. The high temperature (120°C) environment in the autoclave chamber is sufficient to kill unwanted bacteria species pre-exist in the nutrient mixture and prevent them from killing the yeast in the later culturing stage. After autoclaving, the nutrient becomes a liquid form and it must be poured into petri dishes before it is solidified around 42°C. The nutrient petri dishes can be stored in the refrigerator before use. The mother strain *Saccharomyces cerevisiae* is purchased from biological supply company and is kept in the refrigerator before use. Once the nutrient petri dish is prepared the strain of *Saccharomyces cerevisiae* is physically rubbed off from the mother plate by a sterile platinum loop and streak on to the nutrient petri dish. The petri dish is then covered and incubated under room temperature for 48 hours. The anolyte and catholyte are prepared subsequently. For anolyte, microorganism culture is mixed with 1 M of glucose in a 0.1 M phosphate buffer (pH 7.0). The electron transfer mediator, methylene blue of 0.01 M is then added in to promote the biochemical-to-electrical reaction efficiency. Moreover, a sufficient aeration is provided to enhance the fermentation process. On the cathode side, a 0.02 M potassium ferricyanide solution is prepared in a 0.1 M phosphate buffer (pH 7.0). The bio-electrical responses are measured by dropping a drop (volume 0.16 c.c.) of solution into the anode and cathode compartments, and the electrical signals are measured chronically.

Figure 111 shows the measurement results of the open-circuit voltage response of a microbial fuel cell. Both anolytes with and without yeast culture are presented in order to evaluate the effect of yeast metabolism. For anolyte with yeast, the average voltage is 343 mV over a 43-minute period. However, for anolyte without yeast, the voltage stays at 25 mV. Moreover, the effect of methylene blue is also addressed. Anolyte without methylene blue is put into the anode compartments and the open-circuit potential is found increasing from 25 mV to 40 mV in about 10 minutes and stay at 40 mV for another 30 minutes. When fresh anolyte is added into the fuel cell, a 10 to 15 minutes time delay is always observed before the open-circuit potential reaches its peak value. The ramping rate of the open-circuit potential could be dominated by the yeast metabolism and could have been improved if more active bacteria were used. Moreover, it was observed that the open-circuit potential drops gradually after 30 minutes as shown in Figure 111. This

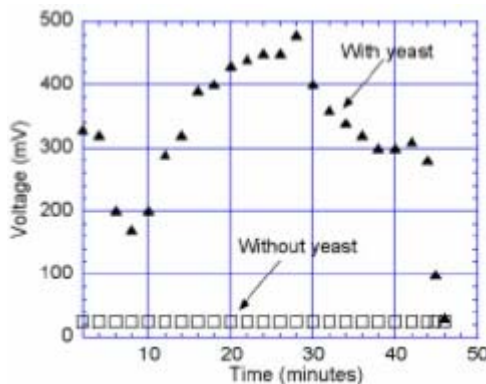


Figure 111: Open circuit measurements

is because of the glucose has been consumed and no more electrons and protons can be generated. The fuel cell discharge experiment is also carried out and the result is shown in Figure 112. Both 50-ohm and 10-ohm loading conditions are tested. Under a 50-ohm load, the current initially jumped to $1.3 \mu\text{A}/\text{cm}^2$ after the first drops of anolyte and catholyte were dispensed into the fuel cell. The current density dropped to $0.58 \mu\text{A}/\text{cm}^2$ after 5 minutes. However, it is consistently observed that the current density comes back up to $1.2 \mu\text{A}/\text{cm}^2$ after fresh drops of anolyte and catholyte are fed to the fuel cell. Under a 10-ohm load, the current density initially goes up to $15 \mu\text{A}/\text{cm}^2$ and drops to $3.6 \mu\text{A}/\text{cm}^2$ after 14 minutes. The power density (I^2R/volume) is characterized as $0.5 \mu\text{W}/\text{cm}^3$ under a 10 ohm-load and was found to have 5 orders of magnitude larger than previously reported value using macro scale machining process. This is due to the high surface-to-volume ratio in the reaction compartments and electrodes made by micromachining technologies. Moreover, the coulombic-yield can be estimated using the electric current-time product divided by theoretical total electrons generated from glucose oxidation and is found less than 1% in this experiment. This low efficiency energy conversion could result from 1) low metabolism of yeast (compare to more active bacteria, such as *E. Coli*); 2) oxygen in the anode compartment could strip electrons from methylene blue and reduce the total electrons transported to the anode; 3) the aluminum foil and Cr/Au interface could have a high contact resistance if the gluing process is not carried out well and 4) the proton conductivity of the PEM is a function of temperature and the optimized operating temperature for Nafion-117 is about $80\text{-}90^\circ\text{C}$. However, in the microbial fuel cell, the yeast could not expose to high temperature for a long period of time.

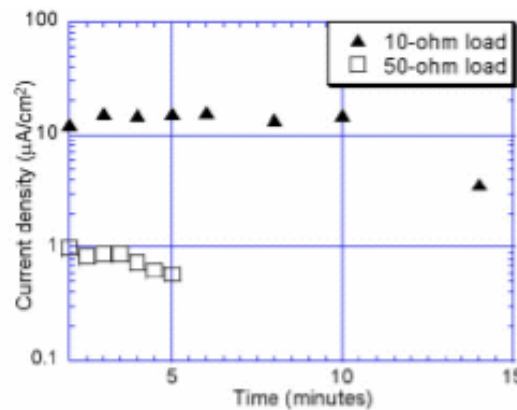


Figure 112: Discharge

5. CONCLUSIONS

This project has achieved many major accomplishments toward achieving a “Water-Powered Bioassay System.” These achievements can be summarized in three areas: (1) water-powered devices and fabrication processes; (2) bioassay; and (3) water-based power sources. This final report concisely covered many aspects of these accomplishments, and the very detailed results and procedures can be found in well-documented conference publications and journal publications listed at the end of this final report. In summary, we were able to develop several new osmotic, water-powered devices, including water-powered osmotic microactuators, water-powered osmotic micropumps, water-powered micro drug delivery system, water-powered droplet generators and water-powered micro accumulators. Every new water-powered device represents technology innovation and advancement. In developing these new water-powered devices, new material fabrication systems were also investigated and established. These include micro hot embossing of various polymer materials, molding of PDMS, localized plastics-to-silicon, glass and plastics bonding processes and the frozen water process. These new micromachining processes and systems make possible water-powered device fabrication and operation demonstrations. In the area of bioassay development, we are able to develop the wafer-level in-device enzyme immobilization scheme for the batch processing of micro glucose sensors; to develop a micro-gap glucose sensing architecture with and without using the assistance of MWCN (multi-wall carbon nanotubes) and to demonstrate an integrated bioassay sensing system with micro dialysis needles. These bioassay systems have gone through various types of characterization, including humidity, PH and glucose measurements. In the water-based power sources area, three types of micro power sources have been successfully demonstrated, including electrolyte-based operation by adding electrolyte into the microbattery chamber to generate electricity; water-activated long shelf-life microbattery by adding water to generate electrical power; and micromachined microbial fuel cells by adding glucose as the fuel and harness electrical power from the metabolism process in living cells. At the end of this project, we are confident that these new and innovative technologies and demonstrations will make a great impact on BioFlips research and commercial applications as well as military applications in the years to come.

6. RECOMMENDATIONS

We feel obligated to provide recommendations and future directions because there are many BioFlips research areas, including those in this project that require further developments. Among the water-powered devices we have demonstrated in this program, water-powered osmotic drug delivery system will be best applicable for implantable drug delivery applications because of its constant delivery rate and no electrical power is required. Although a micro drug delivery system was demonstrated, it goes beyond the scope of this current project in the area of in-vivo studies and biocompatibility qualifications. However, the foundations of the future research were clearly provided by the success of the current project. Similar recommendations apply to the methods of frozen water processes, plastic molding processes, and localized plastics bonding processes for biomedical applications. These processes require very dedicate control parameters and mechanisms to minimize the possible damages to the BioFlips materials, devices and systems and may require more development effort to optimize the processes beyond the scope of the current project. Furthermore, it is recommend that all of the fabrication processes should be applied at the wafer-level to reduce the manufacturing cost.

In the bioassay area, we feel that many investigations should be continued. These include long-term monitoring of the bioassay performance, reliability tests for the sensor operation at the system-level, bioassays of other than glucose as well as batch processing and low-cost manufacturing. In this project, we opened up several research fronts in the area of new device architecture and integrated system with microneedles. For example, micro-gap glucose sensors were first demonstrated as a two-terminal glucose sensor by the electrosynthesis of conducting polymer. The in-device enzyme immobilization scheme at the wafer-level was first suggested and successfully conducted. The integrated microneedle and glucose sensing system was first successfully manufactured and experimented. Unfortunately, in the University environment, we can only fabricate and test limited number of devices and the very comprehensive analyses of these biomedical-testing results should be conducted to gather statistical data before real commercialization. One possible future direction in this area is to collaborate with industrial companies/medical schools and conduct comprehensive tests on patients to gather data for possible FDA approval of these devices for practical applications. Another area to be addressed further is the microneedle tests. Would interstitial liquid be extracted painlessly from the body tissue to the external environment via the microneedle? How about the strength, penetration depth, flow rate of the microneedle operations? If these technical and research issues can be addressed in the near future, it will help the future development of the painless, microneedle-based bioassay systems and commercial products tremendously.

MEMS devices will need electricity to operate, but external batteries will sometimes be too costly, weight too much, and/or be too large for many microsystem applications. Several new water-based power sources have been developed and characterized in this project, including electrolyte-based on-demand microbatteries, water-activated microbatteries and cell-based microbial fuel cells. However, it will be difficult to implement some of these devices and processes into a real BioFlips setup

without further research. For example, both the electrolyte-based microbattery and microbial fuel cells will require toxic chemicals in these prototypes, that have to be replaced with mild chemicals or biocompatible materials. On the other hand, other advanced approaches should be pursued further to explore different energy generation paths at the microscale, such as photosynthetic electrochemical cells and other power generation mechanisms.

7. REFERENCES

- [1] F. Theeuwes, "Elementary Osmotic Pump", *Journal of Pharmaceutical Sciences*, 1975, pp. 1987-1991.
- [2] F. Theeuwes and S.I. Yum, "Principles of the Design and Operation of Generic Osmotic Pumps for the Delivery of Semisolid or Liquid Drug Formulations", *Annals of Biomedical Engineering*, 1976, pp. 343-353.
- [3] Alzet osmotic pumps, www.alzet.com.
- [4] Edith Mathiowitz, *Encyclopedia of Controlled Drug Delivery*, John Wiley & Sons, 1999.
- [5] S. Timoshenko and S. Woinowsky-Krieger, *Theory of Plates and Shells*, McGraw-Hill, 1959.
- [6] Liwei Lin, Y.T. Cheng, and C.J. Chiu, "Comparative Study of Hot Embossed Micro Structures Fabricated by Laboratory and Commercial Environments", *Microsystem Technologies*, pp. 113-116, 1998.
- [7] Liwei Lin, T.K. Shia, and C.J. Chiu, "Silicon-processed plastic micropyramids for brightness enhancement applications" *J. of Micromechanics and Microengineering*, 2000, pp. 395-400.
- [8] B.G. Casey, W. Monaghan, and C.D.W. Wilkinson, "Embossing of Nanoscale Features and Environments", *Microelectronic Engineering*, 1997, pp. 393-396.
- [9] C. Den Besten, R.E.G. van Hal, J. Munoz, and P. Bergveld, "Polymer Bonding of Micro-Machined Silicon Structures", *MEMS '92*, pp. 104-109.
- [10] B. Ilic, P. Neuzil, T. Stanczyk, D. Czaplewski, and G.J. Maclay, "Low Temperature Nafion Bonding of Silicon Wafers", *Electrochemical and Solid-State Letters*, 1999, pp. 86-87.
- [11] A. Han, K.W. Oh, S. Bhansali, H.T. Henderson, and C. H. Ahn, "A Low Temperature Biochemically Compatible Bonding Technique Using Fluoropolymers for Biochemical Microfluidic Systems", *MEMS '00*, pp. 414-418.
- [12] T. Desai, *Microfabricated Biocapsules for the Immuno-isolation of Pancreatic Islets of Langerhans*, Ph.D. dissertation, University of California, 1998.
- [13] R.G. Craig, *Restorative Dental materials*, Mosby-Year, 1993.

- [14] Liwei Lin, Selective Encapsulations of MEMS: Micro Channels, Needles, Resonators, and Electromechanical filters, Ph.D. Dissertation, University of California 1993.
- [15] Y.T. Cheng, Liwei Lin, and Khalil Najafi, "Localized Silicon Fusion and Eutectic Bonding for MEMS Fabrication and Packaging", J. of MEMS, 2000, pp.3-8.
- [16] ANSYS v.5.5, SAS IP, Inc, Southpointe, 275 Technology Drive, Canonsburg, PA 15317.

APPENDIX I. LIST OF JOURNAL PUBLICATIONS

- [1] Ki-Bang Lee, F. Sammoura and Liwei Lin, "Water Activated Disposable and Long Shelf Life Microbatteries," *Sensors and Actuators*, accepted.
- [2] Yu-Chuan Su and Liwei Lin, "A Water-Powered Micro Drug Delivery System," *IEEE/ASME Journal of Microelectromechanical Systems*, accepted.
- [3] Ki-Bang Lee and Liwei Lin, "Surface Micromachined Glass and Polysilicon Microchannels Using MUMPs," *Sensors and Actuators*, accepted.
- [4] Yu-Chuan Su, Jatan Shah and Liwei Lin, "Implementation and Analysis of Polymeric Microstructure Replication by Micro Injection Molding," *Journal of Micromechanics and Microengineering*, Vol. 14, No. 3, pp. 415-422, 2004.
- [5] Ki-Bang Lee and Liwei Lin, "Electrolyte-based On-demand and Disposable Microbattery," *IEEE/ASME Journal of Microelectromechanical Systems*, Vol. 12, pp. 840-847, 2003.
- [6] Yu-Chuan Su, Liwei Lin and A.P. Pisano, "A Water-Powered Osmotic Micro Acuator," *IEEE/ASME Journal of Microelectromechanical Systems*, Vol. 11, pp. 736-742, 2002.
- [7] Jr-Hung Tsai and Liwei Lin, "Active Microfluidic Mixer and Gas Bubble Filter Driven by Thermal Bubble Micropump," *Sensors and Actuators*, Vol. A 97-98, pp. 665-671, 2002.
- [8] Jr-Hung Tsai and Liwei Lin, "Transient Thermal Bubble Formation on Polysilicon Micro-Resisters," *ASME Journal of Heat Transfer*, Vol. 124, No. 2, pp. 375-382, 2002.
- [9] Jr-Hung Tsai and Liwei Lin, "Micro-to-Macro Fluidic Interconnectors with an Integrated Polymer Sealant," *Journal of Micromechanics and Microengineering*, Vol.11, No. 5, pp. 577-581, 2001.

APPENDIX II. LIST OF CONFERENCE PRESENTATIONS

- [1] K.S. Teh and Liwei Lin, "A Polypyrrole-Carbon-Nanotube (PPY-MWNT) Nanocomposite Glucose Sensor," *Proceedings of 17th IEEE Micro Electro Mechanical Systems Conference*, pp. 395-398, Maastricht, Netherlands, Jan. 2004.
- [2] S. Li, W. Liu and Liwei Lin, "On-Chip Cryopreservation of Cells," *Proceedings of 17th IEEE Micro Electro Mechanical Systems Conference*, pp. 287-390, Maastricht, Netherlands, Jan. 2004.
- [3] K.B. Lam, E. Johnson and Liwei Lin, "A Bio-Solar Cell Powered by Sub-Cellular Plant Photosystems," *Proceedings of 17th IEEE Micro Electro Mechanical Systems Conference*, pp. 220-223, Maastricht, Netherlands, Jan. 2004.
- [4] K. S. Teh and L. Lin, "A Micro-Gap Sensor Based on Conducting Polypyrrole", *The 7th International Conference on Micro Total Analysis Systems, Technical Digest*, pp. 1195-1198, Squaw Valley, USA, October 5-9, 2003.
- [5] Y.C. Su and L. Lin, "Geometry and Surface Assisted Flow Discretization," *12th Int. Conference on Solid State Sensors and Actuators, Transducers'03*, Technical Digest, pp. 1812-1815, Boston, June 2003.
- [6] K.S. Teh, Y.T. Cheng and L. Lin, "Nickel Nano-Composite Film For MEMS Applications," *12th Int. Conference on Solid State Sensors and Actuators, Transducers'03*, Technical Digest, pp. 1534-1537, Boston, June 2003.
- [7] S. Zimmermann, D. Fienbork, B. Stoeber, A.W. Flounders and D. Liepmann, "A Microneedle-based Glucose Monitor: Fabrication on a Wafer-Level Using In-Device Enzyme Immobilization," *12th Int. Conference on Solid State Sensors and Actuators, Transducers'03*, Technical Digest, pp. 99-102, Boston, June 2003.
- [8] J. Frank and A.P. Pisano, "Low-Leakage Micro Gate Valves," *12th Int. Conference on Solid State Sensors and Actuators, Transducers'03*, Technical Digest, pp. 143-146, Boston, June 2003.
- [9] E.D. Hobbs and A.P. Pisano, "Micro Capillary-Force Driven Fluidic Accumulator/Pressure Source," *12th Int. Conference on Solid State Sensors and Actuators, Transducers'03*, Technical Digest, pp. 155-158, Boston, June 2003.
- [10] M. Chiao, K.B. Lam and Liwei Lin, "Micromachined Microbial Fuel Cells," *Proceedings of IEEE Micro Electro Mechanical Systems Conference*, pp. 383-386, Kyoto, Japan, Jan. 2003.

- [11] K.B. Lee, F. Sammoura and Liwei Lin, "Water Activated Disposable and Long Shelf Life Microbatteries," *Proceedings of IEEE Micro Electro Mechanical Systems Conference*, pp. 387-390, Kyoto, Japan, Jan. 2003.
- [12] K.B. Lam, M. Chiao, and Liwei Lin, "A Micro Photosynthetic Electrochemical Cell," *Proceedings of IEEE Micro Electro Mechanical Systems Conference*, pp. 391-394, Kyoto, Japan, Jan. 2003.
- [13] K.B. Lee and Liwei Lin, "Surface Micromachined Glass and Polysilicon Microchannels Using MUMPs," *Proceedings of IEEE Micro Electro Mechanical Systems Conference*, pp. 578-581, Kyoto, Japan, Jan. 2003.
- [14] S. Li, L.W. Pan and Liwei Lin, "Frozen Water for MEMS Fabrication and Packaging Applications," *Proceedings of IEEE Micro Electro Mechanical Systems Conference*, pp. 650-653, Kyoto, Japan, Jan. 2003.
- [15] Mu Chiao, Kien B. Lam, Yu-Chuan Su and Liwei Lin, "A Miniaturized Microbial Fuel Cell," *Technical Digest of Solid-State Sensors and Actuators Workshop*, pp. 59-60, Hilton Head Island, June 2002.
- [16] Y.C. Su, Liwei Lin and A.P. Pisano, "A Water-Powered Micro Drug Delivery System," *Technical Digest of Solid-State Sensors and Actuators Workshop*, pp. 69-72, Hilton Head Island, June 2002.
- [17] L.W. Pan, Y.C. Su, S. Li and Liwei Lin, "A Disposable Capillary Micropump Using Frozen Water as Sacrificial Layer," *Technical Digest of Solid-State Sensors and Actuators Workshop*, pp. 293-296, Hilton Head Island, June 2002.
- [18] K.B. Lee and Liwei Lin, "Electrolyte Based On-Demand and Disposable Microbattery," *Proceedings of IEEE Micro Electro Mechanical Systems Conference*, pp. 236-239, Las Vegas, Jan. 2002.
- [19] Y.C. Su, Liwei Lin and A.P. Pisano, "Water-Powered, Osmotic Microactuator," *Proceedings of IEEE Micro Electro Mechanical Systems Conference*, pp. 393-396, Jan. 2001, Interlaken, Switzerland.
- [20] Y.C. Su and Liwei Lin, "Localized Plastic Bonding for Micro Assembly, Packaging and Liquid Encapsulation," *Proceedings of IEEE Micro Electro Mechanical Systems Conference*, pp. 50-53, Jan. 2001, Interlaken, Switzerland.
- [21] K.B. Lee and Liwei Lin, "Electrolyte Based On-Demand and Disposable Microbattery," *Proceedings of IEEE Micro Electro Mechanical Systems Conference*, pp. 236-239, Las Vegas, Jan. 2002.